



PhD thesis

Methods in Statistical Data Analysis of the Cosmic Microwave Background Polarization After Planck

James Creswell

Advisor: Pavel Naselsky

Submitted: 23 July 2021

This thesis has been submitted to the PhD School of The Faculty of Science, University of Copenhagen

ABSTRACT

The B mode of the polarization of the cosmic microwave background, which is a unique estimator of the presence of cosmological gravitational waves in the early universe, is the target of upcoming high sensitivity CMB experiments. In this thesis, new methods are developed for statistical analysis of the CMB polarization. The E and B modes are defined in the space of the Stokes parameters, and the mathematical properties of the E–B decomposition are investigated. These E and B families are applied to the analysis of the morphology and frequency dependence of the thermal dust polarized foregrounds, revealing spectral differences between the E and B modes. This is followed by the presentation of a new method for correction of E–B leakage and the estimation of the B mode map using partial sky data. The method can improve the accuracy of the B mode power spectrum estimation by multiple orders of magnitude. The statistics of the polarization angle and the non-polarized points are investigated. Among other results, the E and B modes are found to have distinct signatures in the polarization angle distribution function, and the number density of non-polarized points is shown to correlate with the tensor-to-scalar ratio r under conditions of gravitational lensing. These statistical methods are applied to the polarization data from the latest *Planck* release. Lastly, the large-scale anomalies of the CMB are examined using new map-space methods, which reveal connections in the parity asymmetry and the alignments of the low multipoles.

RESUMÉ

Det B-mode i den kosmisk mikrobølgebaggrundsstråling, som er en unik indikator for tilstedeværelsen af kosmologiske gravitationsbølger i det tidlige univers, er målet for kommende års CMB-eksperimenter. I denne afhandling udvikles nye metoder til statistisk analyse af CMB-polarisationen. De E- og B-modes er defineret ud fra Stokes parametrene, og de matematiske egenskaber ved E–B dekompositionen undersøges. Disse E- og B-familier anvendes til analyse af morfologien og frekvensafhængigheden af kosmisk støv, som afslører spektrale forskelle mellem E og B. Derefter følger præsentationen af en ny metode til korrektion af E–B leakage og estimering af B-mode-mønstre. Metoden kan forbedre nøjagtigheden af B-mode powerspektrum med flere størrelsesordener. Statistikken for polarisationsvinklen og de ikke-polariserede punkter er undersøgt. Blandt andre resultater kan nævnes, at E- og B-modes har forskellige signaturer i histogrammet af polarisationsvinklerne, og at antallet af ikke-polariserede punkter er korreleret med tensor-til-skalar-forhold r . Der er anvendt data fra den seneste udgivelse af *Planck*. Stor-skala anomalierne undersøges ved hjælp af nye metoder, der forbinder paritets asymmetri og de parallelle axer for lave multipoler.

CONTENTS

ABSTRACT	iii
PREFACE	ix
1 THE COSMIC MICROWAVE BACKGROUND	1
1.1 Observation of the CMB	3
1.2 Anisotropy of the CMB	4
1.3 Polarization of the CMB	6
1.4 Galactic and extra-Galactic foregrounds	14
1.5 Data representation	17
2 E AND B MODES OF THE STOKES PARAMETERS	21
2.1 E-B decomposition of the Stokes vector	22
2.2 Real-space convolution kernels	25
2.3 Polarization analysis of foregrounds	34
3 E-B LEAKAGE	47
3.1 Diffusive inpainting	48
3.2 Real space leakage model	50
3.3 Recycling method	55
3.4 Tests	57
4 STATISTICS OF POLARIZATION ANGLES	69
4.1 Polarization angle distribution functions	70
4.2 Statistics of Gaussianity parameters	77
5 NON-POLARIZED POINTS AND THEIR STATISTICS	83
5.1 Gaussian theory	84
5.2 Lensing and the E/B modes	91
5.3 Non-polarized point analysis in the 2018 Planck maps	93
	vii

6	LARGE SCALE ANOMALIES IN TEMPERATURE AND POLARIZATION . .	103
6.1	Point parity asymmetry	105
6.2	Quadrupole–octupole alignment	112
6.3	Polarization	115
	CONCLUSION AND OUTLOOK	119
	REFERENCES	121
	ACKNOWLEDGMENTS	137

PREFACE

In modern cosmology, it is thought that quantum fluctuations at the earliest times evolved into the large-scale structure of matter in the universe [1, 2]. The cosmic microwave background, a relic radiation source from the early universe, provides the strongest observational evidence verifying this theory.

In the past decade, the *Planck* satellite experiment has mapped the anisotropies of the CMB at high precision, and the results attest to a model of the universe with expanding, spatially flat, statistically homogeneous cosmology, having fluctuations that were initially adiabatic and Gaussian, and composed at late times primarily of dark energy and cold dark matter [3]. The parameters of this model, termed the Λ CDM model for its two main late-time constituents, are well-constrained by the *Planck* observations [4]. The *Planck* results also constrain the tensor-to-scalar ratio r , an important constant measuring the strength of gravitational waves in the early universe which are related to the inflationary potential, at around $r \lesssim 0.1$ [4–6].

The upcoming decade will see new efforts to study the polarization of the CMB, aiming to improve constraints on cosmological parameters and the physics of inflation. The next generation of CMB experiments include LiteBIRD [7–9], CMB-S4 [10], the Simons Observatory [11], and AliCPT [12]. These experiments are aiming for a sensitivity to the tensor-to-scalar ratio at a level of $r \approx 10^{-3}$.

In order to accomplish this, the main target is the detection of the B mode of the CMB polarization. The total polarization signal can be split into a curl-free E mode and a divergence-free B mode. It was observed that normal Thomson scattering during the recombination era produces no B mode; instead, a B mode signal is expected from tensor fluctuations that are predicted by inflationary theory [13–15]. The amplitude of the B mode is linked to the tensor-to-scalar ratio r . The B mode map measured by *Planck* is dominated by noise and foreground residuals, and the primordial B mode in the current data is consistent with zero.

Methods to characterize the primordial B mode and uncover it from the foreground signals, noise, and systematic errors that obscure it is a major current research question and is the theme of this thesis. One particular complication occurs when part of the sky is masked or unobserved, resulting in leakage effects that contaminate the observed B mode with power from the much stronger E mode. Upcoming CMB experiments that are

ground-based have limited sky coverage. Even full-sky surveys are not free from partial-sky coverage due to Galactic foreground masks, and therefore the leakage problem is inevitable. Because of these limitations, using the B mode to improve constraints on r calls for an improved understanding of the foreground polarization signals and the correction of leakage, together with the design of estimators which fully exploit the available polarization data.

In preparation for upcoming high-sensitivity observations, this thesis presents new work in several directions for data analysis of the CMB polarization. These include the E–B decomposition, analysis of the polarized foregrounds, correction of the E–B leakage, and the study of statistical estimators based on polarization angles and non-polarized points. The first chapter introduces the physical properties of the CMB, the history of its observation, and its mathematical and discrete descriptions, focusing especially on the CMB polarization and the standard formulations of the E and B modes.

In chapter 2, the E–B decomposition is reformulated in the map domain as an integral convolution of the input polarization data with corresponding E and B kernels. The E and B kernels reveal the underlying geometric structure and non-locality of the E–B decomposition. The map-domain E–B decomposition also retains the full capacity of the Stokes parameters, enabling the definition of polarization intensities and polarization angles corresponding to the E and B modes separately. These estimators are applied to the analysis of the polarized foregrounds in chapter 2; foreground analysis, especially, benefits from the map domain estimators, revealing variation of foreground properties across the sky and their influence on the E and B modes.

The map domain E–B decomposition opens new doors for the correction of E–B leakage. In chapter 3, a new method of correcting leakage in the map domain is presented, and its performance is validated using simulations of partial-sky CMB observations. The method produces a cleaned B mode map with leakage greatly reduced, and in combination with the MASTER method for estimation of the power spectrum, it can reduce the error on the power spectrum such that it is at an insignificant level compared to other residuals, in the interesting multipole range of ℓ from about 60 to 120.

In chapter 4, further statistical properties of the CMB polarization are explored, focusing on the statistics of the polarization angle ψ . The polarization angle has an important role in the analysis of foregrounds, where it reflects physical processes in the Galaxy and the interstellar medium. It is also sensitive to systematic errors. The distribution of the polarization angle for general Gaussian polarization data is considered, and it is found that the E and B modes produce polarization angle distributions with unique signatures.

In chapter 5, the zero points of the polarization field are investigated. The classification of these points and their corresponding number densities on the sky are sensitive to the statistical properties of the polarization, which is used as the basis to construct a test of Gaussianity applied to the *Planck* component separation maps. It is also shown that the total number density of non-polarized points is linked to gravitational lensing.

In chapter 6, attention is turned to the large-scale anomalies of the cosmic microwave

background, including the parity asymmetry and the quadrupole–octupole alignment. The anomalies are reexamined using new map-domain methods. The parity asymmetry is shown to be related to specific zones on the sky, which are also related to the direction of the kinematic dipole and the alignments of the low multipoles. While this analysis occurs on the temperature data, the methods and estimators can be transferred to the polarization, where some hints of parity asymmetry appear in the U Stokes parameter.

* * *

During my graduate studies, I have contributed to thirteen papers on which I have been included as a co-author. Eight papers are related to CMB data analysis and the results in this thesis [16–23]. Some results and figures in this thesis are reused from these papers.

Lastly, I wish to express my gratitude to my supervisor, Professor Pavel Naselsky, and my colleagues at the Niels Bohr Institute, especially Professor Andrew D. Jackson, Professor Hao Liu, Dr. Sebastian von Hausegger, Nadia Dachlythra, Aske Ravnebjerg, Jaan Kasak, and Jacob Hjortlund. I am also obliged to Dr. Amel Durakovic for reading the text and making helpful suggestions.

JAMES CRESWELL

Copenhagen, Denmark
July 2021

1 THE COSMIC MICROWAVE BACKGROUND

A homogeneous and isotropic universe is described by the Robertson–Walker spacetime metric:

$$ds^2 = g_{\mu\nu} dx^\mu dx^\nu = -c^2 dt^2 + a(t)^2 dx^2, \quad (1.1)$$

where $a(t)$ is the scale factor that parametrizes the relative expansion of physical distances and dx^2 is the metric of a three-dimensional space with a uniform curvature. The evolution of $a(t)$ is given by general relativity and depends on the matter and energy composition of the universe.

A period of exponential expansion of the scale factor in the very early universe explains several aspects of observational cosmology which are otherwise problematic. These include the flatness of the universe, which is measured today to be nearly exactly flat [4]. In the standard expanding universe, flatness is an unstable equilibrium, and any departure from flatness should grow as the universe expands. The small measured curvature therefore seems to indicate fine tuning in the normal model. During exponential expansion of the scale factor, however, the curvature would be suppressed towards zero, removing the need for fine tuning.

Another difficulty of the non-inflationary universe is the horizon problem. As discussed below, the CMB is nearly perfect blackbody emission with a temperature that is almost constant over the full sky, implying that there was some time at which the entire observable universe was in thermal equilibrium. However, according to the normal expansion history, different parts of the sky that are separated by more than a few degrees should be causally disconnected. Inflation provides a mechanism to make the CMB isotropic, again avoiding fine tuning.

There are many inflationary models, which were originally proposed to solve these problems [24, 25]. Generally, the existence of a scalar field ϕ is proposed, corresponding to an inflation particle that drives exponential expansion of the universe. The inflaton is subject to a potential $V(\phi)$ and is originally displaced from its minimum. Under “slow-roll” conditions, when

$$\left(\frac{d\phi}{dt}\right)^2 \ll V(\phi), \quad (1.2)$$

inflation ensues with almost exponential growth of the scale factor.

Inflation expands small quantum fluctuations in the inflaton field into the primordial density perturbations, which are predicted to be Gaussian, adiabatic, and nearly scale invariant [1, 2]. These predictions are confirmed by observations of the CMB. For the curvature perturbations in comoving gauge, denoted \mathcal{R} , a power spectrum is expected that is approximately described by a power law:

$$\Delta_{\mathcal{R}}^2(k) = \frac{k^3 \langle |\mathcal{R}_k|^2 \rangle}{2\pi^2} \propto k^{n_s-1}. \quad (1.3)$$

When the spectral index $n_s = 1$, the perturbations are exactly scale invariant. The current *Planck* measurement of the spectral index is $n_s = 0.965 \pm 0.004$ [4]. The primordial power spectrum affects the angular power spectrum of the CMB, and therefore the statistical properties of the CMB map.

Apart from the scalar curvature perturbations, the theory of inflation also predicts the existence of tensor metric perturbations [26]. Tensor perturbations result from gravitational waves, which can be represented in terms of the $+$ and \times polarizations, denoted h_+ and h_\times . The power spectrum of the tensor perturbations, summing over both polarizations, is

$$\Delta_h^2(k) = 2 \frac{k^3 \langle |h_{+,k}|^2 + |h_{\times,k}|^2 \rangle}{2\pi^2}, \quad (1.4)$$

which is also usually described in terms of a power law model $\Delta_h^2(k) \propto k^{n_t}$. More generally, scale-dependent running of the spectral indices n_s and n_t is allowed.

The amplitude of the gravitational waves is given in terms of the tensor-to-scalar ratio r , defined as the ratio of the power spectrum of tensor fluctuations to the power spectrum of scalar fluctuations, evaluated at a relevant scale $k = k_0$:

$$r = \frac{\Delta_h^2(k_0)}{\Delta_{\mathcal{R}}^2(k_0)}. \quad (1.5)$$

The tensor-to-scalar ratio r is directly linked with the energy scale of inflation, and it is the target of considerable experimental effort, ongoing and upcoming. The tensor fluctuations also affect the angular power spectrum of the CMB temperature, but the information is limited by cosmic variance. Greater sensitivity is available in the polarization of the CMB, and especially in the B mode. The current observational constraint on r by *Planck* is approximately $r < 0.1$; in combination with other current datasets, $r < 0.05$ is achievable with some confidence [6, 27, 28]. The goal for upcoming CMB observations in the next decade is $r \approx 10^{-3}$.

The remainder of this chapter introduces the important elements that underlie CMB data analysis, including the history and status of CMB observations and the mathematical description of CMB data. The focus is especially on establishing the mathematics of the CMB polarization and the standard E and B modes.

1.1 OBSERVATION OF THE CMB

Direct observation of the CMB began in 1964 with the unintentional discovery by Penzias & Wilson of a residual background noise term in a horn antenna designed for satellite radio communication [29], followed almost immediately by the deliberate measurement of the CMB by a team at Princeton University [30]. This observation was the starting point of a new era of observational cosmology, but it was also the culmination of theoretical predictions about the science of the CMB, especially the work of Gamow, Alpher, and Herman in the 1940s, who attempted to explain the chemical composition of the early universe in a hot Big Bang model [31–34]. The first recognition of the possibility of detecting the CMB, and the prediction of its blackbody spectrum, was made shortly before its actual discovery in 1964 [35].

Space-based study of the CMB began with the RELIKT-1 experiment launched in 1983 [36, 37]. The sky at 37 GHz was mapped with an angular resolution of about 5° , which was sufficient to identify the CMB dipole and microwave emission from the Galaxy and to place an upper bound on the quadrupole fluctuations. RELIKT-1 was followed by COBE, the Cosmic Background Explorer, which made multi-frequency observations of the CMB, verifying its blackbody spectrum, and made robust measurements of the CMB anisotropy, albeit at low resolution of around 7° [38–41].

COBE was followed by WMAP, the Wilkinson Microwave Anisotropy Probe [42–44]. Launched in 2001, WMAP began the era of precision CMB astronomy from space, mapping the full sky at a resolution of about 15 arcminutes. The data measured by WMAP began to place tight constraints on cosmological parameters [45, 46].

The current generation full-sky CMB mission is *Planck* [47]. The *Planck* satellite was launched in May 2009 into an orbit around the L2 Lagrange point. It began taking observations in July of the same year. The satellite spins at one revolution per minute, with its telescope beams tracing a large circle around the sky. As the L2 point orbits around the sun, the entire sky is gradually traced out by the spinning satellite.

Planck's telescope consists of two instruments, each bearing a large number of bolometers. The Low Frequency Instrument (LFI) observes in 3 bands centered at 30 GHz, 44 GHz, and 70 GHz; the High Frequency Instrument (HFI) observes in 6 bands centered at 100 GHz, 143 GHz, 217 GHz, 353 GHz, 545 GHz, and 857 GHz. The sensitivity and resolution achievable vary by instrument and frequency band, but in general improves significantly on WMAP, reaching resolutions down to 5 arcminutes. Apart from the 545 GHz and 857 GHz bands, the LFI and HFI are both equipped to measure the CMB temperature and polarization.

Following *Planck*, the next generation full-sky CMB mission is LiteBIRD, currently expected to be launched in 2028 [7–9]. Joining the space missions, ongoing and upcoming balloon-borne experiments also contribute to the current and next-generation CMB data landscape [48–50]. Balloons are generally flown from polar sites [51, 52]. Finally, there are many ground-based observatories in the operating and planning phases [7–12, 53–57].

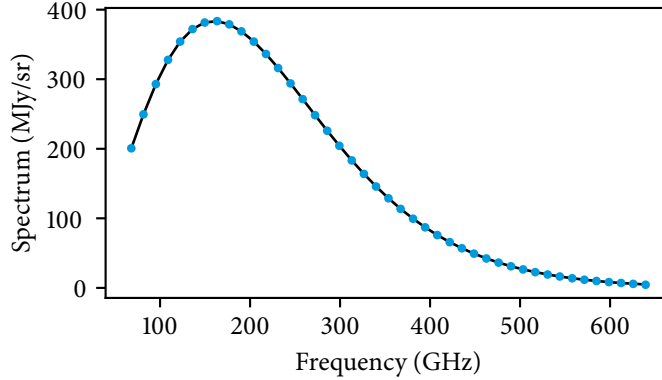


Figure 1.1: The CMB blackbody spectrum measured by the FIRAS instrument aboard the COBE satellite [58, 59]. The measurements are shown in blue dots, above the theoretical blackbody curve with $T = 2.725$ K.

1.2 ANISOTROPY OF THE CMB

The spectrum of the CMB at any point on the sky is observed to follow Planck's law for blackbody radiation, in which the intensity at frequency ν is

$$I_\nu = \frac{2h\nu^3}{c^2} \frac{1}{e^{h\nu/kT} - 1}. \quad (1.6)$$

Measurements of the CMB intensity are usually reported in terms of the effective temperature. Letting $T(\hat{n})$ denote the observed temperature at each direction \hat{n} on the sky, the mean temperature is observed to be

$$\frac{1}{4\pi} \int T(\hat{n}) d\hat{n} = 2.725 \pm 0.001 \text{ K}. \quad (1.7)$$

Measurements of the CMB spectrum by COBE are shown in figure 1.1. The spectrum agrees with a blackbody with a temperature of 2.725 K to high precision.

Blackbody emission is expected from a photon gas in thermal equilibrium. These observations are therefore consistent with the inflationary hot Big Bang model of the universe. However, the observed temperature is not perfectly constant on the sky for several reasons. The strongest anisotropy, of order 3 mK, is the dipole distortion, which can be caused by the redshift due to the motion of the telescope with respect to the rest frame of the CMB. The dipole is usually attributed entirely to such peculiar motion and subtracted from the CMB.

Temperature fluctuations

After subtraction of the dipole, the isotropy of the CMB temperature is still broken by small fluctuations. The relative temperature fluctuation is defined as

$$\Delta T(\hat{n}) = T(\hat{n}) - \frac{1}{4\pi} \int T(\hat{n}) d\hat{n}. \quad (1.8)$$

The size of the temperature fluctuations is dependent on the angular scale at which observations are made. The strongest fluctuations, seen on angular scales of around 1° , are at around the $80 \mu\text{K}$ level.

Several physical processes in the early universe give rise to the temperature fluctuations of the CMB. In general, the temperature fluctuations reflect the uneven distribution of matter at the time of the formation of the CMB, which is why the primordial density fluctuations can be measured in the anisotropy of the CMB.

Harmonic transformation

The temperature fluctuation is a scalar-valued function on the sphere, and it can be written as a linear combination of spherical harmonics:

$$\Delta T(\hat{n}) = \sum_{\ell=1}^{\infty} \sum_{m=-\ell}^{\ell} a_{\ell m} Y_{\ell m}(\hat{n}). \quad (1.9)$$

The harmonic coefficients $a_{\ell m}$ are generally complex numbers, although real input implies constraints between their values. The decomposition is orthogonal, and the $a_{\ell m}$ coefficients can be calculated from $\Delta T(\hat{n})$ by integration over the full sky with the corresponding spherical harmonic function:

$$a_{\ell m} = \int \Delta T(\hat{n}) Y_{\ell m}(\hat{n}) d\hat{n}. \quad (1.10)$$

The harmonic domain is commodious to the statistical description of the temperature anisotropy. According to standard theories of inflation, the anisotropy is a realization of a Gaussian random field, which can be described in the harmonic domain, and its statistical properties are mainly characterized by its power spectrum, C_ℓ . This means that its $a_{\ell m}$ coefficients are random variables with zero mean and covariance

$$\langle a_{\ell m} a_{\ell' m'}^* \rangle = \delta_{\ell\ell'} \delta_{mm'} C_\ell. \quad (1.11)$$

C_ℓ is the power spectrum, which is positive and real-valued, and measures the variance over m of the $a_{\ell m}$ at each ℓ . The covariance $\langle a_{\ell m} a_{\ell' m'}^* \rangle$ contains no dependence on m , reflecting the isotropy of the Gaussian random field. The $2\ell + 1$ instances of $a_{\ell m}$ at each

ℓ therefore constitute independent realizations, from which the power spectrum can be estimated by

$$\hat{C}_\ell = \frac{1}{2\ell + 1} \sum_{m=-\ell}^{\ell} |a_{\ell m}|^2. \quad (1.12)$$

This estimate is highly uncertain at low ℓ , where only a few values of m exist to be averaged.

Under rotations of the coordinate system, the $a_{\ell m}$ coefficients will change, but the power spectrum is rotationally invariant. In general, the spherical harmonics at a particular ℓ vary on an angular scale of approximately $100^\circ/\ell$. The value of C_ℓ , which is linked to the total power in the $a_{\ell m}$ coefficients that multiply the spherical harmonics in the harmonic expansion, is therefore a measure of the strength of temperature fluctuations on the angular scale corresponding to ℓ . This interpretation is particularly useful for summarizing the properties of the CMB. The power spectrum estimated from the *Planck* data is shown in the upper panel of figure 1.2.

The temperature fluctuations can also be considered in real space. The two-point correlation function is

$$C(n_1, n_2) = \langle \Delta T(\hat{n}_1) \Delta T(\hat{n}_2) \rangle. \quad (1.13)$$

Under conditions of statistical isotropy, the correlation function depends only on the angle between n_1 and n_2 . In terms of $\cos(\theta) = \hat{n}_1 \cdot \hat{n}_2$, it can be written in the form

$$C(\theta) = \frac{1}{4\pi} \sum_{\ell=0}^{\infty} (2\ell + 1) C_\ell P_\ell(\cos(\theta)), \quad (1.14)$$

where C_ℓ is the power spectrum and P_ℓ are the Legendre polynomials.

1.3 POLARIZATION OF THE CMB

The CMB is polarized, which is expected from anisotropic scattering at the surface of last scattering. The mathematical description of the polarization of the CMB is complicated by the dependence on the coordinate system in which the data is represented.

Stokes parameters

The polarization of electromagnetic waves can be described in several ways. It is conventional to use the Stokes parameters [61]. Given a Cartesian basis (x, y) in the plane orthogonal to the incoming wave, and another Cartesian basis (a, b) rotated by 45° from (x, y) , the Stokes parameters are defined in terms of the projections of the electric field

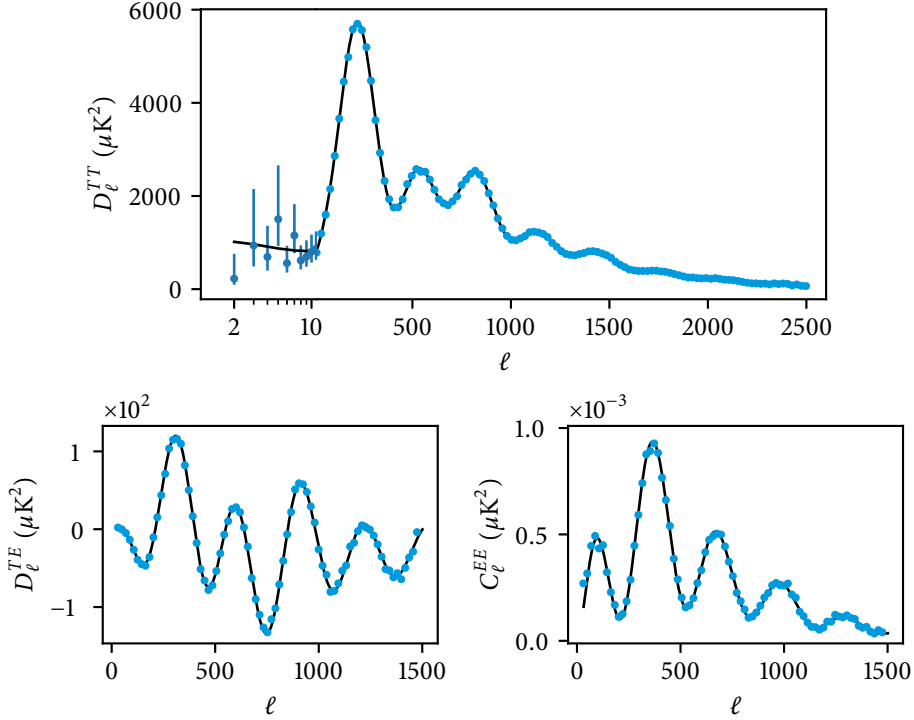


Figure 1.2: TT, TE, and EE angular power spectra measured by *Planck* [60]. The black curves show the Λ CDM model with best-fit parameters, and the blue dots show the measured values. The TT and TE spectra are plotted in terms of $D_\ell = \ell(\ell + 1)C_\ell/2\pi$.

vector $E = (E_x, E_y)$ [62]

$$I = \langle E_x^2 \rangle + \langle E_y^2 \rangle; \quad (1.15a)$$

$$Q = \langle E_x^2 \rangle - \langle E_y^2 \rangle; \quad (1.15b)$$

$$U = \langle E_a^2 \rangle - \langle E_b^2 \rangle. \quad (1.15c)$$

The $\langle \cdot \rangle$ brackets denote time averages. I is the amplitude, or total intensity of the wave; note that this quantity is coordinate-independent. Q and U measure the preference for orientation aligned with the (x, y) and (a, b) axes. If there is no preference, and the orientation of the wave varies randomly in time, then the expectation values in each direction will be equal to each other, and Q and U will be 0. A general description of polarization requires a fourth Stokes parameter, denoted V , which measures circular

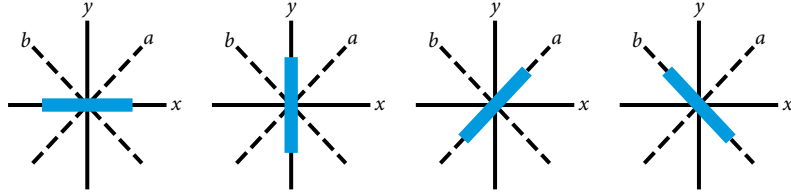


Figure 1.3: The blue bar shows the electric field orientation of an incoming electromagnetic wave with polarization described by, from left to right, pure $Q > 0$, pure $Q < 0$, pure $U > 0$, and pure $U < 0$. In general there will be some superposition with nonzero Q and U .

polarization; but, since V is not produced normally by Thomson scattering, it is normally neglected. Figure 1.3 shows examples of pure Q and pure U polarizations.

The values of Q and U depend on the coordinate system chosen. Under a rotation of the axes by an angle ψ , they transform together as

$$\begin{pmatrix} Q \\ U \end{pmatrix} \xrightarrow{\psi} \begin{pmatrix} Q' \\ U' \end{pmatrix} = \begin{pmatrix} \cos(2\psi) & \sin(2\psi) \\ -\sin(2\psi) & \cos(2\psi) \end{pmatrix} \begin{pmatrix} Q \\ U \end{pmatrix}. \quad (1.16)$$

The Stokes parameters are unchanged under a half rotation ($\psi = \pi$). The combination $Q \pm iU$ transforms as

$$(Q \pm iU) \xrightarrow{\psi} (Q' \pm iU') = e^{\mp 2i\psi} (Q \pm iU). \quad (1.17)$$

This is the transformation law for a spin-2 quantity, and therefore $Q \pm iU$ has a definite spin of ± 2 .

A normal spherical polar coordinate system induces local Cartesian coordinates in each direction.¹ When the Stokes parameters are defined with respect to the local Cartesian coordinates induced by overall spherical coordinates on which they are measured, which is usual, then a rotation of the overall coordinates mixes Q and U at every point according to equation (1.17). The Stokes parameter maps defined in this way comprise a spin-2 field on the sphere.

In terms of the Stokes parameters are defined the polarization intensity

$$P = \sqrt{Q^2 + U^2} \quad (1.18)$$

and the polarization angle

$$\psi = \frac{1}{2} \arctan\left(\frac{U}{Q}\right). \quad (1.19)$$

¹There are two conventions for the local coordinate system, depending on whether the z axis, which is parallel to the line of sight, is taken to point towards or away from the observer. CMB data analysis generally uses the convention which is not recommended by the IAU; see [63]. In the IAU convention, the axes in figure 1.3 would be swapped.

These quantities are an alternative description of the polarization state. The opposite transformation from P and ψ to Q and U is

$$Q = P \cos(2\psi); \quad (1.20a)$$

$$U = P \sin(2\psi). \quad (1.20b)$$

The factor of $1/2$ in equation (1.19), and likewise the factor of 2 in equation (1.20), reflect the geometric fact that the general elliptical polarization state is indistinguishable after rotations of 180° . Q and U are often combined into a *Stokes vector* or *polarization vector*

$$\vec{P} = \begin{pmatrix} Q \\ U \end{pmatrix}. \quad (1.21)$$

But this object is a spurious “vector” that does not transform like a real vector under coordinate transformations. Nevertheless in some cases it is a useful notation to represent the Stokes parameters.

The Stokes parameters are straightforward to measure experimentally. If Q and U are measured with symmetric Gaussian errors, then equation (1.18) is a noise-biased estimate of the polarization intensity, being strictly positive and always overestimated in the presence of noise. Alternative unbiased estimators of the polarization intensity are sought in [64]. The statistical theory of the polarization angle is the subject of chapter 4.

Standard E and B modes

As discussed above, when $Q(\hat{n})$ and $U(\hat{n})$ are defined on the sphere, their values are linked to a specific spherical coordinate system. It is possible to seek a rotationally invariant description of polarization measured on the sphere. $Q(\hat{n}) \pm iU(\hat{n})$ is a spin-2 field which can be expanded in terms of spin-weighted spherical harmonics as [65]

$$Q(\hat{n}) \pm iU(\hat{n}) = \sum_{\ell=2}^{\infty} \sum_{m=-\ell}^{\ell} a_{\pm 2, \ell m \pm 2} Y_{\ell m}(\hat{n}). \quad (1.22)$$

Forming linear combinations of the spin-2 harmonic coefficients as

$$a_{\ell m}^E = -\frac{1}{2}(a_{2, \ell m} + a_{-2, \ell m}); \quad (1.23a)$$

$$a_{\ell m}^B = \frac{i}{2}(a_{2, \ell m} - a_{-2, \ell m}), \quad (1.23b)$$

an invariant E mode and B mode can be defined by normal (zero-spin) inverse harmonic transformation [66]

$$E(\hat{n}) = \sum_{\ell=2}^{\infty} \sum_{m=-\ell}^{\ell} a_{\ell m}^E Y_{\ell m}(\hat{n}); \quad (1.24a)$$

$$B(\hat{n}) = \sum_{\ell=2}^{\infty} \sum_{m=-\ell}^{\ell} a_{\ell m}^B Y_{\ell m}(\hat{n}). \quad (1.24b)$$

The power spectra of the E and B modes can be defined using the corresponding $a_{\ell m}$ coefficients in the same way as for the temperature case. It is also possible to define cross-spectra, for example, TE or EB spectra. The E mode spectrum measured by *Planck* is shown in figure 1.2. The B mode spectrum measured by *Planck* is dominated by noise and systematic uncertainties, and it is compatible with 0.

It can be shown that gravitational waves in the early universe result in a CMB polarization state for which neither $a_{\ell m}^E$ nor $a_{\ell m}^B$ is zero. However, the contribution to the polarization from the normal scalar density perturbations has $a_{\ell m}^B = 0$ [13–15, 67]. The size of the B mode power spectrum is linked directly to the tensor-to-scalar ratio r .

Apart from this very desirable sensitivity of the B mode to the cosmological gravitational waves, the meaning of the E and B modes is not clear from the definition yet given. There are several different constructions of the E and B modes, variously based on spin-raising and spin-lowering operators [68, 69], the differential geometry of tensor fields [62, 70, 71], and the calculus of spin-2 functions [71–73]. These three approaches are all equivalent, but each one clarifies different aspects of the E–B decomposition. They will now be discussed in turn.

Spin-weighted functions

Functions on the sphere with a well-defined spin s , which transform under rotations as $f(\hat{n}) \xrightarrow{\Psi} e^{-is\Psi} f(\hat{n})$ (cf. equation (1.17)), are subject to spin-raising and spin-lowering operators, denoted \check{d} and $\bar{\check{d}}$, which raise or lower the spin [65]:

$$\check{d}f(\hat{n}) \xrightarrow{\Psi} e^{-i(s+1)\Psi} \check{d}f(\hat{n}); \quad (1.25a)$$

$$\bar{\check{d}}f(\hat{n}) \xrightarrow{\Psi} e^{-i(s-1)\Psi} \bar{\check{d}}f(\hat{n}). \quad (1.25b)$$

The spin-weighted spherical harmonics obey the identities

$$\check{d}_{(s)} Y_{\ell m}(\hat{n}) = \sqrt{(\ell-s)(\ell+s+1)}_{s+1} Y_{\ell m}(\hat{n}); \quad (1.26a)$$

$$\bar{\check{d}}_{(s)} Y_{\ell m}(\hat{n}) = -\sqrt{(\ell+s)(\ell-s+1)}_{s-1} Y_{\ell m}(\hat{n}). \quad (1.26b)$$

Spin-0 scalars can therefore be derived from the spin-2 field $Q(\hat{n}) \pm iU(\hat{n})$ by application of the raising and lowering operators. The results are complex-valued and are denoted by

$\mathcal{E}(\hat{n}) \pm i\mathcal{B}(\hat{n})$:

$$\mathcal{E}(\hat{n}) + i\mathcal{B}(\hat{n}) = -\tilde{\delta}^2(Q(\hat{n}) + iU(\hat{n})); \quad (1.27a)$$

$$\mathcal{E}(\hat{n}) - i\mathcal{B}(\hat{n}) = -\tilde{\delta}^2(Q(\hat{n}) - iU(\hat{n})). \quad (1.27b)$$

Combining equations (1.23) and (1.26), the scalar fields are given by

$$\mathcal{E}(\hat{n}) = \sum_{\ell=2}^{\infty} \sum_{m=-\ell}^{\ell} a_{\ell m}^E \sqrt{\frac{(\ell+2)!}{(\ell-2)!}} Y_{\ell m}(\hat{n}); \quad (1.28a)$$

$$\mathcal{B}(\hat{n}) = \sum_{\ell=2}^{\infty} \sum_{m=-\ell}^{\ell} a_{\ell m}^B \sqrt{\frac{(\ell+2)!}{(\ell-2)!}} Y_{\ell m}(\hat{n}). \quad (1.28b)$$

It is more usual to work with the $E(\hat{n})$ and $B(\hat{n})$ fields rather than $\mathcal{E}(\hat{n})$ and $\mathcal{B}(\hat{n})$. $E(\hat{n})$ and $B(\hat{n})$ exclude the ℓ weighting factor, but otherwise emerge from the spin-raising and lowering procedure in the same way, and naturally have the same desired property of rotational invariance.

Tensor harmonic expansion

The Stokes parameters can be organized into a 2×2 symmetric traceless tensor field, denoted $\mathcal{P}_{ab}(\hat{n})$. An explicit coordinate system is required to proceed in concrete terms. Normal spherical polar coordinates (θ, φ) is adopted in which the metric tensor is

$$g_{ab} = \begin{pmatrix} 1 & 0 \\ 0 & \sin^2(\theta) \end{pmatrix}. \quad (1.29)$$

Then $\mathcal{P}_{ab}(\hat{n})$ is¹

$$\mathcal{P}_{ab}(\hat{n}) = \frac{1}{\sqrt{2}} \begin{pmatrix} Q(\hat{n}) & U(\hat{n}) \sin(\theta) \\ U(\hat{n}) \sin(\theta) & -Q(\hat{n}) \sin^2(\theta) \end{pmatrix}. \quad (1.30)$$

It is a fact of differential geometry that any symmetric traceless tensor field on the sphere can be written as the sum of the gradient of some scalar field and the curl of another scalar field, which are called E and B respectively. The terms *gradient* and *curl* are used loosely to refer to tensor generalizations of these operations; explicitly, the decomposition is

$$\mathcal{P}_{ab} = \left(E_{:ab} - \frac{1}{2} g_{ab} E^{:c}_c \right) + \frac{1}{2} (B_{:ac} \epsilon_b^c + B_{:bc} \epsilon_a^c) \quad (1.31)$$

¹Different normalization and sign conventions have been used for \mathcal{P}_{ab} . This one agrees with [68] and [70], but not [62].

using the colon notation for covariant derivatives, and ϵ is the two dimensional Levi-Civita symbol

$$\epsilon_{ab} = \sqrt{g} \begin{pmatrix} 0 & 1 \\ -1 & 0 \end{pmatrix}. \quad (1.32)$$

Being scalars by construction, E and B can be represented in the harmonic domain as sums over spin-0 spherical harmonics (i.e., equation (1.24)). This decomposition is then inherited by \mathcal{P}_{ab} , which can be written as

$$\mathcal{P}_{ab}(\hat{n}) = \sum_{\ell=2}^{\infty} \sum_{m=-\ell}^{\ell} (a_{\ell m}^E (Y_{\ell m}^E)_{ab}(\hat{n}) + a_{\ell m}^B (Y_{\ell m}^B)_{ab}(\hat{n})), \quad (1.33)$$

where Y^E and Y^B denote the gradient and curl of the spherical harmonics:

$$(Y_{\ell m}^E)_{ab} = \sqrt{2} \sqrt{\frac{(\ell-2)!}{(\ell+2)!}} \left((Y_{\ell m})_{:ab} - \frac{1}{2} g_{ab} (Y_{\ell m})_{:c}^c \right); \quad (1.34a)$$

$$(Y_{\ell m}^B)_{ab} = \frac{1}{\sqrt{2}} \sqrt{\frac{(\ell-2)!}{(\ell+2)!}} \left((Y_{\ell m})_{:ac} \epsilon_b^c + (Y_{\ell m})_{:bc} \epsilon_a^c \right). \quad (1.34b)$$

The normalization coefficients of Y^E and Y^B have been chosen to make them orthonormal functions on the sphere. The harmonic coefficients $a_{\ell m}^E$ and $a_{\ell m}^B$ can be found from \mathcal{P}_{ab} by integration:

$$a_{\ell m}^E = \int \mathcal{P}_{ab}(\hat{n}) (Y_{\ell m}^E)^{ab}(\hat{n})^* d\hat{n}; \quad (1.35a)$$

$$a_{\ell m}^B = \int \mathcal{P}_{ab}(\hat{n}) (Y_{\ell m}^B)^{ab}(\hat{n})^* d\hat{n}. \quad (1.35b)$$

In spherical coordinates, Y^E and Y^B can be written explicitly in terms of spin-weighted spherical harmonics:

$$(Y_{\ell m}^E)_{ab} = \frac{1}{\sqrt{2}} \sqrt{\frac{(\ell-2)!}{(\ell+2)!}} \begin{pmatrix} W_{\ell m} & X_{\ell m} \sin(\theta) \\ X_{\ell m} \sin(\theta) & -W_{\ell m} \sin^2(\theta) \end{pmatrix}; \quad (1.36a)$$

$$(Y_{\ell m}^B)_{ab} = \frac{1}{\sqrt{2}} \sqrt{\frac{(\ell-2)!}{(\ell+2)!}} \begin{pmatrix} -X_{\ell m} & W_{\ell m} \sin(\theta) \\ W_{\ell m} \sin(\theta) & X_{\ell m} \sin^2(\theta) \end{pmatrix}, \quad (1.36b)$$

where

$$W_{\ell m}(\hat{n}) \pm iX_{\ell m}(\hat{n}) = \sqrt{\frac{(\ell+2)!}{(\ell-2)!}} {}_{\pm 2} Y_{\ell m}(\hat{n}). \quad (1.37)$$

Vector notation

Above, the spin-raising and spin-lowering operators were applied to $Q(\hat{n}) \pm iU(\hat{n})$ to recover scalars. It is also possible to work in reverse, writing $Q(\hat{n}) \pm iU(\hat{n})$ as the application of spin-raising and spin-lowering operators on some scalar potentials. The correct potentials turn out to be closely linked with the E and B modes. We can write

$$Q(\hat{n}) + iU(\hat{n}) = \partial^2(\Psi_E(\hat{n}) + i\Psi_B(\hat{n})); \quad (1.38a)$$

$$Q(\hat{n}) - iU(\hat{n}) = \bar{\partial}^2(\Psi_E(\hat{n}) - i\Psi_B(\hat{n})), \quad (1.38b)$$

where the potentials are

$$\Psi_E(\hat{n}) = - \sum_{\ell=2}^{\infty} \sum_{m=-\ell}^{\ell} \sqrt{\frac{(\ell-2)!}{(\ell+2)!}} a_{\ell m}^E Y_{\ell m}(\hat{n}); \quad (1.39a)$$

$$\Psi_B(\hat{n}) = - \sum_{\ell=2}^{\infty} \sum_{m=-\ell}^{\ell} \sqrt{\frac{(\ell-2)!}{(\ell+2)!}} a_{\ell m}^B Y_{\ell m}(\hat{n}). \quad (1.39b)$$

These expressions can be recovered by straightforward application of identities obeyed by the spin-weighted spherical harmonics. Introducing differential vector operators D_E and D_B defined as

$$D_E = \frac{1}{2} \begin{pmatrix} \partial^2 + \bar{\partial}^2 \\ -i(\partial^2 - \bar{\partial}^2) \end{pmatrix}; \quad (1.40a)$$

$$D_B = \frac{1}{2} \begin{pmatrix} i(\partial^2 - \bar{\partial}^2) \\ \partial^2 - \bar{\partial}^2 \end{pmatrix}, \quad (1.40b)$$

then equation (1.38) can be written in terms of the Stokes vector $\vec{P} = \begin{pmatrix} Q \\ U \end{pmatrix}$ as

$$\vec{P} = D_E \Psi_E + D_B \Psi_B. \quad (1.41)$$

This is analogous to the gradient/curl decomposition in equation (1.33). D_E and D_B are spin-2 versions of the divergence and curl. They satisfy the identities

$$D_E^\dagger \cdot D_B = 0; \quad (1.42a)$$

$$D_B^\dagger \cdot D_B = 0; \quad (1.42b)$$

$$D_E^\dagger \cdot D_E = \nabla^2(\nabla^2 + 2); \quad (1.42c)$$

$$D_B^\dagger \cdot D_B = \nabla^2(\nabla^2 + 2). \quad (1.42d)$$

The Stokes-space E mode of \vec{P} , which is $\vec{P}_E = D_E \Psi_E$, therefore satisfies $D_B^\dagger \cdot \vec{P}_E = 0$: it has no curl. The Stokes-space B mode, $\vec{P}_B = D_B \Psi_B$, likewise has no divergence. This is the origin of the E/B terminology, made by analogy with electromagnetism.

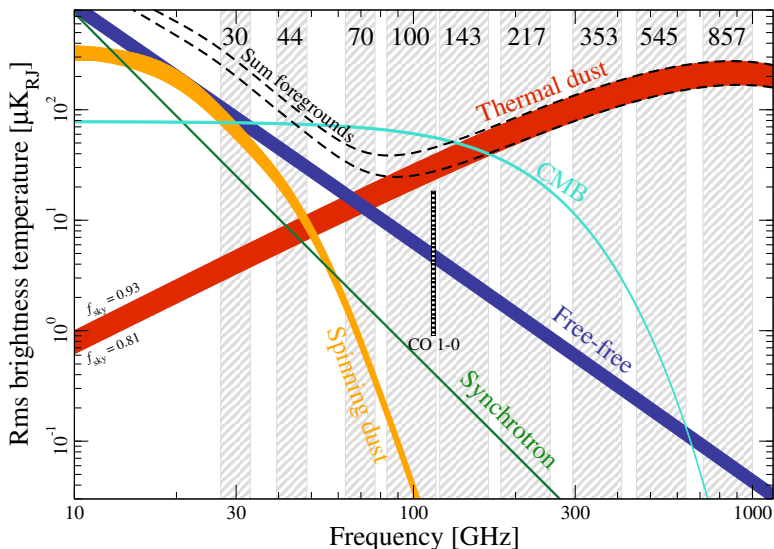


Figure 1.4: Frequency spectra of the main Galactic foregrounds. Figure taken from [3]. The amplitudes plotted are averages over the full sky; however, the foregrounds are not isotropic.

1.4 GALACTIC AND EXTRA-GALACTIC FOREGROUNDS

The CMB is not the only source of microwave radiation in the sky. There are other sources of microwave radiation from the late universe, generally concentrated in stars and galaxies. Although these radiation sources are interesting in their own right, and they render important datasets to astrophysics and the study of the interstellar medium, in CMB science their main role is obscuring the background signal, and they are termed *foregrounds*. The brightest foregrounds are from the Milky Way Galaxy. The strongest foreground sources are synchrotron radiation from relativistic electrons accelerated in the magnetic field of the Galaxy, free–free emission (*Bremsstrahlung*) from electrons deflected by other atoms, and thermal dust emission and spinning dust emission from dust grains in the interstellar medium. Other weaker sources include line emission from carbon monoxide.

The intensities of different foregrounds vary differently with frequency, and they also vary differently from the CMB. This different frequency behavior is one of the keys that enable foreground subtraction from multi-frequency observations, which is discussed below. The approximate frequency spectra of the main Galactic foregrounds in the recent *Planck* data [3] are shown in figure 1.4. Synchrotron and free–free radiation dominate

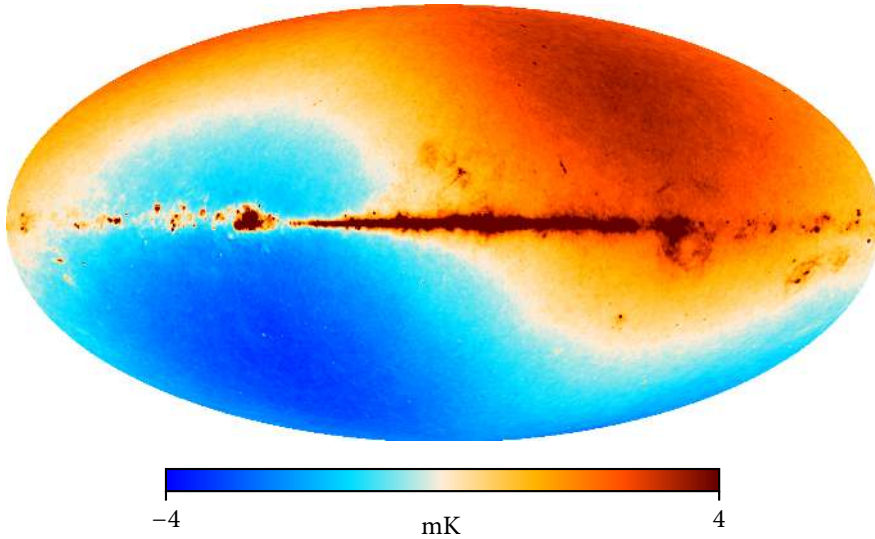


Figure 1.5: The sky observed by *Planck* at $\nu = 30$ GHz. The map shown is the reconstructed LFI posterior mean map released by BeyondPlanck [74]. The two main microwave signals are the kinematic dipole and the Milky Way Galaxy.

at lower frequencies, while thermal dust is the dominant signal at high frequencies. The CMB itself is most pronounced relative to the foregrounds in the 70 and 100 GHz bands.

The spectral behavior illustrated in figure 1.4 should not be allowed to conceal the fact that there is significant spatial variation in the foreground maps [75], which includes variation of the spectral indices across the sky [76].

Polarized foregrounds

There are also foreground sources in polarization [77, 78]. Expressed in terms of the percentage of the total intensity, the synchrotron and thermal dust foregrounds can be significantly polarized, up to around the 20%–40% level [79]. Synchrotron and thermal dust emission are the dominant polarization signals at low and high frequencies respectively. It is also suggested that Galactic magnetic dust radiation could be significantly polarized; these are joined by anomalous microwave emission, believed to result from small spinning dust grains [80–84]. Polarized dust emission has been found to extend to high Galactic latitudes [85], and it appears that there are no parts of the sky that are free from foreground contamination.

Research on the polarized foregrounds has focused on their spectral behavior [86],

which underlies the main component separation methods (discussed below). Spatial variation and structure has also been detected in the polarized foregrounds [87–89]. Other important results include the relative contributions of the polarized foregrounds to the E and B modes, which is linked to research on the physics of the interstellar medium [90–92].

Foreground polarization emission, especially contributing to the B mode, is a significant obstacle to current and upcoming CMB polarization experiments, both ground-based and space-based [93, 94]. Methods for identifying and subtracting contributions from foregrounds to the B mode have been proposed [95–97]. These methods generally work by assuming statistical isotropy of the primordial B mode.

The polarized foregrounds remain poorly understood. In preparation for the upcoming ground-based experiments, the most important goal is understanding the spatial behavior and statistical properties of the polarized foregrounds [94].

Component separation

The subtraction of the foreground signals from observed data to produce maps of the cosmic microwave background is known as component separation. A variety of different algorithms have been proposed for performing component separation. The *Planck* collaboration implements and publishes four component separation products: Commander, NILC, SEVEM, and SMICA [98, 99]. All these methods produce maps in both temperature and polarization. The maps are also each associated with a “confidence mask”, which arbitrarily excludes the most corrupted and uncertain regions of the Galactic plane and point sources.

Commander In the Commander method [100, 101], the frequency- ν data at each pixel p , denoted $d_\nu(p)$, is modeled as a linear combination of projected and rescaled astrophysical foregrounds, plus a noise term $n_\nu(p)$:

$$d_\nu(p) = g_\nu \sum_{c=1}^{N_c} F_\nu(\beta_c) T(p) a_c + n_\nu(p), \quad (1.43)$$

where the different components are indexed by c , each having amplitude a_c ; every component is transformed by the map projection operator $T(p)$ and a frequency scaling operator depending on the spectral index $F_\nu(\beta_c)$. There is also an overall calibration scaling per frequency channel, denoted g_ν . The implied posterior distribution is then sampled using Gibbs sampling. Originally based on map-space data, Commander is more recently implemented in harmonic space [102].

NILC The Needlet Internal Linear Combination method [103, 104] is a development of well-known ILC methods adopted by WMAP for component separation. A basis of

needlets, a type of spherical wavelets with desirable properties, is used to decompose the input maps; in this basis, the linear combination with minimal variance is then found.

SEVEM The Spectral Estimation Via Expectation Maximization [105] is a real-space, template-based method. Templates can be constructed internally by subtraction of different frequency maps. The data is represented as

$$X_\nu(p) = d_\nu(p) - \sum_{i=1}^{N_i} \alpha_i t_i(p), \quad (1.44)$$

where $X \in \{T, Q, U\}$ is the CMB component, and $t_i(p)$ are the map-domain templates. The coefficients α_i are fitted by variance minimization. The method produces CMB maps depending on frequency ν .

SMICA The Spectral Matching Independent Component Analysis method [106, 107] works by producing a linear combination of the frequency channels in the harmonic domain. The weights are determined by variance minimization, in which the covariance matrix is approximated using a maximum-likelihood algorithm under an isotropic Gaussian model.

There are multiple varieties and technical improvements to the component separation methods that have been incorporated in the latest *Planck* releases. Nevertheless, all component separation methods produce maps that are contaminated by strong foreground residuals, especially near the Galactic plane. In addition to the confidence masks associated with each map, a common mask is also published for more conservative applications.

Gravitational lensing

Soon after the introduction of the E–B decomposition, it was observed that gravitational lensing induces B modes even when only a primordial E mode signal is present [108, 109]. Effectively, the native E modes are distorted due to gravitational lensing by interceding matter, resulting in curl patterns which are interpreted as B modes; other effects of gravitational lensing on the CMB include a small non-Gaussian component [110]. Strategies for delensing exist [111], and the CMB can be delensed using measurements of the cosmic infrared background [112] or with galaxy surveys [113, 114].

1.5 DATA REPRESENTATION

The mathematical description of the CMB is naturally continuous and involves the non-trivial geometry of the sphere. Observations of the CMB, however, result in discrete data.

Representations of the data in a format amenable to spherical data analysis, and especially to spherical harmonic transformations, are therefore very desirable.

The COBE mission adopted a quadrilateralized spherical cube mapping, in which equal-area pixels on the sphere are projected onto an inscribed cube. The six base pixels, corresponding to the six faces of the inscribed cube, are divided into four subpixels, which are in turn divided into four subpixels each, and so on, resulting in a total of 6×2^{2N} pixels, where $N = 1, 2, 3, \dots$ is a number of divisions specifying the resolution.

The advantage of equal-area pixels is that integration requires no weights. However, a weakness of the COBE quadrilateralized spherical cube scheme is that the pixels do not lie on rings of equal latitude. The computation and storage costs of evaluating spherical harmonics on a range of latitudes are substantial, especially with modern high-resolution data.

HEALPix

HEALPix [115] solves this problem by ensuring pixels lie on lines of equal latitude. HEALPix stands for “Hierarchical Equal Area iso-Latitude Pixelization”, and was developed for the WMAP and *Planck* experiments, but is now widely used for astrophysical data [63, 116]. Several implementations exist. The C++ implementation can be accessed through a Python wrapper [117]; this is the version used throughout this thesis.

In HEALPix, 12 base pixels are subdivided recursively into 4 subpixels each, similarly to the quadrilateralized spherical cube scheme. Rather than the number of divisions, the resolution is normally specified in terms of an N_{side} parameter, which is the number of pixels along one side of one of the base pixels. The total number of pixels is therefore $12 \times N_{\text{side}}^2$. The N_{side} parameter is a positive power of 2, i.e. $N_{\text{side}} = 1, 2, 4, 8, 16, \dots$. Most full-resolution *Planck* data products are pixelized at $N_{\text{side}} = 2048$, corresponding to about 50 million pixels.

HEALPix is associated with a pixel ordering, which means that a map can be stored in a one-dimensional array object. In the RING ordering, pixels are numbered starting from the North Pole, looping around and then stepping down through the iso-latitude rings. In the NESTED ordering, pixels are numbered in a recursive scheme through successive quadrilateral subpixel divisions. Maps do not need to be rasterized and include a metadata flag labeling which of the two ordering schemes is in use. The different ordering schemes can have significant impacts on the performance of different algorithms.

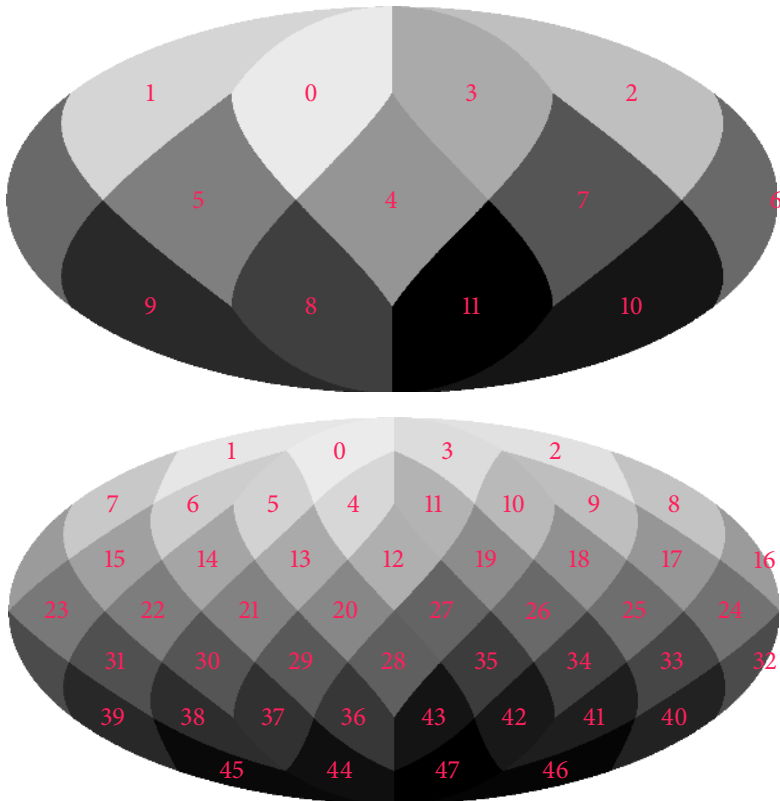


Figure 1.6: Upper panel: the 12 base pixels of the HEALPix scheme. Lower panel: the HEALPix map at $N_{\text{side}} = 2$, with the pixels numbered in the RING ordering.

2 E AND B MODES OF THE STOKES PARAMETERS

The E and B modes of the polarization field are normally conceived in a harmonic setting, where they emerge from the decomposition of the Stokes field on the sphere into spin-weighted spherical harmonics and the construction of scalar and pseudo-scalar modes in harmonic space, discussed in section 1.3. The great value of this decomposition is that scalar perturbations do not produce a B mode signal; instead, a B mode is expected from tensor perturbations due to a gravitational wave background in the early universe [13–15].

In addition to the normal harmonic method, it is possible to construct E and B maps directly out of Q and U . The E–B decomposition is realized as

$$\begin{pmatrix} Q \\ U \end{pmatrix} = \begin{pmatrix} Q_E \\ U_E \end{pmatrix} + \begin{pmatrix} Q_B \\ U_B \end{pmatrix}. \quad (2.1)$$

This conception of the E–B decomposition is implied by equation (1.41), although there the interest was the scalar E and B potentials. In this chapter, the subject is the Stokes-space E and B modes themselves, which are named the *E and B families*.

E and B modes in the space of the Stokes parameters are discussed briefly in some early works, e.g. [118], and they have also appeared in [119]. But they remain understudied from an analytic point of view, and their potential applications for data analysis are unexploited. There are several specific objectives of the study presented here. The first is the representation of the E–B decomposition as a linear convolution in the map space, and the computation of the corresponding convolution kernels. These kernels, which are 2×2 matrices denoted $G_E(\hat{n}, \hat{n}')$ and $G_B(\hat{n}, \hat{n}')$, link the input polarization data (Q, U) to the output E and B modes via integration over the full sky:

$$\begin{pmatrix} Q_E(\hat{n}) \\ U_E(\hat{n}) \end{pmatrix} = \int G_E(\hat{n}, \hat{n}') \begin{pmatrix} Q(\hat{n}') \\ U(\hat{n}') \end{pmatrix} d\hat{n}'; \quad (2.2a)$$

$$\begin{pmatrix} Q_B(\hat{n}) \\ U_B(\hat{n}) \end{pmatrix} = \int G_B(\hat{n}, \hat{n}') \begin{pmatrix} Q(\hat{n}') \\ U(\hat{n}') \end{pmatrix} d\hat{n}'. \quad (2.2b)$$

The kernels therefore describe the influence of the point \hat{n} on the point \hat{n}' , and they provide a concrete and visualizable insight into the geometric workings of the E–B decomposition.

The second objective is the design of new estimators which characterize the E and B modes. Since the E and B families retain the two Stokes dimensions, it is possible to define polarization intensities and polarization angles associated with each of the E and B modes separately. These estimators are applied to polarized foreground analysis, where they reveal new features of the thermal dust foregrounds. The analysis is illustrative of the utility of the estimators.

These results underlie much of the remainder of the thesis. The map-space E–B decomposition is the foundation of a new leakage correction method proposed in chapter 3. The statistics of the polarization angle, including the specific statistical properties of the E and B polarization angles, is the subject of chapter 4, and the E and B polarization intensities are involved in the non-polarized point analysis in chapter 5.

The basic ideas of the map-space E–B decomposition and the E and B convolution kernels were published in [16], together with the application to polarized foreground analysis. Shortly thereafter, these subjects were also discussed in a work by Rotti & Huffenberger [69], and they were applied to filamentary structures. The formalisms of [16] and [69] contain slight differences from each other, but they are completely compatible.

2.1 E–B DECOMPOSITION OF THE STOKES VECTOR

The Stokes vector holding the Q and U Stokes parameters is

$$\vec{P} = \begin{pmatrix} Q \\ U \end{pmatrix}. \quad (2.3)$$

Q and U are real numbers. But, the Stokes vector field on the sphere, $\vec{P}(\hat{n})$, does not transform as an \mathbb{R}^2 vector under coordinate transformations: instead, Q and U are mixed according to the rules of a spin-2 field, as discussed in section 1.3. This is a slightly subtle point because \vec{P} will sometimes be treated as a “vector” in an operational sense; for example, 2×2 matrices will multiply it.

Under the decomposition of equation (2.1), the Stokes parameters can be split into E and B components separately:

$$Q = Q_E + Q_B \quad (2.4a)$$

$$U = U_E + U_B \quad (2.4b)$$

The division is determined by the requirement that (Q_E, U_E) will, when treated as an input polarization map under the traditional harmonic space construction, yield only an E mode, and (Q_B, U_B) only a B mode. The traditional expansion of $Q(\hat{n}) + iU(\hat{n})$ into

spin ± 2 spherical harmonics is:¹

$$Q(\hat{n}) \pm iU(\hat{n}) = \sum_{\ell, m} a_{\pm 2, \ell m \pm 2} Y_{\ell m}(\hat{n}), \quad (2.5)$$

and the coefficients are computed in the standard way:

$$a_{\pm 2, \ell m} = \int (Q(\hat{n}) + iU(\hat{n}))_{\pm 2} Y_{\ell m}(\hat{n})^* d\hat{n}. \quad (2.6)$$

The separate equations for Q and U are

$$Q(\hat{n}) = \frac{1}{2} \left(\sum_{\ell, m} a_{2, \ell m 2} Y_{\ell m}(\hat{n}) + \sum_{\ell, m} a_{-2, \ell m - 2} Y_{\ell m}(\hat{n}) \right); \quad (2.7a)$$

$$U(\hat{n}) = \frac{1}{2i} \left(\sum_{\ell, m} a_{2, \ell m 2} Y_{\ell m}(\hat{n}) - \sum_{\ell, m} a_{-2, \ell m - 2} Y_{\ell m}(\hat{n}) \right). \quad (2.7b)$$

In terms of the $a_{\pm 2, \ell m}$ coefficients, the E and B modes in harmonic space are

$$a_{\ell m}^E = -\frac{a_{2, \ell m} + a_{-2, \ell m}}{2}; \quad (2.8a)$$

$$a_{\ell m}^B = -\frac{a_{2, \ell m} - a_{-2, \ell m}}{2i}. \quad (2.8b)$$

Therefore, the condition of zero E or B mode implies a constraint on the $a_{\pm 2, \ell m}$ coefficients. Zero E mode corresponds to

$$a_{2, \ell m} = -a_{-2, \ell m}, \quad (2.9)$$

and zero B mode corresponds to

$$a_{2, \ell m} = a_{-2, \ell m}. \quad (2.10)$$

Substituting these constraints in equation (2.7) yields respectively Stokes parameters with no E and no B component, and therefore they can be associated solely with the B and the E mode:

$$Q_{E=0}(\hat{n}) = Q_B(\hat{n}) = \frac{1}{2} \sum_{\ell, m} a_{2, \ell m} ({}_2Y_{\ell m}(\hat{n}) - {}_{-2}Y_{\ell m}(\hat{n})); \quad (2.11a)$$

$$U_{E=0}(\hat{n}) = U_B(\hat{n}) = \frac{1}{2i} \sum_{\ell, m} a_{2, \ell m} ({}_2Y_{\ell m}(\hat{n}) + {}_{-2}Y_{\ell m}(\hat{n})); \quad (2.11b)$$

$$Q_{B=0}(\hat{n}) = Q_E(\hat{n}) = \frac{1}{2} \sum_{\ell, m} a_{2, \ell m} ({}_2Y_{\ell m}(\hat{n}) + {}_{-2}Y_{\ell m}(\hat{n})); \quad (2.11c)$$

$$U_{B=0}(\hat{n}) = U_E(\hat{n}) = \frac{1}{2i} \sum_{\ell, m} a_{2, \ell m} ({}_2Y_{\ell m}(\hat{n}) - {}_{-2}Y_{\ell m}(\hat{n})). \quad (2.11d)$$

¹In this chapter, $\sum_{\ell, m}$ generally stands for $\sum_{\ell=2}^{\ell_{\max}} \sum_{m=-\ell}^{\ell}$, where ℓ_{\max} can be ∞ , but it is not assumed to be. But see the discussions on pages 27 and 29.

These sum together to the original, i.e.

$$Q_E(\hat{n}) + Q_B(\hat{n}) = Q(\hat{n}); \quad (2.12a)$$

$$U_E(\hat{n}) + U_B(\hat{n}) = U(\hat{n}). \quad (2.12b)$$

Defining linear combinations of the spin-weighted spherical harmonics,

$$F_{\ell m}^+(\hat{n}) = -\frac{1}{2}({}_2Y_{\ell m}(\hat{n}) + {}_{-2}Y_{\ell m}(\hat{n})); \quad (2.13a)$$

$$F_{\ell m}^-(\hat{n}) = -\frac{1}{2i}({}_2Y_{\ell m}(\hat{n}) - {}_{-2}Y_{\ell m}(\hat{n})), \quad (2.13b)$$

the E and B Stokes parameters can be written as

$$Q_E(\hat{n}) = \sum_{\ell, m} a_{\ell m}^E F_{\ell m}^+(\hat{n}); \quad (2.14a)$$

$$U_E(\hat{n}) = \sum_{\ell, m} a_{\ell m}^E F_{\ell m}^-(\hat{n}); \quad (2.14b)$$

$$Q_B(\hat{n}) = -\sum_{\ell, m} a_{\ell m}^B F_{\ell m}^-(\hat{n}); \quad (2.14c)$$

$$U_B(\hat{n}) = \sum_{\ell, m} a_{\ell m}^B F_{\ell m}^+(\hat{n}). \quad (2.14d)$$

Therefore the E Stokes parameters are functions of $a_{\ell m}^E$ alone, and similarly for B. The decomposition is linear and orthogonal. The E and B families are:

$$\vec{P}_E(\hat{n}) = \begin{pmatrix} Q_E(\hat{n}) \\ U_E(\hat{n}) \end{pmatrix}; \quad (2.15a)$$

$$\vec{P}_B(\hat{n}) = \begin{pmatrix} Q_B(\hat{n}) \\ U_B(\hat{n}) \end{pmatrix}. \quad (2.15b)$$

Polarization intensities and polarization angles

Now that the E and B modes are each expressed as Stokes vectors, it is possible to define a polarization intensity and a polarization angle associated with each mode, as follows:

$$P_E = \sqrt{Q_E^2 + U_E^2}; \quad (2.16a)$$

$$P_B = \sqrt{Q_B^2 + U_B^2}; \quad (2.16b)$$

$$\psi_E = \frac{1}{2} \arctan\left(\frac{U_E}{Q_E}\right); \quad (2.16c)$$

$$\psi_B = \frac{1}{2} \arctan\left(\frac{U_B}{Q_B}\right). \quad (2.16d)$$

The total polarization intensity can be expanded in terms of the E and B polarization intensities, but the nonlinearity introduces an extra term:

$$P^2 = Q^2 + U^2 = P_E^2 + P_B^2 + \Delta_{EB}, \quad (2.17)$$

where

$$\Delta_{EB} = 2(Q_E Q_B + U_E U_B). \quad (2.18)$$

The cross term Δ_{EB} can be rewritten in terms of the polarization angles, as

$$\Delta_{EB} = 2P_E P_B \cos(2\psi_E - 2\psi_B), \quad (2.19)$$

or, returning to the harmonic expansions,

$$\Delta_{EB} = 2 \sum_{\ell, m} \sum_{\ell', m'} a_{\ell m}^E (a_{\ell m}^B)^* (F_{\ell m}^- (F_{\ell' m'}^+)^* - F_{\ell m}^+ (F_{\ell' m'}^-)^*). \quad (2.20)$$

From equation (2.20) it is clear that Δ_{EB} is composed entirely of cross quadratic E–B terms. The mixing coefficients are

$$G_{\ell m \ell' m'} = F_{\ell m}^- (F_{\ell' m'}^+)^* - F_{\ell m}^+ (F_{\ell' m'}^-)^*. \quad (2.21)$$

2.2 REAL-SPACE CONVOLUTION KERNELS

The decomposition of the Stokes vector presented above assumes the existence of full-sky data. \vec{P}_E and \vec{P}_B have been expressed in terms of harmonic coefficients. However, it is possible to recast the equations to define the E and B families locally through linear convolution of the Stokes vector. Apart from theoretical interest, this enables the E and B families to be calculated using partial sky data, without the need to perform any harmonic transformation. They are still subject to E–B leakage effects.

Integral representation of the E–B decomposition

The harmonic coefficients $a_{\pm 2, \ell m}$ are calculated by integration of the Stokes parameters in equation (2.6). Combining this with the definitions of $a_{\ell m}^E$ and $a_{\ell m}^B$ in equation (2.8), these can be written as

$$a_{\ell m}^E = \int (Q(\hat{n}) F_{\ell m}^+(\hat{n})^* + U(\hat{n}) F_{\ell m}^-(\hat{n})^*) d\hat{n}; \quad (2.22a)$$

$$a_{\ell m}^B = \int (-Q(\hat{n}) F_{\ell m}^-(\hat{n})^* + U(\hat{n}) F_{\ell m}^+(\hat{n})^*) d\hat{n}. \quad (2.22b)$$

Then, substituting into equation (2.14),

$$Q_E(\hat{n}) = \int (G_1(\hat{n}, \hat{n}')Q(\hat{n}') + G_2(\hat{n}, \hat{n}')U(\hat{n}')) d\hat{n}' \quad (2.23a)$$

$$U_E(\hat{n}) = \int (G_3(\hat{n}, \hat{n}')Q(\hat{n}') + G_4(\hat{n}, \hat{n}')U(\hat{n}')) d\hat{n}'; \quad (2.23b)$$

$$Q_B(\hat{n}) = \int (G_4(\hat{n}, \hat{n}')Q(\hat{n}') - G_3(\hat{n}, \hat{n}')U(\hat{n}')) d\hat{n}'; \quad (2.23c)$$

$$U_B(\hat{n}) = \int (-G_2(\hat{n}, \hat{n}')Q(\hat{n}') + G_1(\hat{n}, \hat{n}')U(\hat{n}')) d\hat{n}'. \quad (2.23d)$$

where the coefficients G_i are defined as

$$G_1(\hat{n}, \hat{n}') = \sum_{\ell, m} F_{\ell m}^+(\hat{n})F_{\ell m}^+(\hat{n}')^*; \quad (2.24a)$$

$$G_2(\hat{n}, \hat{n}') = \sum_{\ell, m} F_{\ell m}^+(\hat{n})F_{\ell m}^-(\hat{n}')^*; \quad (2.24b)$$

$$G_3(\hat{n}, \hat{n}') = \sum_{\ell, m} F_{\ell m}^-(\hat{n})F_{\ell m}^+(\hat{n}')^*; \quad (2.24c)$$

$$G_4(\hat{n}, \hat{n}') = \sum_{\ell, m} F_{\ell m}^-(\hat{n})F_{\ell m}^-(\hat{n}')^*. \quad (2.24d)$$

The decomposition in equations (2.23) can be written as an integral transform:

$$\vec{P}_E(\hat{n}) = \int G_E(\hat{n}, \hat{n}')\vec{P}(\hat{n}') d\hat{n}'; \quad (2.25a)$$

$$\vec{P}_B(\hat{n}) = \int G_B(\hat{n}, \hat{n}')\vec{P}(\hat{n}') d\hat{n}'. \quad (2.25b)$$

G_E and G_B are the E and B kernels, which weight the contribution of the polarization intensity at \hat{n} to E or B at the point \hat{n}' . The kernels can be written as sums over spherical harmonics. The explicit matrix representation is

$$G_E(\hat{n}, \hat{n}') = \begin{pmatrix} G_1(\hat{n}, \hat{n}') & G_2(\hat{n}, \hat{n}') \\ G_3(\hat{n}, \hat{n}') & G_4(\hat{n}, \hat{n}') \end{pmatrix}; \quad (2.26a)$$

$$G_B(\hat{n}, \hat{n}') = \begin{pmatrix} G_4(\hat{n}, \hat{n}') & -G_3(\hat{n}, \hat{n}') \\ -G_2(\hat{n}, \hat{n}') & G_1(\hat{n}, \hat{n}') \end{pmatrix}. \quad (2.26b)$$

Properties of the E/B kernels

Some analytic properties of the kernels deserve to be worked out first, before attempting to compute them. The main tool is the completeness of the spin-weighted spherical harmonics,

$$\sum_{\ell=2}^{\infty} \sum_{m=-\ell}^{\ell} {}_s Y_{\ell m}(\hat{n}')^* {}_s Y_{\ell m}(\hat{n}) = \delta(\hat{n} - \hat{n}'), \quad (2.27)$$

together with other standard identities. In equation (2.27), the sum over ℓ is taken to ∞ . Only in this limit is a true delta function recovered. However, as discussed below, the notion of a band-limited delta function is important in any practical application of the theory to pixelized data. A band-limited delta function is therefore defined as the truncation of the series at some finite ℓ_{\max} :

$$\sum_{\ell=2}^{\ell_{\max}} \sum_{m=-\ell}^{\ell} {}_2Y_{\ell m}(\hat{n}')^* {}_2Y_{\ell m}(\hat{n}) = \delta^{\ell_{\max}}(\hat{n} - \hat{n}'). \quad (2.28)$$

The behaviour of $\delta^{\ell_{\max}}(\hat{n} - \hat{n}')$ on angular scales $\ell < \ell_{\max}$ is comparable to a delta function, and as the value of ℓ_{\max} is increased, the corresponding $\delta^{\ell_{\max}}(\hat{n} - \hat{n}')$ becomes increasingly localized. Generally, the ℓ_{\max} superscript can be omitted in the equations, which usually apply to the normal and band-limited delta functions alike.

First, it is claimed that the kernels are real-valued. This is not obvious from the equations above. But, choosing G_1 in particular, it can be written

$$G_1(\hat{n}, \hat{n}') = \sum_{\ell, m} F_{+, \ell m}(\hat{n}) F_{+, \ell m}^*(\hat{n}') \quad (2.29a)$$

$$= \frac{1}{2} \delta(\hat{n} - \hat{n}') + \frac{1}{4} \sum_{\ell, m} ({}_2Y_{\ell m}(\hat{n}) {}_{-2}Y_{\ell m}(\hat{n}')^* + {}_{-2}Y_{\ell m}(\hat{n}) {}_2Y_{\ell m}(\hat{n}')^*). \quad (2.29b)$$

The sum over m is split into three parts:

$$\sum_{\ell, m} = \sum_{\ell} \left(\sum_{m>0} + \sum_{m<0} + \sum_{m=0} \right). \quad (2.30)$$

The sum over negative m can be modified using the identity $({}_sY_{\ell m})^* = (-1)^{s+m} {}_{-s}Y_{\ell(-m)}$:

$$\begin{aligned} & \sum_{m<0} ({}_2Y_{\ell m}(\hat{n}) {}_{-2}Y_{\ell m}(\hat{n}')^* + {}_{-2}Y_{\ell m}(\hat{n}) {}_2Y_{\ell m}(\hat{n}')^*) \\ &= \sum_{m<0} \left(-{}_2Y_{\ell(-m)}(\hat{n})^* {}_2Y_{\ell(-m)}(\hat{n}') + {}_2Y_{\ell(-m)}(\hat{n})^* {}_{-2}Y_{\ell(-m)}(\hat{n}') \right) \end{aligned} \quad (2.31a)$$

$$= \sum_{m>0} \left(-{}_2Y_{\ell m}(\hat{n})^* {}_2Y_{\ell m}(\hat{n}') + {}_2Y_{\ell m}(\hat{n})^* {}_{-2}Y_{\ell m}(\hat{n}') \right) \quad (2.31b)$$

$$= \left(\sum_{m>0} ({}_2Y_{\ell m}(\hat{n}) {}_{-2}Y_{\ell m}(\hat{n}')^* + {}_{-2}Y_{\ell m}(\hat{n}) {}_2Y_{\ell m}(\hat{n}')^*) \right)^*. \quad (2.31c)$$

Therefore the $m > 0$ and $m < 0$ sums are complex conjugates to each other, and together they are real. Furthermore, the $m = 0$ term can also be modified using the same identity:

$${}_2Y_{\ell 0}(\hat{n}) {}_{-2}Y_{\ell 0}(\hat{n}')^* + {}_{-2}Y_{\ell 0}(\hat{n}) {}_2Y_{\ell 0}(\hat{n}')^* = {}_2Y_{\ell 0}(\hat{n}) {}_2Y_{\ell 0}(\hat{n}') + {}_2Y_{\ell 0}(\hat{n})^* {}_2Y_{\ell 0}(\hat{n}')^*, \quad (2.32)$$

which is a sum of complex conjugates and is therefore also real. Therefore each term in the \sum_ℓ is real, and G_1 is real.

By similar calculations it can be shown that G_2 , G_3 , and G_4 are also real.

Furthermore, it can be shown that $G_2 = G_3$. This is also not obvious from equation (2.24). The difference can be written

$$G_2(\hat{n}, \hat{n}') - G_3(\hat{n}, \hat{n}') = \sum_{\ell, m} F_{+, \ell m}(\hat{n}) F_{-, \ell m}^*(\hat{n}') - \sum_{\ell, m} F_{-, \ell m}(\hat{n}) F_{+, \ell m}^*(\hat{n}') \quad (2.33a)$$

$$\begin{aligned} &= \frac{1}{4i} \sum_{\ell, m} ({}_2Y_{\ell m}(\hat{n}) {}_2Y_{\ell m}(\hat{n}')^* - {}_2Y_{\ell m}(\hat{n}) {}_{-2}Y_{\ell m}(\hat{n}')^* \\ &\quad + {}_{-2}Y_{\ell m}(\hat{n}) {}_2Y_{\ell m}(\hat{n}')^* - {}_{-2}Y_{\ell m}(\hat{n}) {}_{-2}Y_{\ell m}(\hat{n}')^* \\ &\quad - {}_2Y_{\ell m}(\hat{n}) {}_2Y_{\ell m}(\hat{n}')^* + {}_2Y_{\ell m}(\hat{n}) {}_{-2}Y_{\ell m}(\hat{n}')^* \\ &\quad - {}_{-2}Y_{\ell m}(\hat{n}) {}_2Y_{\ell m}(\hat{n}')^* + {}_{-2}Y_{\ell m}(\hat{n}) {}_{-2}Y_{\ell m}(\hat{n}')^*) \end{aligned} \quad (2.33b)$$

$$= 0. \quad (2.33c)$$

All terms cancel out.¹

Finally, it can be shown, by similar techniques, that

$$G_1(\hat{n}, \hat{n}') + G_4(\hat{n}, \hat{n}') = \delta(\hat{n} - \hat{n}'). \quad (2.34)$$

As discussed above, when a finite ℓ_{\max} is in use, this is a band-limited delta function.

Therefore, the kernels can be written concisely and coordinately in terms of delta functions and a single symmetric matrix, denoted $G(\hat{n}, \hat{n}')$,²

$$G_E(\hat{n}, \hat{n}') = \frac{1}{2} \delta(\hat{n} - \hat{n}') + G(\hat{n}, \hat{n}'); \quad (2.35a)$$

$$G_B(\hat{n}, \hat{n}') = \frac{1}{2} \delta(\hat{n} - \hat{n}') - G(\hat{n}, \hat{n}'), \quad (2.35b)$$

where

$$G(\hat{n}, \hat{n}') = \begin{pmatrix} g_+(\hat{n}, \hat{n}') & -ig_-(\hat{n}, \hat{n}') \\ -ig_-(\hat{n}, \hat{n}') & -g_+(\hat{n}, \hat{n}') \end{pmatrix}, \quad (2.36)$$

and

$$g_{\pm}(\hat{n}, \hat{n}') = \frac{1}{4} \sum_{\ell, m} ({}_2Y_{\ell m}(\hat{n}) {}_{-2}Y_{\ell m}(\hat{n}')^* \pm {}_{-2}Y_{\ell m}(\hat{n}) {}_2Y_{\ell m}(\hat{n}')^*). \quad (2.37)$$

It is remarked that G is traceless,

$$G(\hat{n}, \hat{n}') = \frac{1}{2} (G_E(\hat{n}, \hat{n}') - G_B(\hat{n}, \hat{n}')). \quad (2.38)$$

¹This original description in [16] is therefore overspecified, but it is the description that emerges naturally from the construction of the kernels in the preceding manner.

²It is understood in equation (2.35) and elsewhere that the delta function is multiplied by a 2×2 identity matrix.

In terms of the original kernel components G_i , the G kernel is

$$G(\hat{n}, \hat{n}') = \begin{pmatrix} G_1(\hat{n}, \hat{n}') - \frac{1}{2}\delta(\hat{n} - \hat{n}') & G_2(\hat{n}, \hat{n}') \\ G_2(\hat{n}, \hat{n}') & -G_1(\hat{n}, \hat{n}') + \frac{1}{2}\delta(\hat{n} - \hat{n}') \end{pmatrix} \quad (2.39a)$$

$$= \begin{pmatrix} -G_4(\hat{n}, \hat{n}') + \frac{1}{2}\delta(\hat{n} - \hat{n}') & G_2(\hat{n}, \hat{n}') \\ G_2(\hat{n}, \hat{n}') & G_4(\hat{n}, \hat{n}') - \frac{1}{2}\delta(\hat{n} - \hat{n}') \end{pmatrix}. \quad (2.39b)$$

This representation will be returned to in the next chapter. It suffices to consider and compute only the kernel $G(\hat{n}, \hat{n}')$, or its two independent real-valued components $g_{\pm}(\hat{n}, \hat{n}')$, which divides the input signal into E and B families.

Computation of E and B kernels

In theory, the E–B decomposition as introduced in section 1.3 was based on local differentiation. In practice, observational data has some finite resolution, and the computable E and B modes are band-limited versions of the differential concept. This is very naturally compatible with the formalism developed in this chapter: the sums $\sum_{\ell, m}$ should be understood to have some finite upper bound on ℓ . This dependence on ℓ_{\max} can be considered a property of the kernel itself, and if relevant the band-limited kernels can be denoted by $G_{E/B}^{\ell_{\max}}$. In [69], the possibility of a lower limit $\ell_{\min} > 2$ is also considered; again, this is naturally accommodated in the current formalism, although it is unused in this thesis and no notation is adopted. In the limit $\ell_{\max} \rightarrow \infty$, the series definitions of $G_i(\hat{n}, \hat{n}')$ are not generally expected to converge. The limits like

$$\lim_{\ell_{\max} \rightarrow \infty} \sum_{\ell=2}^{\ell_{\max}} \sum_{m=-\ell}^{\ell} {}_2Y_{\ell m}(\hat{n}) {}_{-2}Y_{\ell m}(\hat{n})$$

may not exist, but will turn into some combination of delta functions. When an upper bound on ℓ in the sums is adopted, the kernels are finite valued.

The central point is: the band-limited E–B decomposition is eminently non-local. The values of $\vec{P}_E(\hat{n})$ and $\vec{P}_B(\hat{n})$ at a particular point depend on the values of $\vec{P}(\hat{n})$ over the entire sky, or, in other words, the convolution kernels $G_{E/B}(\hat{n}, \hat{n}')$ are nonzero for almost all \hat{n} and \hat{n}' .

Otherwise, there is little difficulty in transitioning from the continuous to the pixelized case. The integrals in equations (2.22), (2.23), and (2.25) become Riemann sums; the sums in equation (2.24) should be evaluated up to at least the ℓ_{\max} that corresponds to the resolution afforded by the pixelization. If the data is band-limited or filtered itself, then the corresponding lower ℓ_{\max} for the kernels suffices. In general, if the kernels are evaluated to a higher ℓ than the ℓ_{\max} of the data, it makes no difference to the result, because of the orthogonality of the spherical harmonics with different ℓ . Therefore a pre-computed $G_{E/B}^{\ell_{\max}}$ kernel can be used on any data with multipole content up to ℓ_{\max} . The notion of

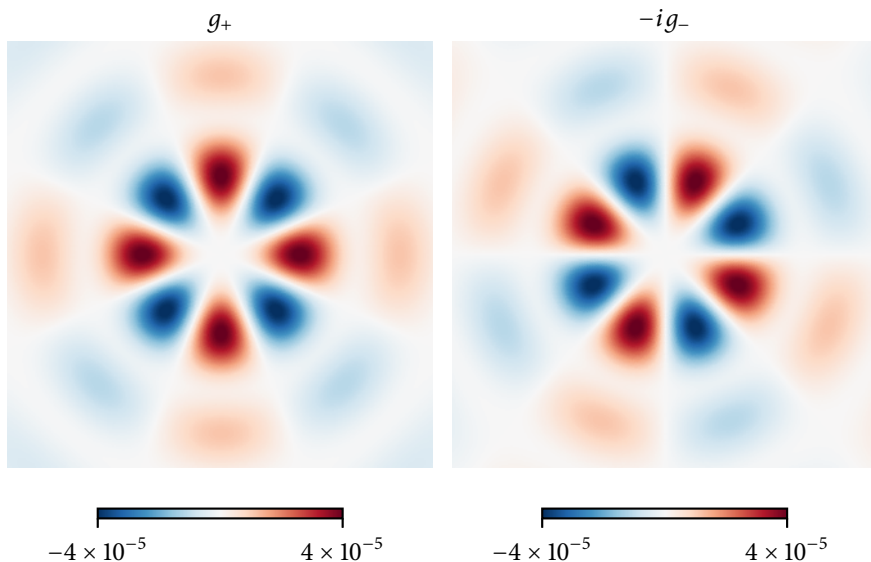


Figure 2.1: $g_+(\hat{n}, \hat{n}')$ and $-ig_-(\hat{n}, \hat{n}')$, plotted as functions of \hat{n} with \hat{n}' fixed at the center of the maps. The two components are related to each other by a 22.5° rotation around the central point.

“band-limited delta functions”, mentioned above, is also discussed at greater length in [69]. This is what happens to all $\delta(\hat{n} - \hat{n}') \rightarrow \delta^{\ell_{\max}}(\hat{n} - \hat{n}_0)$ in the pixelized case.

When a value of ℓ_{\max} has been adopted, there are several strategies possible for numerical computation of the E/B kernels. The sums in equation (2.24) can be computed directly using the definition of the spin-weighted spherical harmonics. However, depending on the implementation, this kind of calculation can be slow, and it is only feasible for low ℓ_{\max} . A faster approach is based on harmonic transformation of unit vector input maps. Harmonic transformation itself can be performed using healpy or other software packages like ssht [120].

Also, the real and imaginary parts of \mathcal{D} in [69] correspond to the two real-valued g_+ and g_- kernel components; the \mathcal{I} in [69] corresponds to the band-limited delta function, which behaves similarly in both formalisms.

Linear algebra notation

The convolution kernels, either $G(\hat{n}, \hat{n}')$ or $G_{E/B}(\hat{n}, \hat{n}')$, are functions $S^2 \times S^2 \rightarrow \mathbb{R}^{2 \times 2}$, i.e. they map any two points on the sphere to a real 2×2 matrix. The E and B families then follow from matrix multiplication and integration with the input signal $\vec{P}(\hat{n})$. Because matrix multiplication and integration are linear, the entire process can be represented by a linear operator which maps the input polarization signal to the E and B families. In the pixelized domain, this will be some mapping $\mathbb{R}^{N_{\text{pix}}} \times \mathbb{R}^{N_{\text{pix}}} \rightarrow \mathbb{R}^{N_{\text{pix}}} \times \mathbb{R}^{N_{\text{pix}}}$. It is convenient to imagine the Q and U values stacked upon each other, in which case the mapping is $\mathbb{R}^{2N_{\text{pix}}} \rightarrow \mathbb{R}^{2N_{\text{pix}}}$, which corresponds to a $2N_{\text{pix}} \times 2N_{\text{pix}}$ real-valued matrix. This matrix will have four sectors, as below for G_E :

$$\begin{pmatrix} Q_E(n_1) \\ \dots \\ Q_E(n_N) \\ U_E(n_1) \\ \dots \\ U_E(n_N) \end{pmatrix} = \begin{pmatrix} G_{QQ} \\ \\ \\ G_{UQ} \end{pmatrix} \begin{pmatrix} G_{QU} \\ \\ \\ G_{UU} \end{pmatrix} \begin{pmatrix} Q(n_1) \\ \dots \\ Q(n_N) \\ U(n_1) \\ \dots \\ U(n_N) \end{pmatrix}. \quad (2.40)$$

A linear operator algebra is therefore at hand. The pixelized polarization data $P \in \mathbb{R}^{2N_{\text{pix}}}$ is decomposed into E and B families by the action of linear operators G_E and G_B . These operators are accompanied by the band-limited delta function, denoted l , which behaves in most respects as an identity, and they still can be represented in terms of a common decomposition operator G as

$$G_E = \frac{1}{2}l + G; \quad (2.41a)$$

$$G_B = \frac{1}{2}l - G. \quad (2.41b)$$

The operators obey such identities as

$$G_E G_E = G_E; \quad (2.42a)$$

$$G_B G_B = G_B; \quad (2.42b)$$

$$G_E G_B = 0; \quad (2.42c)$$

$$G_E + G_B = l; \quad (2.42d)$$

$$Gl = lG = G. \quad (2.42e)$$

The objects in these equations can be understood as the actual $2N_{\text{pix}} \times 2N_{\text{pix}}$ matrices, which act on pixelized maps, or they can be understood abstractly as standing for integral operators in the original continuous theory. The fact that the E–B decomposition could be fashioned in this way follows simply from its linearity. However, now the matrices have explicit formulas, and the entire scheme can be implemented and computed.

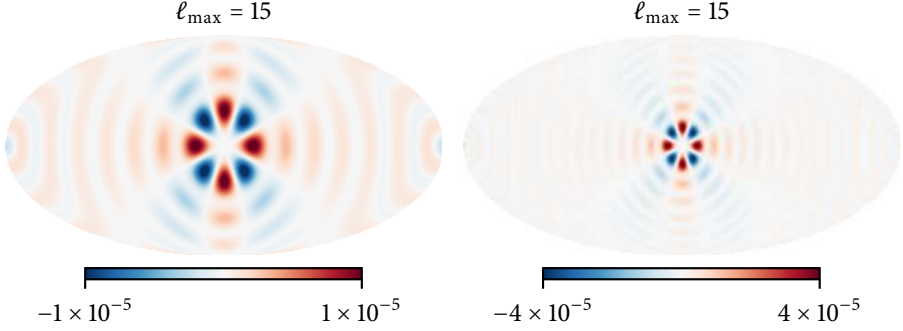


Figure 2.2: Full-sky plots of $g_+^{\ell_{\max}}(\hat{n}, \hat{n}')$ for two different values of ℓ_{\max} , plotted as a function of \hat{n} with \hat{n}' fixed in the center of the map.

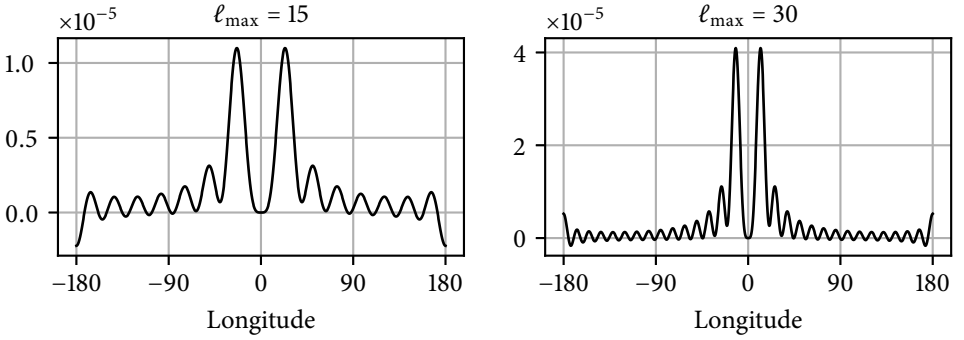


Figure 2.3: Cross sections of the kernels in figure 2.2 along the ring $b = 0^\circ$.

Visualization of kernels

In figure 2.2, $g_+(\hat{n}, \hat{n}_0)$ is shown for two different values of ℓ_{\max} . The basic structure is an 8-petal flower-like shape of alternating positive and negative contributions to the central point. Wave-like oscillations emanate from each petal and loop around the sky. Figure 2.3 shows a cross-section around the sphere along the equator. The kernel evaluates to exactly zero at the central point (all self-contribution is carried by the band-limited delta function part of the kernel). The two strongest peaks are on either side, surrounded by diminishing sidelobes. A subsidiary sole peak, exactly opposite to the central point, is also present. This peak can be either positive or negative depending on the value of ℓ_{\max} .

In figures 2.4 and 2.5, the maps and cross-sections of the band-limited delta functions are shown. This part of the kernel has spherical symmetry around the central point.

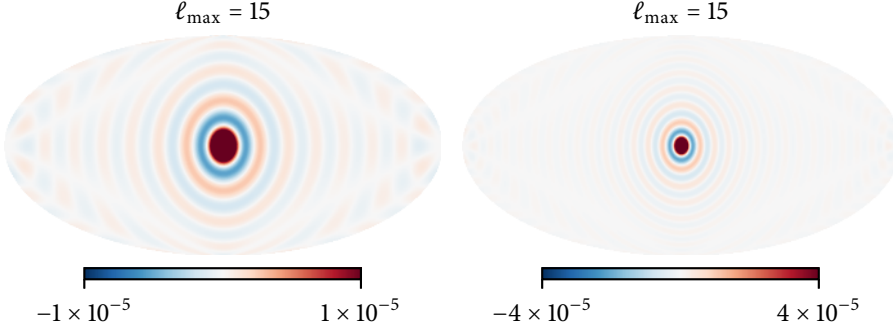


Figure 2.4: Full-sky plots of $\delta^{\ell_{\max}}(\hat{n} - \hat{n}')$ for two different values of ℓ_{\max} , plotted as a function of \hat{n} with \hat{n}' fixed in the center of the map.

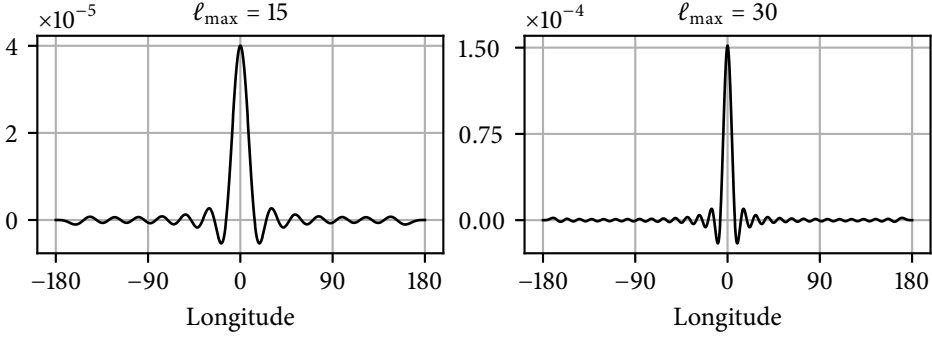


Figure 2.5: Cross sections of the kernels in figure 2.4 along the ring $b = 0^\circ$.

Oscillations with diminishing amplitude radiate in all directions around the sky, which converge to exactly zero at the antipodal point. In general, the $\delta^{\ell_{\max}}$ is more localized than $g_+^{\ell_{\max}}$ when both are evaluated at the same ℓ_{\max} . In the limit $\ell_{\max} \rightarrow \infty$, the normal delta function is approached.

g_+ and g_- are related by a 22.5° rotation around the central point. g_+ and g_- are illustrated side by side in figure 2.1.

Scalar E and B kernels

It is also possible to define the normal, scalar E and B modes in terms of a real space

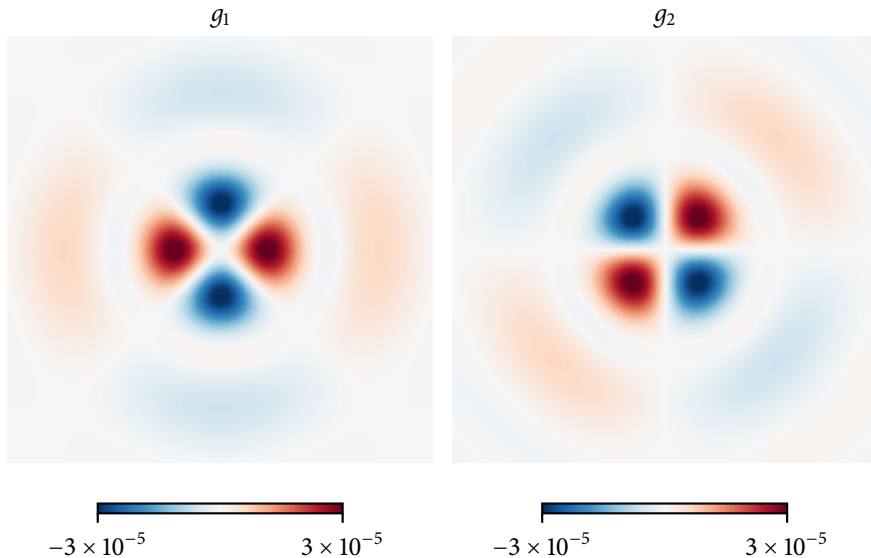


Figure 2.6: Convolution kernels for the normal scalar E and B modes. They are related by a rotation of 45° .

convolution. The corresponding kernels are real 1×2 matrices of the form $g_E = (g_1 \quad -g_2)$, and $g_B = (g_2 \quad g_1)$. These kernels are shown in figure 2.6.

These kernels, as they are defined here, have the same local shape on all points of the sky. The kernels of the E and B families will be slightly distorted at high latitudes, reflecting the dependence of Q and U on the coordinate system.

2.3 POLARIZATION ANALYSIS OF FOREGROUNDS

One advantage of the real space E–B decomposition is that it immediately introduces two pairs of new estimators: the polarization angles and polarization intensities associated with the E and B modes separately, defined in equation (2.16). In this section, these estimators are applied to the polarized dust foregrounds using the *Planck* frequency maps as tracers for polarized foregrounds.

Frequency maps above 100 GHz are dominated by thermal dust emission (see figure 1.4) [79, 121, 122]. The thermal dust emission is linearly polarized, potentially at a significant level, up to around 20% [77, 79, 87, 123]. The *Planck* 217 and 353 GHz maps are adopted here to trace thermal dust emission. These maps also contain relatively small signals from the CMB, the cosmic infrared background, and extra-Galactic point sources. The

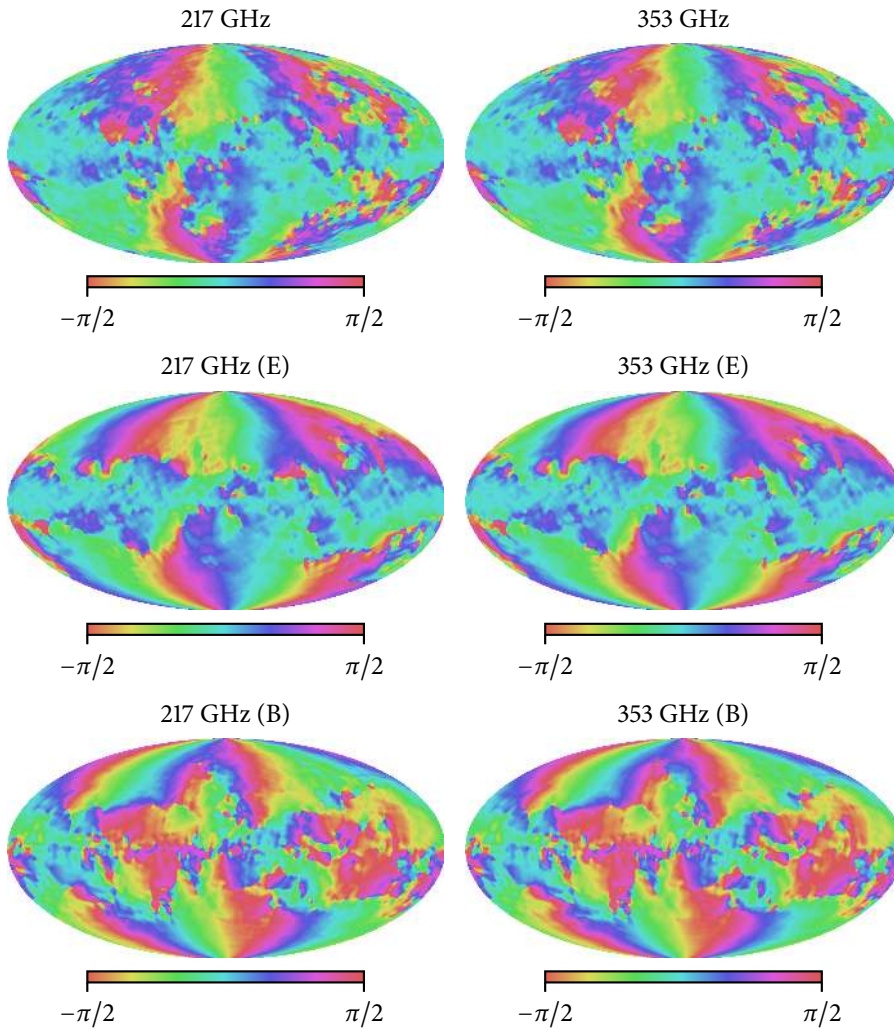


Figure 2.7: Polarization angles of the 217 GHz and 353 GHz frequency maps, originally (top row) and of the E and B modes separately (middle and lower rows).

possibility of separating these sources is discussed in [124].

Synchrotron radiation dominates at lower frequencies (see figure 1.4). Synchrotron radiation can also be significantly polarized, up to around 40% in localized filamentary structures associated with the Galactic magnetic field [125, 126]. In [16] the WMAP K and

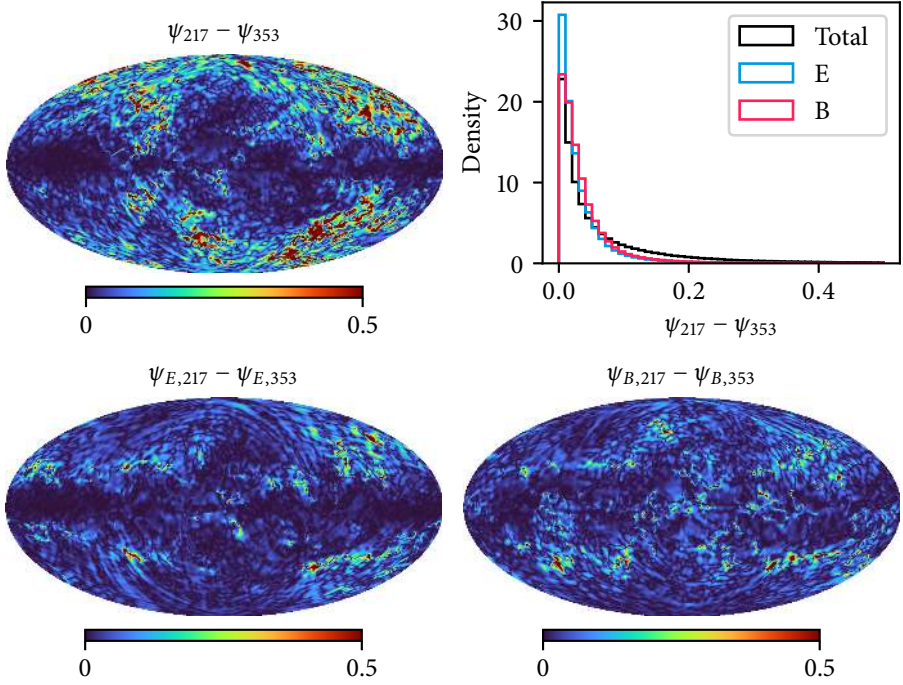


Figure 2.8: Difference of the 217 GHz and 353 GHz polarization angles before and after E/B separation. The difference is calculated using the always positive, absolute angular difference defined in equation (2.43). The same color scale is in use in all plots. The E polarization angles exhibits the greatest cross-frequency similarity.

Ka bands (22 GHz and 30 GHz) were chosen as low-intensity maps, intended to track synchrotron emission but bearing in mind the limited accuracy of this identification due to contamination by various other foregrounds and noise.

Polarization angles

The polarization angles ψ , ψ_E , and ψ_B from the 217 GHz and 353 GHz maps are shown in figure 2.7. The similarity between 217 GHz and 353 GHz is apparent, not only in the total maps but also in the E and B channels separately. To characterize the residuals between the two frequencies, the absolute angular difference is defined as

$$\psi_1 - \psi_2 \sim \Delta\psi = \left| \frac{1}{2} \arctan(\sin(2\psi_1 - 2\psi_2), \cos(2\psi_1 - 2\psi_2)) \right|. \quad (2.43)$$

	Total	E	B
Full sky	0.948	0.990	0.987
BICEP	0.970	0.998	0.996

Table 2.1: $C(\psi_{217}, \psi_{353})$ for the unseparated, E, and B angle maps, computed over the full sky or the BICEP zone.

Note that this formula has been adapted specifically for polarization angles, whose range is $[-\frac{\pi}{2}, \frac{\pi}{2}]$. However, the difference $\Delta\psi$ is defined absolutely without sign, and its range is $[0, \frac{\pi}{2}]$. The angular differences are plotted together with their distribution functions in figure 2.8. Individually, the E and B angles are similar to each other, deviating most strongly in mid-Galactic latitudes around $b = \pm 30^\circ$. The angles from the original unseparated maps show stronger deviations across the high-latitude sky, visible in the flattened distribution function.

Polarization angles in the BICEP zone

The observation area of the BICEP experiment [127, 128] is particularly interesting part of the sky. This sky zone was chosen because it is one of the cleanest patches of the sky that can be continuously scanned from the observatory location at the South Pole. However, it is not totally free of foreground contamination. Nevertheless, the region is interesting for foreground analysis because of the low amplitudes in this region; it also serves as a generic illustration of partial sky foreground analysis, within which the calculation of polarization angle differences is now repeated.

In figure 2.9, the angle differences are shown as in figure 2.8. Again, the E and B modes separately differ very little between the two frequencies. Much greater differences are found between the unseparated angles.

A measure of the similarity between two maps of polarization angles is given by the cross-correlation coefficient,

$$C(\psi_1, \psi_2) = \frac{1}{N} \sum_{i=1}^N \cos(2\psi_1(n_i) - 2\psi_2(n_i)), \quad (2.44)$$

where the sum is taken over all N pixels n_i . Note that again this formula is specific for polarization angle. Like the normal Pearson cross-correlation coefficient, $C(\psi_1, \psi_2)$ takes values between -1 and 1 . The correlations between ψ_{217} and ψ_{353} are shown in table 2.1.

In [16], the expected distribution of $C(\psi_1, \psi_2)$ was estimated in the case that the underlying signals are Gaussian noise, using the WMAP K and Ka bands with randomized phases. For Gaussian noise, the expectation of $C(\psi_1, \psi_2)$ is 0, and the standard deviation depends on the sky area and the smoothing angle. The analysis is not repeated here, but the results let us assert that the values in table 2.1 are inconsistent with a noise hypothesis

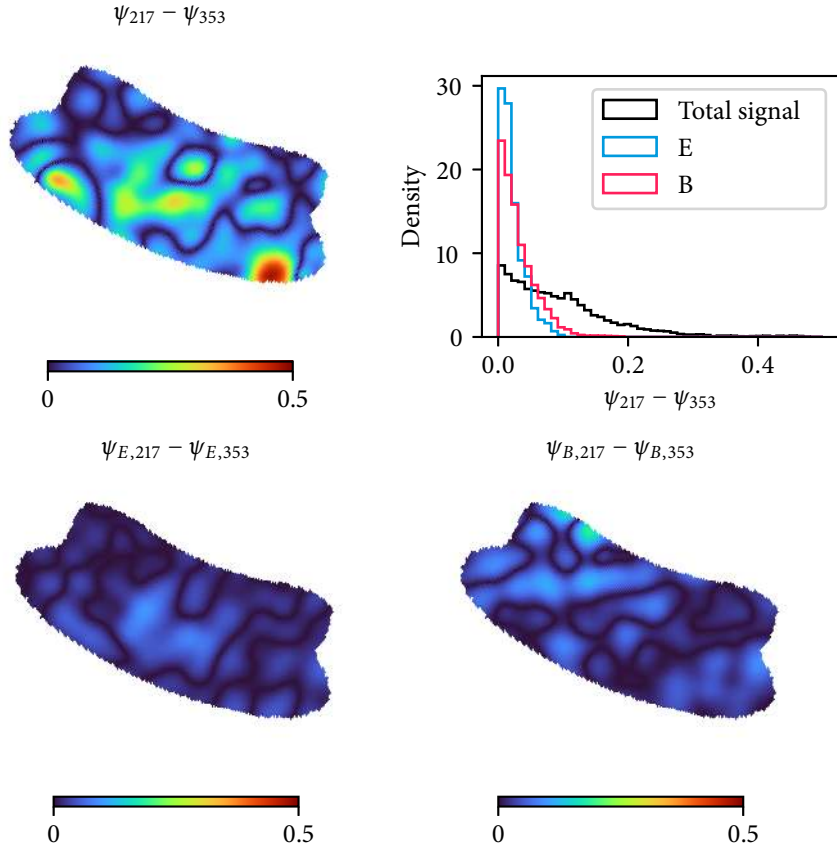


Figure 2.9: Difference of the 217 GHz and 353 GHz polarization angles before and after E–B separation, within the BICEP region. The E and B angles separately show greater consistency.

at high significance. The ψ_E and ψ_B estimators are therefore associated with intrinsic properties of the polarization signal.

Further, [16] also considered correlations between the WMAP K-band and the *Planck* 217/353 GHz maps. Significant correlations were found, sufficient to reject models in which ψ_E and ψ_B have no band-to-band correlation.

The polarization angles ψ , ψ_E , and ψ_B are related by

$$\tan(2\psi) = \frac{P_E \sin(2\psi_E) + P_B \sin(2\psi_B)}{P_E \cos(2\psi_E) + P_B \cos(2\psi_B)} \quad (2.45a)$$

$$= \frac{\rho \sin(2\psi_E) + \sin(2\psi_B)}{\rho \cos(2\psi_E) + \cos(2\psi_B)}, \quad (2.45b)$$

where $\rho = \frac{P_E}{P_B}$. If $\rho \gg 1$, then the total polarization signal is dominated by the E mode ($\vec{P} \approx \vec{P}_E$), which also carries over to the angles, for which asymptotically

$$\psi \approx \psi_E - \frac{1}{2\rho} \sin(2\psi_E - 2\psi_B). \quad (2.46)$$

This simple model is apparent in figure 2.7, although it does not necessarily hold everywhere on the sky. The North Polar Spur region was identified as having a particularly strong agreement between ψ and ψ_E [16]. To understand this, next the polarization intensities and the ratio ρ are examined directly.

Polarization intensities

The polarization intensities and the ratios are shown for the 217 and 353 GHz maps in figures 2.10 and 2.11. From these plots, it is visible that the E mode dominates ($\rho \gg 1$) in the Galactic plane as well as certain other regions at higher Galactic latitudes. Also, loop-like structures associated with the Galactic radio loops are visible in the E mode but not the B mode polarization intensities. An estimator which captures the morphological similarity between regions of E mode dominance and the overall strength of the polarization signal is

$$C(P, \rho) = \frac{\sum_i (P(n_i) - \langle P(n_i) \rangle)(\rho(n_i) - \langle \rho(n_i) \rangle)}{\sum_i (P(n_i) - \langle P(n_i) \rangle)^2 \sum_i (\rho(n_i) - \langle \rho(n_i) \rangle)^2}. \quad (2.47)$$

This correlation can be applied to regions of $\rho < 1$ and $\rho > 1$ separately. The meaning is the following. Where $\rho \gg 1$, the E mode is dominant, and a positive correlation is expected between ρ and P . Where $\rho < 1$, the B mode is stronger, and an anti-correlation between ρ and P is expected. Therefore a negative value of $C(P, \rho)|_{\rho < 1}$ constitutes detection of the B mode. See figure 2.12.

Frequency dependence

Following the analysis of the 217 GHz and 353 GHz frequency maps, next we consider the general frequency dependence of the E and B modes across the spectrum. The median value of $\rho = P_E/P_B$ is shown in figure 2.13 for all frequency bands from 30 GHz to 353 GHz. There is general convergence around $\rho \approx 1.4$ for the higher frequencies. Below 100

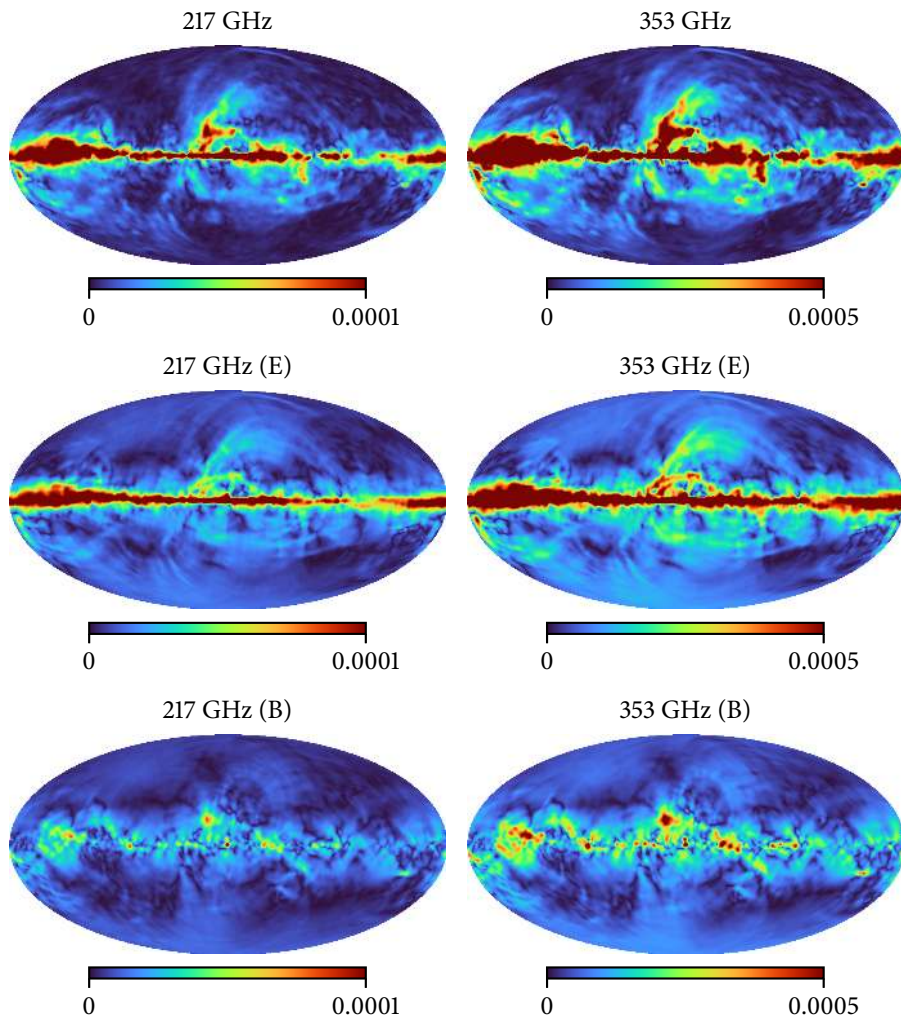


Figure 2.10: Polarization intensities (units = K). E family emission is tightly concentrated in the Galactic plane, unlike B family emission, which is more diffuse. The Galactic radio loops are easily visible in E but are absent in B.

GHz, the median ρ appears to have some anti-correlation with the frequency. The same pattern is more or less consistent in the WMAP bands [16].

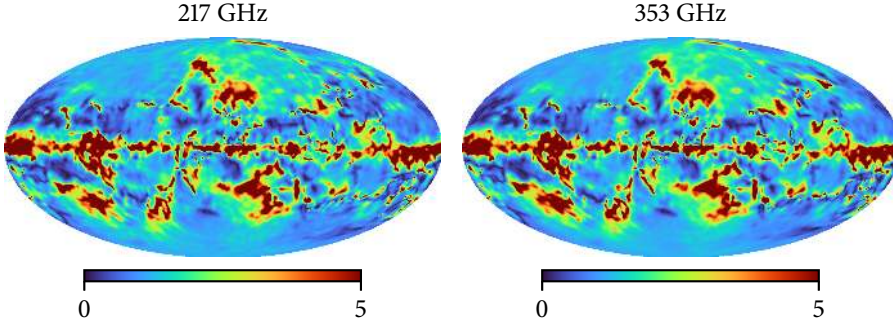


Figure 2.11: Ratio of E to B polarization intensities. Red regions, indicating the dominance of the E mode, are concentrated tightly along the Galactic plane, plus some other regions that can be associated with the Galactic radio loops.

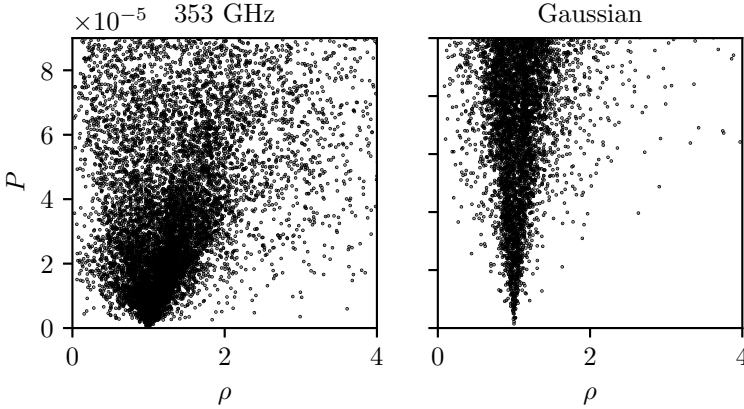


Figure 2.12: Scatter plots of P and ρ for the 353 GHz map and Gaussian noise. In the pure Gaussian case, the expected correlation is greater than observed in the foreground maps. The clustering on the right and left sides of the line $\rho = 1$ is an indicator of the E and B components of the foreground map respectively.

Spectral indices

Assuming a power law model, the spectral index can be estimated as¹

$$\beta(\hat{n}) = \frac{\log\left(\frac{P_1(\hat{n})}{P_2(\hat{n})}\right)}{\log\left(\frac{\nu_1}{\nu_2}\right)}, \quad (2.48)$$

¹See Appendix A of [16] for a note on this simplification.

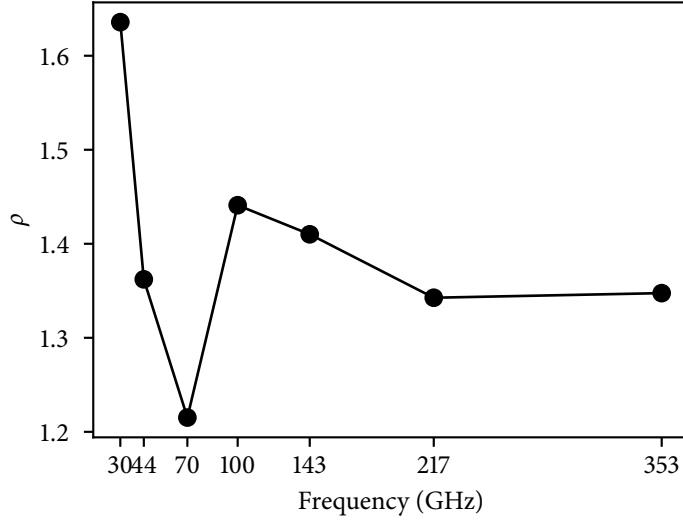


Figure 2.13: The median ρ for each of the *Planck* frequency bands up to 353 GHz. The 44 GHz and 70 GHz are the closest to E–B equality; other frequencies tend towards E dominance by around 30–50%.

where P_1 and P_2 are two sky maps with frequencies ν_1 and ν_2 . In this definition, the spectral index is defined independently at each \hat{n} , and therefore is allowed to vary across the sky. In figure 2.14, the distribution functions of this estimator are shown using the 217 and 353 GHz maps, for the total signal and the E and B modes separately. Thermal dust emission is expected to have a spectral index of 4, and the spectral indices are generally well clustered near this point, although there is a slight generic deficit. The spectral index of the E mode is more homogeneous than of the B mode, which is, in turn, more homogeneous than the total signal.

The same distribution functions are shown in the lower panel of figure 2.14 for the BICEP zone only. In this region, we see a slight tension between the E and B mode, with the E mode having a slightly higher spectral index than the B mode. Unsurprisingly, the distribution for the total signal takes a significantly greater variance.

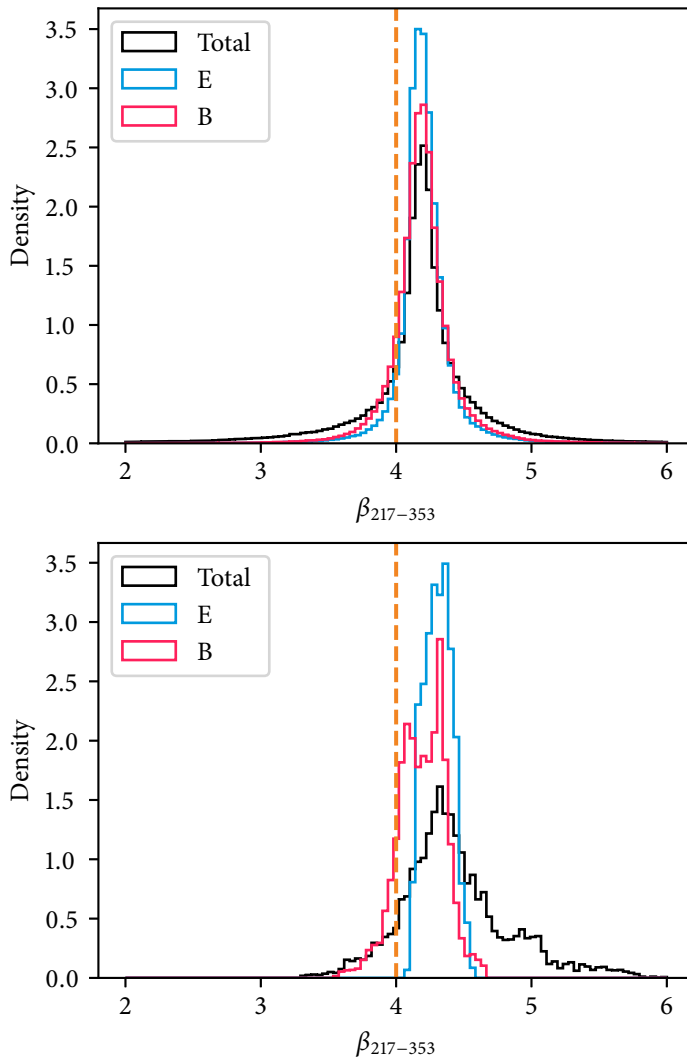


Figure 2.14: The upper panel shows the distribution of estimated spectral indices between 217 GHz and 353 GHz. The distribution is over the unmasked sky, and indicates the range of the spectral index. The lower panel shows the same using pixels from the BICEP zone only. The total polarization signal exhibits greater variation of the spectral index compared to the E and B components separately.

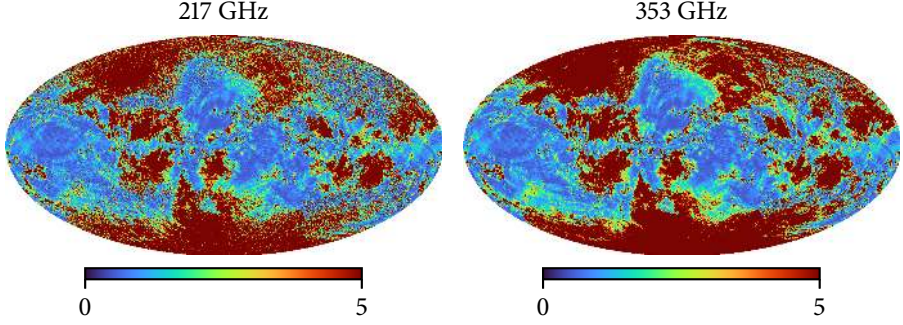


Figure 2.15: Γ parameter for 217 and 353 GHz maps. The E and B modes are correlated when $\Gamma < 1$, indicated by the blue zones, which dominate at lower Galactic latitudes.

E–B coupling

The final estimator introduced in this series of analyses is Γ :

$$\Gamma^2 = \frac{P_E^2 + P_B^2}{P^2} = \frac{1 + \rho^2}{1 + 2\rho \cos(2\psi_E - 2\psi_B) + \rho^2}. \quad (2.49)$$

The Γ parameter reflects the coupling between the E and B modes. Comparing Γ to 1 is comparing $P_E^2 + P_B^2$ to $|\vec{P}_E + \vec{P}_B|^2$; the difference is the cross-term proportional to $\vec{P}_E \cdot \vec{P}_B$. If the E and B modes are correlated, then $\Gamma < 1$. This can also be seen in the sign of $\cos(2\psi_E - 2\psi_B)$. Γ is plotted in figure 2.15. E–B correlation is concentrated in the Galactic plane; but the polar regions indicate E–B anticorrelation. The transition between the two regimes is, in most places, fairly sharp.

To conclude this section, the E–B family decomposition provides new tools for the analysis of the foreground polarization, particularly polarization orientations and intensities. The polarization angles of the E and B families in the 217 GHz and 353 GHz maps were shown to be fairly stable between frequencies. The patterns in these polarization angle maps should hopefully be sensitive to systematics and can be applied to small regions of the sky. The ratio of the polarization intensities, denoted ρ , reveals E dominance over B in the Galactic plane and certain other regions on the sky.

The spectral index of the thermal dust emission shows that its variance differs in the E and B families compared to the total signal, especially in the BICEP zone, where the E spectral index especially has a small variance. This has implications for foreground removal: in some sense, the greater variance of the spectral index will behave like increased noise in

the algorithms. In general, it is seen that the mixture of E and B in the total unseparated signal results in greater variance of the estimators, reflecting some coherence in the E and B emission at these frequencies.

A general consideration that applies to the results in this chapter, and to all map-domain analyses, is the smoothing angle. Here the Q and U data were subject to smoothing at 2.5° before computation of the polarization angles and polarization intensities, except in figures 2.14 and 2.15, where 0.5° was used.

3 E–B LEAKAGE

The E–B decomposition is originally conceived in a full-sky setting, but realistic CMB data sets do not have full-sky coverage, due to residual contamination from the Galactic plane and other foregrounds which must be masked, and possibly also because of the scanning limitations of ground-based telescopes. The original E and B modes are not unique nor well-defined on the partial sky. E–B *leakage* refers to the tendency of the true E mode to “leak” power into the apparent partial-sky B mode, ruining its most desirable property.

Early attempts to overcome this obstacle sought to define modified versions of the E and B modes conforming to the specific shape of the available sky [129, 130]. Such methods are not unlike the methods used for estimation of the power spectrum of the temperature anisotropy from partial sky data [131, 132], which entail e.g. orthogonalization of the spherical harmonics and result in pseudo- C_ℓ estimators. The main result of these efforts [72, 73, 119, 130, 133] is, roughly speaking, a tripartite decomposition of the partial-sky polarization signal into *pure* E and B modes and an *ambiguous* mode, which represents a part of the signal that cannot be assigned to either. The pure E and B modes are unique and well-defined: but there is no expectation that they should be equal to the *true* E and B modes, which would be calculated if full-sky data were available. They are still useful estimators insofar as the pure B mode is sensitive to cosmological signals, and some methods exist to estimate the true E and B modes from the pure E and B modes.

A crucial point is that the target of these methods, and others that have been discussed and used in the literature (e.g. [134–136]), is generally the pseudo- C_ℓ power spectrum estimate, rather than the pixel-domain B mode map itself. Pure E and B mode maps are, however, constructed in [119], as discussed below in section 4.1.

In this chapter, the E–B leakage problem is reexamined, drawing heavily on the new understanding of the E–B decomposition provided by the convolution kernel analysis in the previous chapter. The main goal is to correct leakage in the pixel domain and produce a corrected B mode *map*. Also, we avoid redefinition of the E and B modes. The target is the *true* E and B modes as they were originally defined on the full sky: which, although unknowable, can still be studied to understand how the apparent E and B modes differ from the true E and B modes, and how this difference can be reduced. This work has been published in a series of papers [17, 19, 137], and there is some overlap with chapter 5 in [138].

There are many potential advantages of leakage correction in the pixel domain. They are discussed in [17, 19, 137, 138]. It is also useful to know where the leakage is coming from, especially in the study of foregrounds and their possible contamination. The E–B convolution kernels enable this to be investigated closely and carefully.

Although E–B leakage occurs whenever part of the sky is masked, the upcoming ground-based CMB experiments that are constrained to observe a part of the sky are especially susceptible. Accurate reconstruction of the B mode from partial sky data is an important component of the data analysis pipelines in order to enable measurements of r at the 10^{-3} level or below.

Terminology and notation

Some conventions in terminology are adopted for this chapter. A subset of the sphere, $\Omega \subset S^2$, is observed. The boundary of Ω is denoted by $\partial\Omega$. Ω will be called the “observed region” or “region 1”, and this region will be indicated by an ordinal 1 in equations or integrals. The complement of Ω is the unobserved region, from which data is missing, sometimes called “region 2”, and appearing as a subscript 2 in integrals. These two regions of the sky are characterized by a mask $M(\hat{n})$, defined as

$$M(\hat{n}) = \begin{cases} 1, & \hat{n} \in 1; \\ 0, & \hat{n} \in 2. \end{cases} \quad (3.1)$$

It is not assumed that Ω is simply connected. $M(\hat{n})$ can be a realistic confidence mask that masks the Galactic plane together with other high-latitude point sources. However, most of the examples in this chapter use very simple spherical and rectangular masks, to illustrate the principles of leakage and its correction.

A “fiducial” (leakage-corrupted) E–B decomposition is taken over region 1 by setting $\vec{P} = 0$ in the entirety of region 2, and then treating this as a full-sky map. The normal definitions and methods of E–B decomposition can be applied as before, in other words, taking the E–B decomposition of the map $M(\hat{n}) \times \vec{P}(\hat{n})$. The fiducial E and B modes resulting from this decomposition will be denoted with primes, by \vec{P}'_E and \vec{P}'_B .

3.1 DIFFUSIVE INPAINTING

In [119], the leakage question is framed in terms of an *ambiguous mode* with potential $\Psi(\hat{n})$, which satisfies the spherical biharmonic equation on the observed sky:

$$\nabla^2(\nabla^2 + 2)\Psi(\hat{n}) = 0. \quad (3.2)$$

It can be shown that this equation implies that the ambiguous mode satisfies $D_B^\dagger D_E \Psi = D_E^\dagger D_B \Psi = 0$, and so it could be attributed to either the E or B mode or some combination

thereof. Beginning with some arbitrary fiducial decomposition (affected by leakage),

$$\vec{P}' = \vec{P}'_E + \vec{P}'_B = D_E \Psi'_E + D_B \Psi'_B, \quad (3.3)$$

[119] solves equation (3.2) twice with boundary conditions given by the fiducial E/B potentials Ψ'_X , $X \in \{E, B\}$. The full boundary value problem is:

$$\nabla^2(\nabla^2 + 2)\alpha_X = 0; \quad (3.4a)$$

$$\alpha_X|_{\partial\Omega} = \Psi'_X|_{\partial\Omega}; \quad (3.4b)$$

$$\hat{n} \cdot \nabla \alpha_X|_{\partial\Omega} = \hat{n} \cdot \nabla \Psi'_X|_{\partial\Omega}. \quad (3.4c)$$

Then, purified potentials are defined

$$\Psi_E = \Psi'_E - \alpha_E; \quad (3.5a)$$

$$\Psi_B = \Psi'_B - \alpha_B. \quad (3.5b)$$

Differentiation as follows yields pure E mode, pure B mode, and ambiguous mode fields:

$$\vec{P}_{pE} = D_E \Psi_E; \quad (3.6a)$$

$$\vec{P}_{pB} = D_B \Psi_B; \quad (3.6b)$$

$$\vec{P}_a = D_E \alpha_E + D_B \alpha_B. \quad (3.6c)$$

Solving equation (3.2) is challenging computationally, especially if the region and the boundary conditions are irregular, but a successful implementation (within a flat-sky approximation) is described in [119].

In [17], a simplification of Bunn's method is presented, termed *method 1* in that paper (*method 2* of [17], which is the main part of the work, follows below in sections 4.2 and 4.3). There are two principles of the simplification that lead to *method 1*. First, the bi-Laplacian is replaced by the Laplacian, which is mathematically simpler, and the Laplacian problem has trivial and rapid numerical solutions using relaxation methods. The solutions of the Laplacian problem are expected to retain the basic structure of the true bi-Laplacian solutions, especially on large angular scales, although they will differ on smaller scales. Furthermore, equation (3.4c) is discarded. The Laplacian equation is overspecified by both Neumann and Dirichlet boundary conditions.

Also, in [17], the entire procedure is transferred to the B mode itself, rather than the potential. The normal B mode (defined in equation (1.24)) is closely related to the potential Ψ_B , and it makes little difference which is used. In fact, the method can work similarly on each Stokes parameter map, $Q_B(\hat{n})$ and $U_B(\hat{n})$, as well. The theoretical justification behind these simplifications and modifications of the method is weak: the proof of the method is its performance on simulations, which is impressive.

In summary, the Laplacian equation is solved once, using the corrupted B mode as the boundary condition. Then, the true B mode can be approximated from the measured B mode by subtraction of Laplacian solution.

It may seem irredeemable to discard Bunn’s *exact* method and replace it with this theoretically unsubstantiated method. But, it is emphasized that the “pure” B mode which results from Bunn’s method, however exactly it is defined, is not equal to the real B mode. Therefore approximation is inevitable, and both methods depend on empirical validation of their usefulness.

It is also possible to surmise some properties of the simplification of the method in more concrete terms. Any harmonic function α , which satisfies $\nabla^2 \alpha = 0$ in the interior of the region, is also biharmonic, satisfying $\nabla^2(\nabla^2 + 2)\alpha = 0$. The difference between the original and the simplified solutions is a function that is biharmonic but not harmonic. In a one-dimensional analogy of the problem, where the solutions would be polynomials, the difference would be composed of quadratic and cubic terms only and therefore associated with small-scale oscillations around the linear harmonic solution. The same principle applies to the two-dimensional case, although many more kinds of features are possible in two-dimensional biharmonic functions. The difference is zero on the boundary and satisfies the original Neumann boundary conditions, which seed the oscillations in the interior.

The implementation of method 1 uses relaxation to solve Laplace’s equation, subject to the boundary condition of the corrupted B mode at the edge of the mask; the loop will look like

$$B(\hat{n}) \leftarrow \frac{1}{4} \sum B(\hat{n} + d\hat{n}) \quad \text{for all interior pixels } \hat{n}, \quad (3.7)$$

where the sum is taken over all adjacent pixels. The boundary condition is reimposed after each iteration. As mentioned above, B can be the standard scalar B mode, the B mode potential, or Q_B or U_B . This type of computation is called *diffusive inpainting* because the boundary condition is diffused into the interior of the solution region. The convergence rate will depend on the resolution, but in general it is quite fast. Different convergence criteria are usable. Apart from the initial fiducial E–B decomposition, the entire method works in the pixel domain, and the output is a template that can be subtracted from the corrupted B mode to produce an estimate of the true B mode map.

3.2 REAL SPACE LEAKAGE MODEL

The premise is to approach the question of leakage within the real space decomposition formalism, summarized in equation (2.25), which is repeated here:

$$\tilde{P}_E(\hat{n}) = \int G_E(\hat{n}, \hat{n}') \tilde{P}(\hat{n}') d\hat{n}', \quad (3.8a)$$

$$\tilde{P}_B(\hat{n}) = \int G_B(\hat{n}, \hat{n}') \tilde{P}(\hat{n}') d\hat{n}'. \quad (3.8b)$$

There are different approaches to characterizing leakage in real space. The first is based on the notation of *contributors* introduced in [17]. This leads to the leakage equation giving the leakage as integration over region 2, which is visualized.

Contributors

To describe the polarization data in regions 1 and 2 separately, the following notation is introduced:

$$\vec{P}_{E_1}(\hat{n}) = \begin{cases} \vec{P}_E(\hat{n}) & \hat{n} \in 1 \\ 0 & \hat{n} \in 2 \end{cases} \quad \vec{P}_{B_1}(\hat{n}) = \begin{cases} \vec{P}_B(\hat{n}) & \hat{n} \in 1 \\ 0 & \hat{n} \in 2 \end{cases} \quad (3.9a)$$

$$\vec{P}_{E_2}(\hat{n}) = \begin{cases} 0 & \hat{n} \in 1 \\ \vec{P}_E(\hat{n}) & \hat{n} \in 2 \end{cases} \quad \vec{P}_{B_2}(\hat{n}) = \begin{cases} 0 & \hat{n} \in 1 \\ \vec{P}_B(\hat{n}) & \hat{n} \in 2 \end{cases} \quad (3.9b)$$

In [17], the notation is sometimes simplified like $\vec{P}_{E_1} = E_1$, etc. These four functions are all full-sky maps defined at every point, but with the value of 0 outside their respective regions. Therefore, for all \hat{n} , we have $\vec{P}_{E_1}(\hat{n}) + \vec{P}_{E_2}(\hat{n}) = \vec{P}_E(\hat{n})$ and $\vec{P}_{B_1}(\hat{n}) + \vec{P}_{B_2}(\hat{n}) = \vec{P}_B(\hat{n})$. In total,

$$\vec{P}_{E_1}(\hat{n}) + \vec{P}_{E_2}(\hat{n}) + \vec{P}_{B_1}(\hat{n}) + \vec{P}_{B_2}(\hat{n}) = \vec{P}(\hat{n}). \quad (3.10)$$

The calculation of \vec{P}_E and \vec{P}_B entails full-sky integration of \vec{P} with a suitable kernel, as in equation (3.8). Substituting equation (3.10) into equation (3.8) gives rise to equations like

$$\vec{P}_{E_1} = M(\hat{n}) \times \int G_E(\hat{n}, \hat{n}') (\vec{P}_{E_1}(\hat{n}') + \vec{P}_{E_2}(\hat{n}') + \vec{P}_{B_1}(\hat{n}') + \vec{P}_{B_2}(\hat{n}')) d\hat{n}'. \quad (3.11)$$

Similar equations for the other quantities are possible, with different permutations of G_E with G_B and $M(\hat{n})$ with $1 - M(\hat{n})$. These equations are tautological, but they illustrate how each of the four *output* quantities (the E or B families in region 1 or 2) in some sense depends, through the real-space convolution, on the *input* of the same four quantities, but unseparated between E and B. In [17], these contributions are denoted with the arrow notation, in which equation (3.11) would be written

$$\vec{P}_{E_1} = (E_1 \rightarrow E_1) + (E_2 \rightarrow E_1) + (B_1 \rightarrow E_1) + (B_2 \rightarrow E_1). \quad (3.12)$$

Explicitly, these four contributions are found by separating the integral in equation (3.10): for example,

$$(E_1 \rightarrow E_1) = M(\hat{n}) \times \int G_E(\hat{n}, \hat{n}') \vec{P}_{E_1}(\hat{n}') d\hat{n}', \quad (3.13)$$

and, in general,

$$(X_i \rightarrow Y_j) = \int G_Y(\hat{n}, \hat{n}') \vec{P}_{X_i}(\hat{n}') d\hat{n}' \times \begin{cases} M(\hat{n}), & \text{if } j = 1; \\ 1 - M(\hat{n}), & \text{if } j = 2; \end{cases} \quad (3.14a)$$

$$= \int_i G_Y(\hat{n}, \hat{n}') \vec{P}_X(\hat{n}') d\hat{n}' \times \begin{cases} M(\hat{n}), & \text{if } j = 1; \\ 1 - M(\hat{n}), & \text{if } j = 2. \end{cases} \quad (3.14b)$$

In equation (3.14b), the full-sky integration has been replaced by integration over the region in which the integrand is nonzero. However, the outcome of this integral is generically nonzero for all \hat{n} , before it is multiplied by either $M(\hat{n})$ or $1 - M(\hat{n})$.

The contributors satisfy an orthogonality identity, which easily follows from the integral definitions:

$$(X_1 \rightarrow Y_i) + (X_2 \rightarrow Y_i) = 0. \quad (3.15)$$

This is the statement that an E–B decomposition on a full-sky E mode will yield no B mode, and vice versa.

This notation and formalism make salient the subtle distinction between “E-to-B” leakage and “B-to-B” leakage. When only data from region 1 is available, the calculated E and B modes are missing two contributors. Particularly, the corrupted B family (restricted to region 1) is

$$\vec{P}'_{B_1} = (E_1 \rightarrow B_1) + (B_1 \rightarrow B_1). \quad (3.16)$$

The first term is the “E-to-B” leakage. In a full-sky E–B decomposition, this term is canceled by $(E_2 \rightarrow B_1)$; but in the fiducial partial sky E–B decomposition, it remains, corrupting the B mode. The second term is the B-to-B deformation, which differs from the true \vec{P}_{B_1} by the term $(B_2 \rightarrow B_1)$: this effect is called “B-to-B” leakage.

Integral representation and visualization

Now we return to the true E and B modes, expressed as full-sky integrals using (3.8). For emphasis, the integration domain is explicitly denoted f.s. here, standing for “full sky”:

$$\vec{P}_E(\hat{n}) = \int_{\text{f.s.}} G_E(\hat{n}, \hat{n}') \vec{P}(\hat{n}') d\hat{n}', \quad (3.17a)$$

$$\vec{P}_B(\hat{n}) = \int_{\text{f.s.}} G_B(\hat{n}, \hat{n}') \vec{P}(\hat{n}') d\hat{n}'. \quad (3.17b)$$

If only part of the sky is observed, it is possible to nevertheless attempt an E–B decomposition using the available data. Then the fiducial E and B modes can be written either as integrals over region 1, or as full-sky integrals with $M(\hat{n})$ moved into the integrand:

$$\vec{P}'_E(\hat{n}) = \int_1 G_E(\hat{n}, \hat{n}') \vec{P}(\hat{n}') d\hat{n}' = \int_{\text{f.s.}} G_E(\hat{n}, \hat{n}') M(\hat{n}') \vec{P}(\hat{n}') d\hat{n}', \quad (3.18a)$$

$$\vec{P}'_B(\hat{n}) = \int_1 G_B(\hat{n}, \hat{n}') \vec{P}(\hat{n}') d\hat{n}' = \int_{\text{f.s.}} G_B(\hat{n}, \hat{n}') M(\hat{n}') \vec{P}(\hat{n}') d\hat{n}'. \quad (3.18b)$$

Like any E–B decomposition performed in this way, even with some zones of the sky zeroed, the fiducial E and B modes still add up exactly to the input, however, in the partial sky case, the input is 0 outside the observed region. Formally, this can be denoted

$$\vec{P}'_E(\hat{n}) + \vec{P}'_B(\hat{n}) = M(\hat{n}) P(\hat{n}); \quad (3.19)$$

which reduces to equation (2.1) for all observed \hat{n} . However, although the fiducial E and B modes behave like the true E and B modes in this respect, there is no guarantee that they should be equal, and in general they will not be. The difference between \vec{P}'_B and \vec{P}_B is what is called the total leakage, which is a real-space function of \hat{n} . Through equation (3.19), \vec{P}'_E is also subject to leakage. The two leakage terms are denoted \vec{L}_E and \vec{L}_B :

$$\vec{P}'_E(\hat{n}) = \vec{P}_E(\hat{n}) - \vec{L}_E(\hat{n}), \quad (3.20a)$$

$$\vec{P}'_B(\hat{n}) = \vec{P}_B(\hat{n}) - \vec{L}_B(\hat{n}). \quad (3.20b)$$

Now, in this framework, the leakage has an explicit integral representation, but it must be handled carefully in the case of $\hat{n} \in 2$. Equation (3.20) makes sense when $\hat{n} \in 1$. The case of $\hat{n} \in 2$ is more subtle. When $\hat{n} \in 2$, the fiducial E and B modes are by no means equal to 0; however, they satisfy the constraint

$$\vec{P}'_E(\hat{n}) + \vec{P}'_B(\hat{n}) = 0. \quad (3.21)$$

The leakage is the E or B decomposition of the missing data only, so it can be written as an integration over region 2. The explicit leakage integrals are

$$\vec{L}_E(\hat{n}) = \int_2 G_E(\hat{n}, \hat{n}') \vec{P}(\hat{n}') d\hat{n}' \quad (3.22a)$$

$$\vec{L}_B(\hat{n}) = \int_2 G_B(\hat{n}, \hat{n}') \vec{P}(\hat{n}') d\hat{n}'. \quad (3.22b)$$

Therefore

$$\vec{L}_E(\hat{n}) + \vec{L}_B(\hat{n}) = \int_2 (G_E(\hat{n}, \hat{n}') + G_B(\hat{n}, \hat{n}')) \vec{P}(\hat{n}') d\hat{n}' \quad (3.23a)$$

$$= \int_2 \delta(\hat{n} - \hat{n}') \vec{P}(\hat{n}') d\hat{n}' \quad (3.23b)$$

$$= \begin{cases} 0, & \hat{n} \in 1; \\ \vec{P}(\hat{n}), & \hat{n} \in 2. \end{cases} \quad (3.23c)$$

Within the observed region, then,

$$\vec{L}_E(\hat{n}) = -\vec{L}_B(\hat{n}) \equiv \vec{L}(\hat{n}) \quad (\hat{n} \in 1). \quad (3.24)$$

Similarly to before, integrals over region 2 can be converted to integration over the full sky by introducing a factor $1 - M(\hat{n}')$ into the integrand:

$$\vec{L}(\hat{n}) = - \int_{\text{f.s.}} G_B(n, n') (1 - M(\hat{n}')) \vec{P}(\hat{n}') d\hat{n}' \quad (\hat{n} \in 1) \quad (3.25a)$$

$$= \int_{\text{f.s.}} G_E(n, n') (1 - M(\hat{n}')) \vec{P}(\hat{n}') d\hat{n}'. \quad (\hat{n} \in 1) \quad (3.25b)$$

Therefore a leakage kernel can be defined as

$$G_L(\hat{n}, \hat{n}') = -G_B(\hat{n}, \hat{n}')(1 - M(\hat{n}')) = G_E(\hat{n}, \hat{n}')(1 - M(\hat{n}')). \quad (\hat{n} \in 1) \quad (3.26)$$

These equations show the emergence of symmetry between E and B, in which the leakage can be written either as a sort of E mode (equation (3.25a)) or a sort of B mode (equation (3.25b)). The leakage convolution kernel, too, is related symmetrically to the E and B kernels, up to a minus sign. There is an analogy with the ambiguous mode, satisfying both $D_E\Psi = 0$ and $D_B\Psi = 0$ in Bunn's formalism

Recall equation (2.35), repeated here:

$$G_E(\hat{n}, \hat{n}') = \frac{1}{2}\delta(\hat{n} - \hat{n}') + G(\hat{n}, \hat{n}'); \quad (3.27a)$$

$$G_B(\hat{n}, \hat{n}') = \frac{1}{2}\delta(\hat{n} - \hat{n}') - G(\hat{n}, \hat{n}'). \quad (3.27b)$$

The leakage kernel can therefore be written as

$$G_L(\hat{n}, \hat{n}') = G(\hat{n}, \hat{n}')(1 - M(\hat{n}')), \quad (\hat{n} \in 1) \quad (3.28)$$

which follows because

$$\frac{1}{2}\delta(\hat{n} - \hat{n}')(1 - M(\hat{n}')) = 0. \quad (\hat{n} \in 1) \quad (3.29)$$

The \pm asymmetry between E and B in equation (3.27) nicely balances the \pm between the two expressions for G_L . As before, it is the single kernel $G(\hat{n}, \hat{n}')$ which underlies the mathematics of both the E–B decomposition and E–B leakage. It is a virtue of the real space E–B model that all is reduced to this one simple object.

The leakage kernel is determined by the mask. Figure 3.1 shows a plot of the leakage kernel of a circular mask. Note that all the considerations about resolution and ℓ_{\max} , discussed in the previous chapter for the E and B kernels, also apply to the leakage kernel.

In [139], it was observed that the leakage is concentrated near the edge of the mask, and negligible in regions distant from the masked sky. This observation is now fully explainable in terms of the leakage kernels. We can expect that leakage will be especially concentrated in corners, or regions where the mask is narrow.

An important remark is that the leakage kernel defined here applies to the E and B families in the space of Q, U . The traditional scalar E and B modes, which were studied in [139], are associated with slightly different kernels as discussed in the previous chapter. In particular, the dependence on latitude is different between the two types of kernels. Nevertheless, they have the same localization properties and the same near-circular arrangement of “petals”.

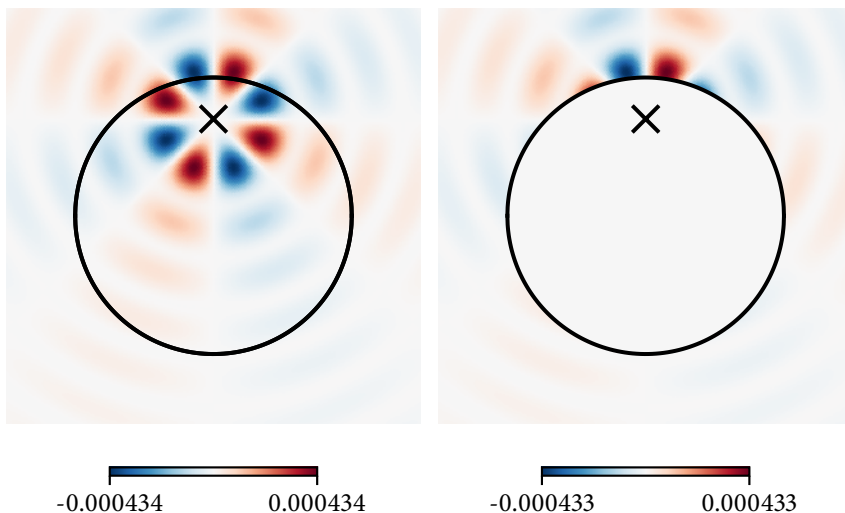


Figure 3.1: The left panel shows $G(\hat{n}, \hat{n}')$ as a function of \hat{n}' , with \hat{n} fixed at the black cross. The right panel shows $G_L(\hat{n}, \hat{n}')$ in the same way, when the mask is the circular disk shown on both plots. Given some mask, $G_L(\hat{n}, \hat{n}')$ is $G(\hat{n}, \hat{n}')$ with the *inverse* mask applied over \hat{n}' (see equation (3.28)).

Linear algebra notation

At the end of section 2.2, a notation for E–B decomposition based on linear operators was introduced. It should now be extended by adding the mask operator M , which is a diagonal matrix with diagonal entries either 0 or 1 depending on whether the corresponding pixel is masked or unmasked. The mask operator is idempotent, $MM = M$. The leakage operator is

$$L_M = -G_B(I - M). \quad (3.30)$$

These operators are generally non-commutative; in fact, the leakage within region 1 can be expressed neatly as a commutator, $[M, G]P$.

3.3 RECYCLING METHOD

The feasibility of correcting leakage

Figure 3.1, though lying atop a significant effort to make a mathematical analysis and framework of E–B leakage, is very simple, and at first appearance, seems hopeless: the leakage term is convolution with missing data alone. The leakage kernel includes no

contribution from the observed region. If it did, this part of the leakage could be easily calculated and subtracted; but as it stands, it seems all available information has been used.

However, it is possible to proceed. First, it will be argued that correction is feasible; then, the thematic derivation of the recycling method (method 2 of [17]) will be made.

The feasibility of correcting E–B leakage, and in some sense reaching into the masked sky, is based on the fact that the map is continuous. Interesting CMB maps are not white noise, but they have a non-flat power spectrum; they are further smoothed (at high ℓ) by Silk damping, the telescope beam pattern, and possibly further deliberate data processing. Therefore they are continuous in the pixel domain. The values of Q and U near the edge, but inside, of the observed region inform us about the values of Q and U outside of the observed region, near the edge. This knowledge is then translated into knowledge about leakage through the leakage kernel, which is exactly known anywhere on the sky. In figure 3.1, one could imagine, as a very crude implementation of this idea, reflecting the observed Q and U over the boundary of the mask, multiplying by the leakage kernel, and *subtracting* this from the fiducial B mode.¹ The further away from the edge of the mask, the less informative continuity is. But, at the same time, the contribution to the leakage also diminishes further away from the edge. Similarly, on smaller angular scales, the continuity is less useful, but the leakage is also more localized on smaller angular scales.

The information provided by the shape of the mask and the continuity of the map is probabilistic. Multiple different methods can be designed to exploit this information. The method below, called the recycling method, works by repeating an E–B decomposition on the corrupted E mode, in which the leakage can be calculated exactly because the input B mode of the second decomposition is known to be 0. The method relies on the dominance of the E mode over the B mode to approximate the

Recycling method

Consider the corrupted E family \vec{P}'_E resulting from a fiducial decomposition, which has the generic decomposition $\vec{P}'_E = \vec{P}'_{E_1} + \vec{P}'_{E_2}$, and neither \vec{P}'_{E_1} nor \vec{P}'_{E_2} is expected to be zero. The idea is to perform a second E–B decomposition starting from the corrupted E family *in region 1 only*. When the E mode dominates the B mode, this second decomposition resembles the first, and it is hoped that it produces a similar leakage term; but, because there was no input B mode in the second decomposition, the resulting B mode consists only of the leakage contribution.

The linear algebra notation is convenient here. Let P denote the full-sky, unknown polarization data. Only MP is known. The fiducial E and B modes are $G_E MP$ and $G_B MP$;

¹This strategy would resemble the principle of the diffusive inpainting method.

they are related to the true E and B modes by leakage:

$$G_E MP = G_E P - L_M P; \quad (3.31a)$$

$$G_B MP = G_B P + L_M P. \quad (3.31b)$$

The E–B decomposition of the fiducial E mode in region 1 is

$$MG_E MP = G_E MG_E MP + G_B MG_E MP. \quad (3.32)$$

These E and B modes are subject to leakage according to the leakage operator, which acts like in equation (3.31), but with MP replaced with $G_E MP$:

$$G_E MG_E MP = G_E G_E MP - L_M G_E MP; \quad (3.33a)$$

$$G_B MG_E MP = G_B G_E MP + L_M G_E MP. \quad (3.33b)$$

These equations simplify using $G_E G_E = G_E$ and $G_B G_E = 0$. Then, substituting equation (3.31a) into the new leakage terms,

$$G_E MG_E MP = G_E MP - L_M (G_E P - L_M P); \quad (3.34a)$$

$$G_B MG_E MP = L_M (G_E P - L_M P). \quad (3.34b)$$

So far the equations are exact. Two approximations are made which yield the template. Relying on the dominance of the E mode over the B mode, we first assume that $L_M G_E P \approx L_M P$. Second, the double leakage term $L_M L_M P$ is assumed to be half the original leakage: $L_M L_M P \approx \frac{1}{2} L_M P$, which can be motivated by the notion that the leakage operator applied to increasingly corrupted maps will tend (on average) to mix them evenly between E and B. Assuming that the B mode is small, then the first approximation should hold with good accuracy, and the second is also observed to be approximately true.

Therefore, the leakage $L_M P$ is approximately proportional to $G_B MG_E MP$, and the constant of proportionality is expected to be approximately 2. The quantity $G_B MG_E MP$ is known and can be computed with the available data.¹ It is therefore the template for the leakage, which is subtracted from the corrupted B map to estimate the true B map.

In an implementation, it is not necessary to use the assumption that the constant of proportionality is 2. Instead, the template $G_B MG_E MP$ can be linearly removed from the corrupted B mode. It is observed that the corresponding coefficient calculated empirically in this way is almost always close to 2.

3.4 TESTS

In figures 3.2 and 3.3, individual realizations of each of the methods are illustrated in two shapes of mask. Larger illustrations of method 2 on a lower-resolution map are also shown in figures 3.10 and 3.11 at the end of the chapter.

¹Known quantities are easily identified because they end with MP; unknown quantities include a P that is not acted on by an M.

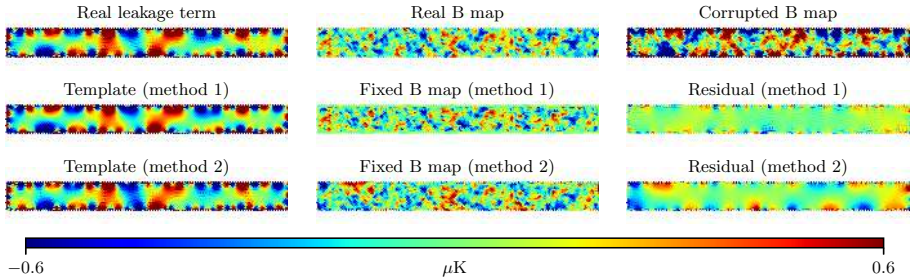


Figure 3.2: Leakage, templates, and correction for a narrow belt mask.

In the following, the performance method is tested on FFP9 simulations [140], constructed with a tensor-to-scalar ratio of $r = 0.05$. Region 1 is taken to be a disk with radius 47° , which covers about 15% of the sky. This region is comparable with the observation region in the specification of the GreenPol experiment.

Zero B mode

A simple null test is possible in which the true B mode is artificially set to 0. In addition to removing the cosmological signal, we also remove noise and lensing effects, so the true B mode is exactly 0. Under these idealistic circumstances, the entire recovered B mode is due to leakage.

The left panel of figure 3.4 shows the observed B mode, which consists entirely of leakage. The middle panel shows the template derived from the recycling method. The agreement is very strong.

The B mode power spectra estimated from this example are shown in figure 3.5 before and after correction. The spectra are calculated both with and without apodization using a Tukey window function with a taper fraction of 0.1, illustrated in the inset of figure 3.5. A taper fraction of 0.1 corresponds approximately to a smoothing scale of 5° for this mask. The window function reduces high- ℓ power in both the corrupted and corrected B modes. On the whole, the corrected spectrum is smaller, and therefore more accurate, than the corrupted one by about 5 orders of magnitude for $\ell < 100$, and about 4 orders of magnitude for $100 < \ell < 1000$.

Combination with the MASTER method

The map-domain E–B leakage correction, though worthy in its own right, can also be used as part of the reconstruction of the B mode spectrum. In this case, however, the problem

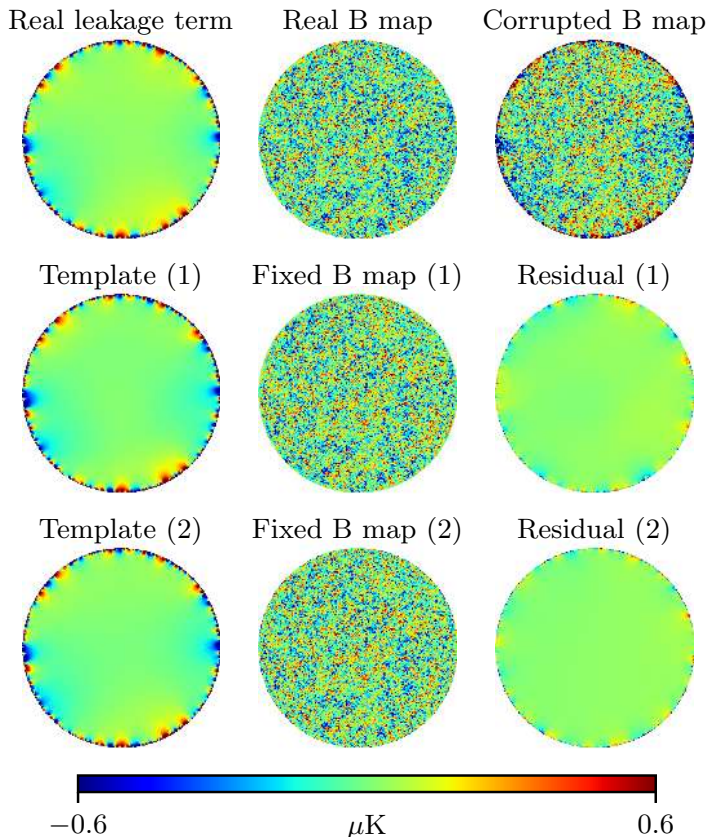


Figure 3.3: Leakage, templates, and correction for a large disk mask.

is estimation of the power spectrum of a masked *scalar* function, which is well studied [100, 141–144], and any of the various techniques is applicable. A widely used technique is the MASTER method, which is a well-known algorithm giving an unbiased estimate of the full-sky power spectrum from partial sky data [142]. MASTER is used here with the namaster implementation [145]. The full-sky power spectrum is estimated from the simulated partial sky data in two ways: first, purification of the B mode, based on the Smith method [134–136], which is similar to the Bunn method discussed in section 4.1; and second, a normal non-polarized power spectrum estimation, using MASTER alone, on the B mode map corrected in the pixel domain using the recycling method as above. These are then compared to the true power spectrum estimated by MASTER using the real B map.

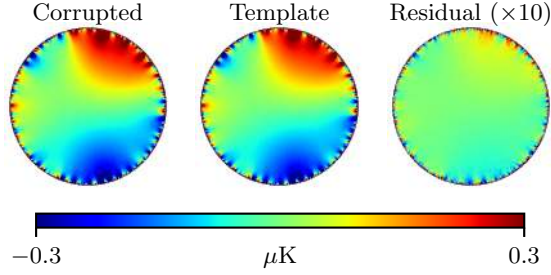


Figure 3.4: From left to right: the observed B mode (which is entirely leakage), the template derived from the recycling method, and their difference magnified by a factor of 10 for visibility.

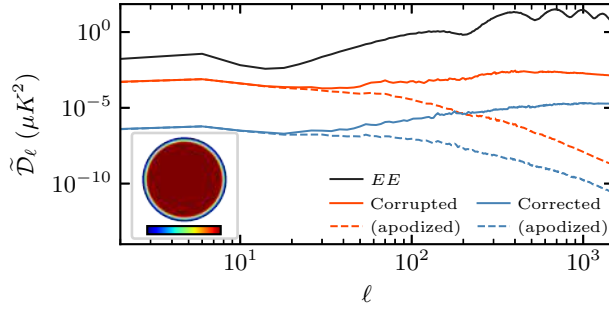


Figure 3.5: Estimated B mode power spectra from figure 3.4. The inset shows the apodization used for estimation of the dashed power spectra.

The error is characterized using an root mean square over simulations. The starting point is the absolute difference of the true B mode spectra and the estimated B mode spectra, from either the pure method or the real-space-correction method:

$$\Delta_i(\ell) = (C_\ell)_i - (C_\ell^{\text{true}})_i, \quad (3.35)$$

where the index i numbers each simulation. Then the overall error of each method is measured using

$$\Delta(\ell) = \sqrt{\frac{1}{N_{\text{sim}}} \sum_{i=1}^{N_{\text{sim}}} \Delta_i(\ell)^2}. \quad (3.36)$$

Using 50 simulations with the same specifications as before, the values of Δ are shown in figures 3.6 and 3.7. The same plots show the true B mode spectra for $r = 10^{-2}$, $r = 10^{-3}$,

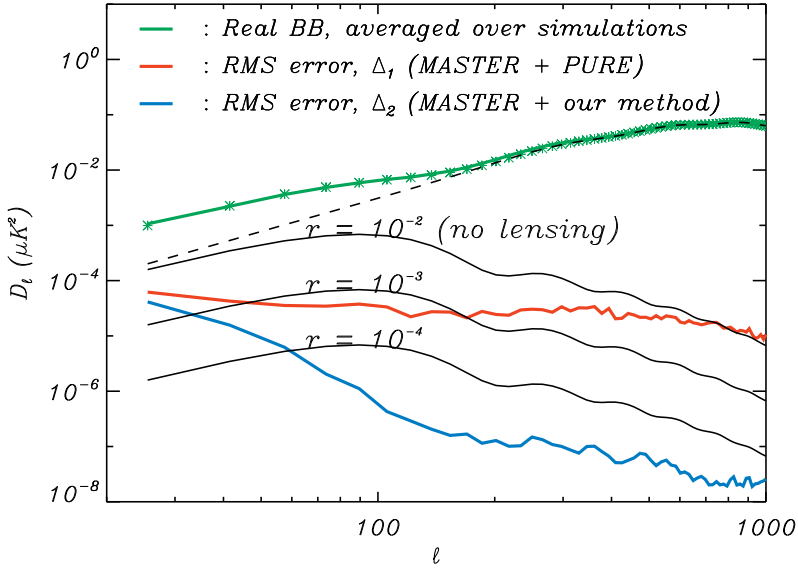


Figure 3.6: Performance of E-B leakage correction according to the RMS (defined in the text) from purified MASTER (red) and MASTER plus the recycling method (blue). The real B spectrum is shown in green, and the lensing spectrum is shown by the black dashed line, together with expected primordial B mode spectra expected from $r = 10^{-2}$, $r = 10^{-3}$, and $r = 10^{-4}$.

and $r = 10^{-4}$. In general, the real-space correction reduces the error in the final power spectrum estimation by about 2 orders of magnitude compared to the pure method, in the interesting region around $\ell \approx 100$. The improvement is dependent on ℓ . At small $\ell < 20$, there is no improvement, and at large $\ell > 200$, the improvement is at the level of 3 orders of magnitude or more. This behavior with ℓ is by no means assumed to be general: the size and shape of the observed region, and other properties of the simulations, likely have a significant influence on how the errors scale with ℓ . Nevertheless, under the conditions simulated here, which are not unrealistic, the real-space correction offers substantial improvement over the pure method.

The uncertainties using the real space correction are below the level of the theoretical $r = 10^{-4}$ power spectrum at the first peak and above, compared to $r \approx 10^{-3}$ for the pure method. For lower multipoles, the sensitivity of both methods approaches $r \approx 10^{-2}$. Of course, this setup excludes the errors due to foreground residuals, noise, delensing, etc., so

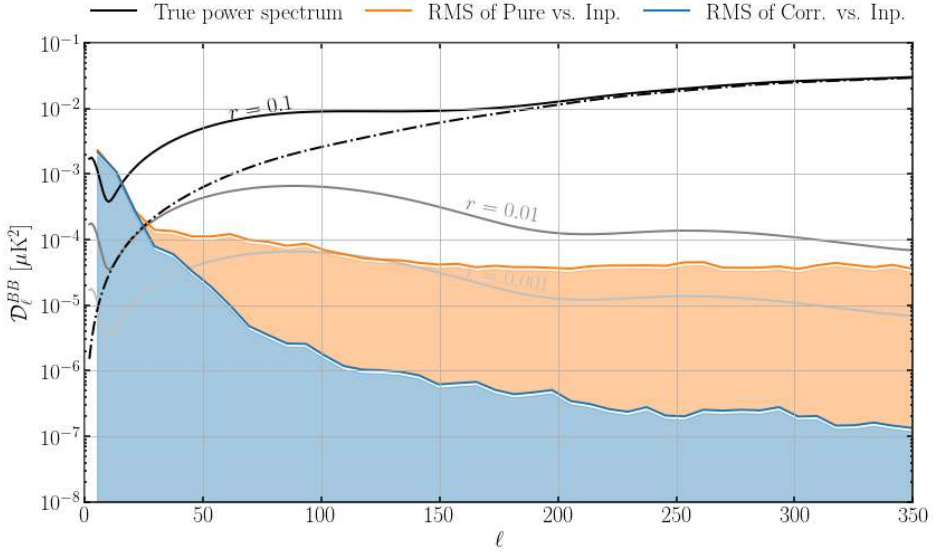


Figure 3.7: Similar to figure 3.6. Performance of E-B leakage correction from purified MASTER (orange) and MASTER plus the recycling method (blue). The real B spectrum, shown in black, is here simulated with $r = 0.1$.

the conclusion is not that $r = 10^{-5}$ is detectable, but that leakage does not exclude detection of $r = 10^{-5}$.

Optimization of the posterior apodization

The MASTER code was run using the default 10° apodization length for both the pure method and the real-space correction method. Optimization of the window function for the pure method was studied in [146]. Under comparable circumstances with a circular mask, an improvement of significantly less than one order of magnitude in the power spectrum error was achievable. We test different window functions for the real space correction method. The optimal window function is expected to depend strongly on the shape of the mask. Therefore, each specific simulation setup should be tested in realistic circumstances. Below, we continue to use the 47° disk mask based on the GreenPol telescope.

In the signal processing literature, window functions are normally defined in one dimension. The window function is $w(x)$, where $0 \leq x \leq 1$, and it is also usually symmetric: $w(0.5 - x) = w(0.5 + x)$. One-dimensional window functions can be applied

to an unmasked region of arbitrary shape on the sky by defining the corresponding two-dimensional window function as

$$W_{\Omega}(\hat{n}) = w\left(\frac{d(\hat{n})}{2\max_{\hat{n}\in\Omega}(d(\hat{n}))}\right), \quad (3.37)$$

where $d(\hat{n})$ is the distance from \hat{n} to the edge of the mask. According to this definition, $W_{\Omega}(\hat{n})$ is 0 at the edge of the region, and equal to the central value $w(0.5)$ (usually 1) at points most distant to the edge.

The computation of $d(\hat{n})$ in practice is by no means trivial, depending on how the mask is defined; a simple brute force method can be prohibitively expensive at high resolution. Where possible, symmetry of the mask should be exploited to simplify the calculation of $d(\hat{n})$.

Several different window functions are considered:

- Hamming (ha) and Tukey windows. The Tukey window depends on a taper fraction in the range $[0, 1]$, which is varied in increments of 0.1.
- Bartlett window (ba)
- Nuttall window (nu)
- Exact Blackman window (bl)

The performance of each window function is evaluated in two dimensions, which does not yield a simple optimum, but enables a clearer understanding of the tradeoff involved in apodization optimization. The effective sky fraction of the window function is

$$f_W = \frac{1}{N} \sum_{i=1}^N W^2(\hat{n}_i), \quad (3.38)$$

where \hat{n}_i , $i = 1, \dots, N$, are the coordinates of all pixels in the available region. f_W measures the aggressiveness of the window function. A top-hat mask has $f_W = 1$, while more aggressive masks have smaller f_W . Furthermore, the performance of the method after apodization is evaluated using an average of the relative error over a set of simulations, confined to a multipole range $\ell_1 \leq \ell \leq \ell_2$:

$$R = \sqrt{\frac{1}{N_{\text{sim}}(\ell_2 - \ell_1 + 1)} \sum_{\ell=\ell_1}^{\ell_2} \sum_{i=1}^{N_{\text{sim}}} \left(\frac{\Delta_i(\ell)}{(C_{\ell}^{\text{true}})_i} \right)^2}. \quad (3.39)$$

R is similar to the $\Delta(\ell)$ error estimate in equation (3.36) averaged over the specific multipole range, except that a *relative* error is used instead of an absolute error. R is defined with respect to a specific multipole range $[\ell_1, \ell_2]$, which should be adjusted to suit the

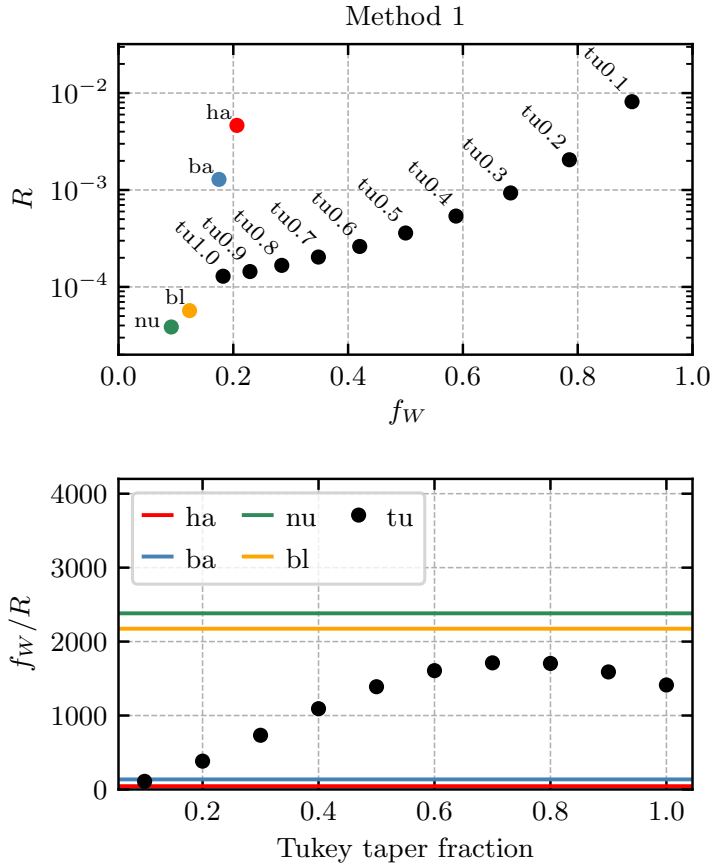


Figure 3.8: Performance metrics of method 1 (diffusive inpainting) for different choices of the apodization.

angular size of the mask under analysis as well as the scientific target. For the large and featureless disk mask used here, almost any multipole range is appropriate; for illustration below, $[\ell_1, \ell_2] = [60, 120]$ is used, including the recombination bump.

The performance of the window functions in the R/f_w space is shown in figures 3.8 and 3.9, for method 1 and method 2 respectively. Windows with smaller R give more accurate results, while windows with larger f_w retain more of the data. The optimal window functions therefore lie towards the lower right corner of the plots. The ideal optimum is a balance between these two considerations that depends on the specifics of the problem. In

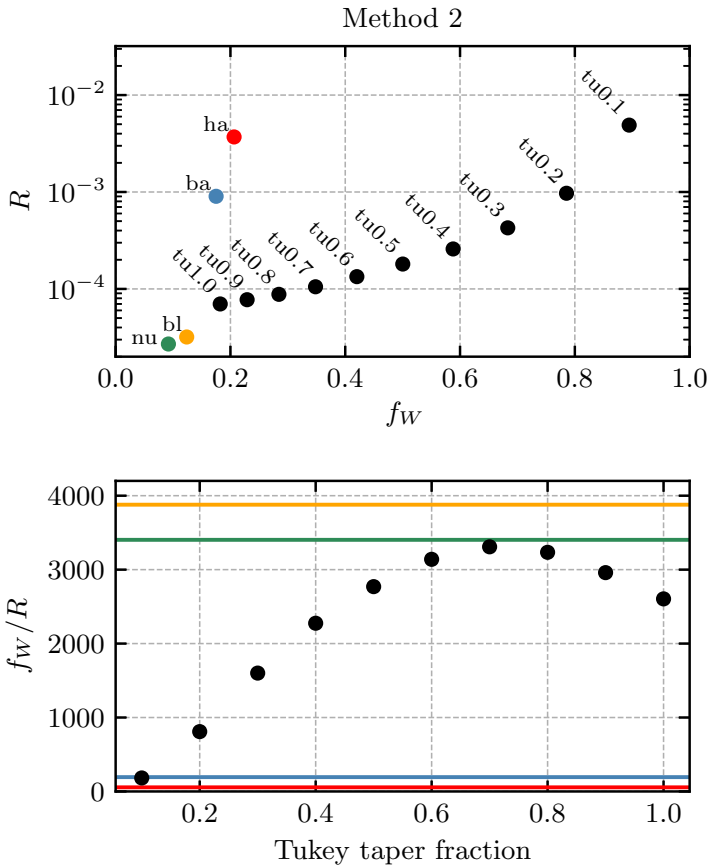


Figure 3.9: Performance metrics of method 2 (recycling method) for different choices of the apodization. Compared to figure 3.8, method 2 gives an error about 50% lower than method 1.

general, the Tukey window with 100% taper fraction is a good compromise; the Hamming and Bartlett windows are less aggressive but less accurate, and the Nuttall and Blackman windows are more aggressive but more accurate. Scaling back the Tukey taper fraction can significantly reduce the aggressiveness of the window with modest worsening of the accuracy, at least down to a taper fraction of about 0.5. These tapered Tukey windows make the Hamming and Bartlett windows almost redundant. Note, however, that this is a posterior apodization that applies specifically to the large circular disk mask in use,

in which leakage is very concentrated in the outermost parts of the mask. Masks with small-scale features will likely suffer greater in terms of accuracy using the less aggressive tapered Tukey windows. The lower panels of figure 3.8 and 3.9 plot the simple ratio f_W/R , which prefers a taper fraction of around 0.7.

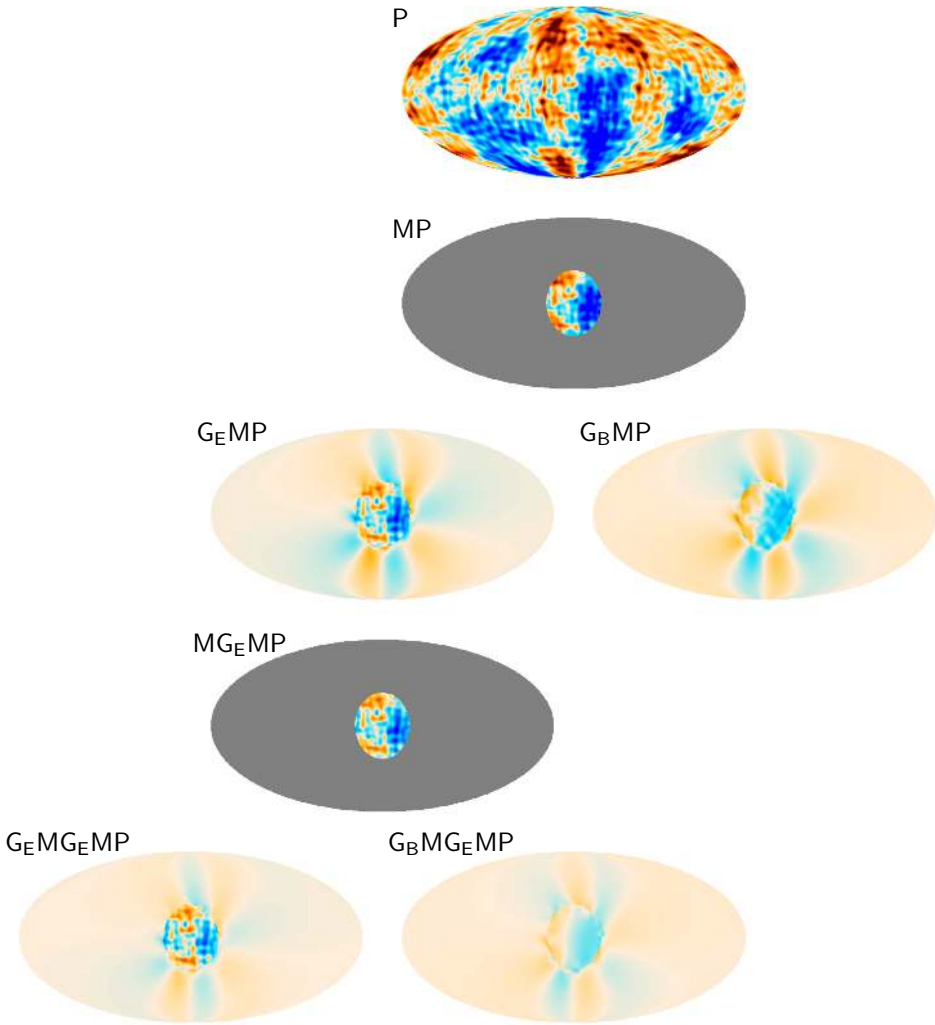


Figure 3.10: Overall summary of the recycling method scheme and the matrix notation, illustrated using one simulation. The Q component of \vec{P} is shown in all maps. The top map shows the true full-sky data, which is only observed in the disk region shown in the second row. The third row shows the full-sky E and B families of the masked data. The E family is remasked and further split into E and B. The resulting B component is the template for correcting the corrupted map. All maps use the same color scale.

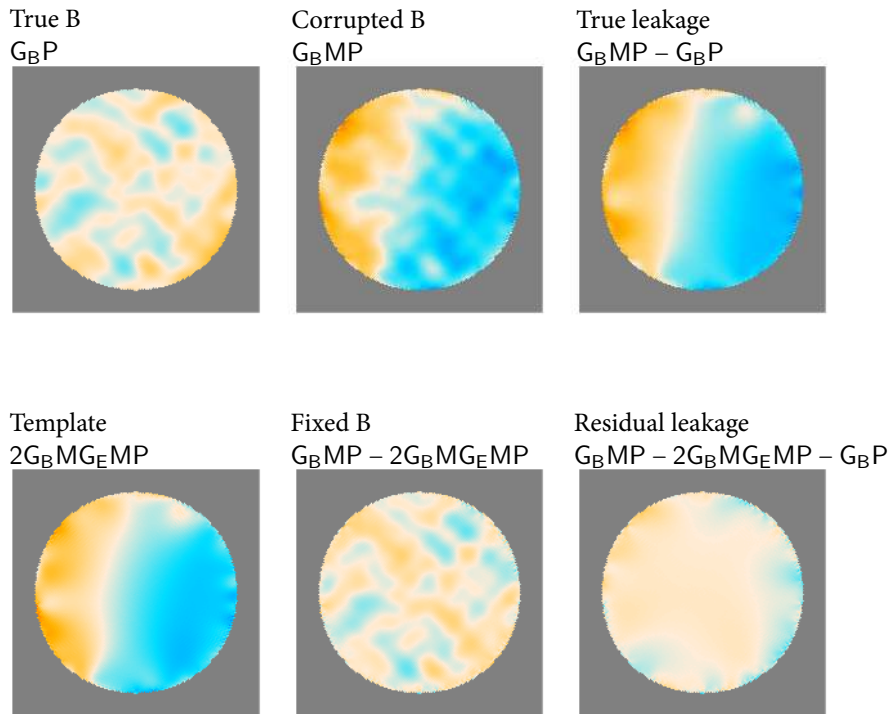


Figure 3.11: Same as figure 3.10, together with the true Q_B map, the fixed Q_B map, and the residual leakage after correction. All maps use the same color scale.

4 STATISTICS OF POLARIZATION ANGLES

The polarization of electromagnetic radiation has an orientation, but not a direction. The orientation can be described by an angle in the half plane, hence the factor of $1/2$ in the definition of the polarization angle ψ ,

$$\psi = \frac{1}{2} \arctan\left(\frac{U}{Q}\right), \quad (4.1)$$

constraining it to the range $-\pi/2 \leq \psi \leq \pi/2$. This factor is naturally compatible with the spin-2 transformation law obeyed by Q and U , found in equations (1.16) and (1.17).

The polarization angle is an understudied estimator so far. The dependence of ψ on the Q - U covariance was studied in [147] in the context of the WMAP data, although this work has received little attention. As discussed in [148], an independent measurement of the polarization angle leads to a method for debiasing the polarization intensity. This applies to, among other things, analysis of the polarized foregrounds, where the polarization angle is expected to be constant across frequency for certain types of foreground emission.

In this chapter, the goal is to generalize the theory of [147] to allow nonzero Q and U means, thereby fully characterizing the polarization angle expected from an arbitrary two-dimensional multivariate Gaussian distribution. This shows how the statistics of the Stokes parameters are reflected in the statistics of ψ . Asymptotics to leading order in the Q , U means, the Q - U covariance, and the difference between the Q and U variances produce a simple model of the pointwise distribution function of ψ , which takes the form of a constant $1/\pi$ density plus a non-uniform part consisting of $\sin(2\psi)$, $\cos(2\psi)$ modes and $\sin(4\psi)$, $\cos(4\psi)$ modes, each corresponding to a certain departure from the symmetric, uncorrelated case.¹

Furthermore, the polarization angles corresponding to the E and B modes are considered. These angles were defined previously in terms of the E and B families of the Stokes

¹The distribution of the polarization angle is exactly uniform only when Q and U are independent of each other and have zero mean and zero covariance.

parameters:

$$\psi_E = \frac{1}{2} \arctan\left(\frac{U_E}{Q_E}\right); \quad (4.2a)$$

$$\psi_B = \frac{1}{2} \arctan\left(\frac{U_B}{Q_B}\right). \quad (4.2b)$$

The geometric nature of the E and B modes constrains the statistics of their corresponding polarization angles.

These properties are derived and tested in the *Planck* 2018 maps. This work is published in [20].

4.1 POLARIZATION ANGLE DISTRIBUTION FUNCTIONS

The Stokes parameters have pixel-domain correlations, e.g. $Q(\hat{n}_1)$ and $Q(\hat{n}_2)$ are correlated random variables for different \hat{n}_1 and \hat{n}_2 : therefore, for instance, the set of all $Q(\hat{n})$ values in a map are not independent and identically distributed. For now, we consider point statistics only, and Q and U should be understood to be the single Q and U values at a certain point.

Q and U , then, are assumed to be random Gaussian variables with means μ_Q, μ_U and covariance

$$\Sigma_{QU} = \begin{pmatrix} \sigma_{QQ} & \sigma_{QU} \\ \sigma_{QU} & \sigma_{UU} \end{pmatrix}. \quad (4.3)$$

The determinant of the covariance matrix is

$$|\Sigma_{QU}| = \sigma_{QQ}\sigma_{UU} - \sigma_{QU}^2. \quad (4.4)$$

The joint probability density of Q and U is

$$\mathcal{P}(Q, U) = \frac{1}{2\pi|\Sigma_{QU}|} \exp\left(-\frac{1}{2}(\vec{P} - \vec{\mu})^T \Sigma_{QU}^{-1}(\vec{P} - \vec{\mu})\right), \quad (4.5)$$

where

$$\vec{P} = \begin{pmatrix} Q \\ U \end{pmatrix} \quad \text{and} \quad \vec{\mu} = \begin{pmatrix} \mu_Q \\ \mu_U \end{pmatrix} \quad (4.6)$$

are ‘‘vector-like’’ representations of the Stokes parameters and their means.

The distribution function of the polarization angle ψ is essentially a marginalization of equation (4.5), obtained by integration over all values of the polarization intensity $I = \sqrt{Q^2 + U^2}$. This was calculated in [147] in the case that $\mu_Q = \mu_U = 0$; the result is

$$\mathcal{P}(\psi) = \frac{2\sqrt{|\Sigma_{QU}|}}{\pi f_\sigma(\psi)}, \quad (4.7)$$

where $f_\sigma(\psi)$ is defined as

$$f_\sigma(\psi) = \sigma_{QQ} + \sigma_{UU} + (\sigma_{UU} - \sigma_{QQ}) \cos(4\psi) - 2\sigma_{QU} \sin(4\psi). \quad (4.8)$$

The simplest possible special case is uncorrelated Q and U with equal variances. Under substitution of $\sigma_{QQ} = \sigma_{UU}$ and $\sigma_{QU} = 0$, the distribution function reduces to a uniform distribution on the domain, i.e. $\mathcal{P}(\psi) = 1/\pi$. Otherwise, the distribution is made non-uniform by the $\cos(4\psi)$ and $\sin(4\psi)$ terms in $f_\sigma(\psi)$, whose amplitudes are proportional to the variance difference and the covariance.

It is informative to consider asymptotics of equation (4.7) because in many situations both the variance differential (i.e. $\sigma_{UU} - \sigma_{QQ}$) and the covariance σ_{QU} can be expected to be small quantities. The leading order expansion of equation (4.7) in these quantities is

$$\mathcal{P}(\psi) = \frac{1}{\pi} \left(1 + \frac{(1-R) \cos(4\psi) + \kappa \sin(4\psi)}{1+R} \right), \quad (4.9)$$

written in terms of the variance ratio

$$R = \frac{\sigma_{UU}}{\sigma_{QQ}} \quad (4.10)$$

and the relative covariance

$$\kappa = \frac{\sigma_{QU}}{\sigma_{QQ}}. \quad (4.11)$$

This distribution function is a linear combination of 4ψ sines and cosines. The sine and cosine terms in equation (4.8) have coefficients that are small.

Equations (4.7) and (4.9) only hold when the means of Q and U are zero. In general, this may not be exactly true. Therefore it is necessary to modify the foregoing theory to allow for nonzero means. The general result is¹

$$\mathcal{P}(\psi) = \frac{2f_\mu(\psi)}{\pi f_\sigma(\psi)^{3/2}} \exp\left(-\frac{(\mu_U \cos(2\psi) - \mu_Q \sin(2\psi))^2}{f_\sigma(\psi)}\right) \left(\frac{e^{-f_{\mu\sigma}(\psi)^2}}{f_{\mu\sigma}(\psi)} - \sqrt{\pi} \operatorname{erfc}(f_{\mu\sigma}(\psi))\right). \quad (4.12)$$

In addition to the variance factor $f_\sigma(\psi)$, equation (4.12) also includes the mean factor

$$f_\mu(\psi) = (\mu_U \sigma_{QU} - \mu_Q \sigma_{UU}) \cos(2\psi) + (\mu_Q \sigma_{QU} - \mu_U \sigma_{QQ}) \sin(2\psi) \quad (4.13)$$

and the mean–variance factor

$$f_{\mu\sigma}(\psi) = \frac{f_\mu(\psi)}{\sqrt{|\Sigma_{QU}| f_\sigma(\psi)}}. \quad (4.14)$$

¹This is a standard result in the statistical theory of directional data; see, e.g., [149, 150].

Mode	Source	Amplitude
$\cos(2\psi)$	nonzero Q mean	$\mu_Q/\sqrt{\sigma}$
$\sin(2\psi)$	nonzero U mean	$\mu_U/\sqrt{\sigma}$
$\cos(4\psi)$	unequal Q, U variances	$\Delta\sigma/\sigma$
$\sin(4\psi)$	nonzero $Q-U$ covariance	σ_{QU}/σ

Table 4.1: The leading order nonuniform modes in the polarization angle distribution function, their sources, and the scaling of their amplitudes.

Despite foreboding appearances, it can be seen in these equations that the nonuniformity enters in the form of $\cos(2\psi)$ and $\sin(2\psi)$ terms with amplitudes linearly depending on the means μ_Q and μ_U . Straightforward substitution of $\mu_Q = \mu_U = 0$ into equation (4.12) produces indeterminate forms like $0/0$, which when handled correctly simplify to equation (4.7).

Various other special cases of equation (4.12) can be considered. The nonuniformity induced by nonzero means at first order is

$$\mathcal{P}(\psi) = \frac{1}{\pi} + \frac{\mu_Q \cos(2\psi) + \mu_U \sin(2\psi)}{\sqrt{2\pi\sigma_{QQ}}}. \quad (4.15)$$

Together with equation (4.9), the main forms of modulations expected in near-uniform polarization angle distributions are shown in table 4.1, and the shapes are shown in figures 4.1 and 4.2.

Q, U means and the E and B modes

The means μ_Q and μ_U appearing in the point distribution functions are constant parameters in a statistical model. They are conceptually different from the full-sky averages of any particular Q and U maps, i.e. their monopoles, which deviate from the underlying means due to random fluctuations on a finite sample. However, provided that the correlation length of the map is sufficiently small, there is convergence in these two values. The full-sky average of a Q map,

$$\bar{Q} = \frac{1}{4\pi} \int Q(\hat{n}) d\hat{n}, \quad (4.16)$$

can itself be considered a Gaussian random variable (with respect to different realizations of the CMB) with expectation value μ_Q and standard deviation related to the correlation length. This distinction is minor in most practical circumstances, but the monopoles will continue to be denoted by \bar{Q} and \bar{U} instead of μ_Q and μ_U .

The full-sky map means of Q and U , i.e. their monopoles, are closely related to the E and B power spectra. Substituting equation (2.7) for the harmonic decomposition of $Q(\hat{n})$

and $U(\hat{n})$ into equation (4.16), the mean of Q can be expressed as

$$\bar{Q} = \frac{1}{8\pi} \sum_{\ell m} \int (a_{2,\ell m 2} Y_{\ell m}(\hat{n}) + a_{-2,\ell m -2} Y_{\ell m}(\hat{n})) d\hat{n}. \quad (4.17)$$

The full-sky integration of the spin-weighted spherical harmonics vanishes except for $m = 0$, whence further possible simplifications emerge because the $m = 0$ spin-weighted spherical harmonics are real-valued and obey ${}_2 Y_{\ell 0} = -{}_2 Y_{\ell 0}$.

$$\bar{Q} = \frac{1}{8\pi} \sum_{\ell} \int (a_{2,\ell 0 2} Y_{\ell 0}(\hat{n}) + a_{-2,\ell 0 -2} Y_{\ell 0}(\hat{n})) d\hat{n} \quad (4.18a)$$

$$= \frac{1}{8\pi} \sum_{\ell} \int (a_{2,\ell 0} + a_{-2,\ell 0}) {}_2 Y_{\ell 0}(\hat{n}) d\hat{n} \quad (4.18b)$$

$$= -\frac{1}{4\pi} \sum_{\ell} a_{\ell 0}^E \int {}_2 Y_{\ell 0}(\hat{n}) d\hat{n}. \quad (4.18c)$$

In the last line, the definition of $a_{\ell m}^E$ has been used, equation (2.8). A similar derivation yields the same type of expression for \bar{U} , but the B mode coefficient appears in place of the E mode coefficients:

$$\bar{U} = -\frac{1}{4\pi} \sum_{\ell} a_{\ell 0}^B \int {}_2 Y_{\ell 0}(\hat{n}) d\hat{n}. \quad (4.19)$$

The series

$$Y_{\ell} = \frac{1}{4\pi} \int {}_2 Y_{\ell 0}(\hat{n}) d\hat{n}, \quad (4.20)$$

which functions as the weights acting on $a_{\ell 0}$ in the above equations, has the closed form

$$Y_{\ell} = \begin{cases} \sqrt{\frac{2\ell + 1}{\pi} \frac{(\ell - 2)!}{(\ell + 2)!}}, & \text{if } \ell \text{ is even} \\ 0, & \text{if } \ell \text{ is odd} \end{cases} \quad (4.21)$$

Therefore it is the even- ℓ coefficients which contribute to the full-sky means. Y_{ℓ} diminishes rapidly with increasing ℓ ; the contribution is dominated by the first few even modes, depending on how rapidly the power spectra decay. In fact, to good approximation, \bar{Q} and \bar{U} is determined by just $\ell = 2$ and $\ell = 4$; the series Y_{ℓ} is plotted in figure 4.3.

In general, there is usually not *a priori* expectation for the specific values of $a_{\ell m}^{E/B}$, on which \bar{Q} and \bar{U} depend. When only the power spectra C_{ℓ}^{EE} and C_{ℓ}^{BB} are specified, then \bar{Q} and \bar{U} are not determined. However, if we assume Gaussianity such that C_{ℓ} is the expected variance of $a_{\ell m}$ at that ℓ , then C_{ℓ}^{EE} and C_{ℓ}^{BB} do determine the probability distributions for \bar{Q} and \bar{U} . In each Gaussian realization of the CMB, \bar{Q} and \bar{U} can be modelled as random

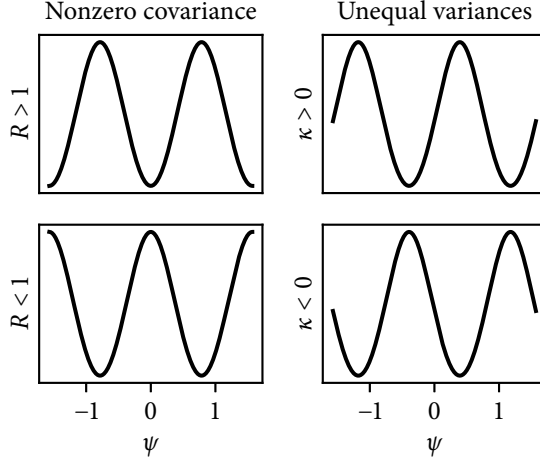


Figure 4.1: Phases of the $\cos(4\psi)$ and $\sin(4\psi)$ modes.

variables drawn from Gaussian distributions having zero mean and variance

$$\text{var}(\bar{Q}) = \sum_{\ell} C_{\ell}^{EE} Y_{\ell}^2; \quad (4.22a)$$

$$\text{var}(\bar{U}) = \sum_{\ell} C_{\ell}^{BB} Y_{\ell}^2. \quad (4.22b)$$

Based on this formalism, we expect the distribution function for Q monopoles to be significantly broader than the distribution function for U monopoles, assuming that $C_{\ell}^{EE} \gg C_{\ell}^{BB}$ at low ℓ .

The recurring association between Q and E , and between U and B , appears in these equations.

E and B polarization angles

In equation (2.16), polarization angles of the E and B modes were defined as

$$\psi_E = \frac{1}{2} \arctan\left(\frac{U_E}{Q_E}\right); \quad (4.23a)$$

$$\psi_B = \frac{1}{2} \arctan\left(\frac{U_B}{Q_B}\right). \quad (4.23b)$$

In principle, these obey the same statistics as the normal polarization angle ψ discussed above. However, there is an important constraint on the Stokes parameters of the E and B

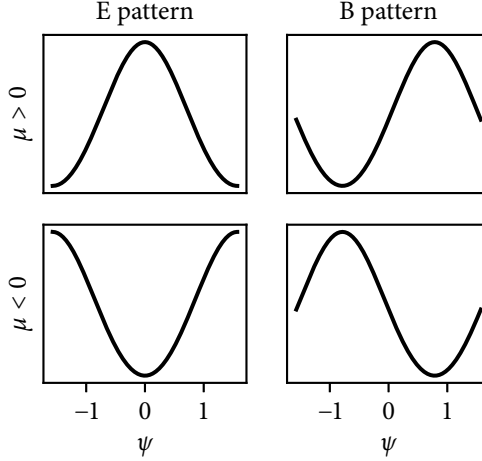


Figure 4.2: Phases of the $\cos(2\psi)$ and $\sin(2\psi)$ modes from the nonzero means μ_Q and μ_U . The E and B families are constrained to have zero U and Q means respectively, so ψ_E and ψ_B are constrained to one of these two specific phases. In general, unseparated polarization data can have an arbitrary phase.

modes. The U_E and Q_B maps are forbidden from having any monopole component—their full-sky averages are exactly zero, $\overline{U}_E = \overline{Q}_B = 0$. Meanwhile, Q_E and U_B have the same monopole as the original unseparated Q and U respectively. These results follow from equations (4.18) and (4.19).

Thus there are unique E and B patterns of the 2ψ mode, distinguished by the phase, labelled in figure 4.2. These patterns reflect the geometry of the E and B modes.¹

Partial-sky analysis

Several issues apply to partial-sky analysis of polarization angles. First, we repeat that equation (4.5) is the distribution function for a single pixel. A region of the sky cannot be modeled in this way if the correlation length is comparable to the size of the region. This is briefly and vaguely mentioned in [147], in which the authors point out that the inter-pixel correlations do not affect expectation values, and the mean number of pixels in each bin of a histogram calculated from the data is given by the point distribution function in the

¹Although ψ_E and ψ_B were constructed through the use of the E and B families (Q_E, U_E) and (Q_B, U_B) , the patterns in the angle distribution functions are not tied to this construction. For example, the normal unseparated polarization angle ψ of a polarization field, which is purely E and has no B mode, will have the same shape.

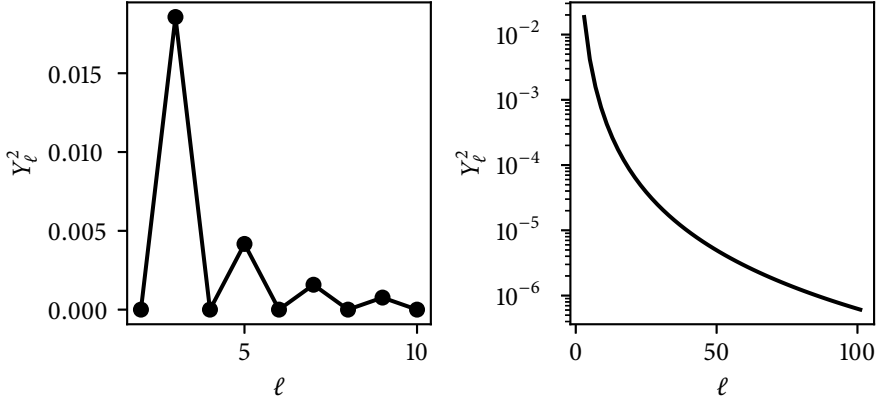


Figure 4.3: The series Y_ℓ^2 , which are the weights of the contribution of the E or B power spectra to the variance of μ_Q or μ_U , as stated in equations (4.22a) and (4.22b). The curve in the right panel shows the values for even ℓ only.

simplest way. Most likely, it is necessary to work with simulations, when small regions of the sky are considered, in which the sampling uncertainty is significant.

Furthermore, the zero mean constraints on Q_B and U_E are broken on the partial sky. There is also the question of leakage.

In the results that follow, the common polarization mask or the confidence mask associated with the component separation method are generally used.

Polarization angle distributions in SMICA

In figure 4.4, the polarization angle distribution measured from SMICA is shown. The sky has been masked with the polarization confidence mask, and the map is otherwise unprocessed ($N_{\text{side}} = 2048$). Also plotted are curves corresponding to three Gaussian models: the fully Gaussian model of equation (4.12), the equal variance/zero covariance model of equation (4.9), and the zero-mean model of equation (4.15). In all three cases, the unneglected means and variances are sample estimates from the data.

Figure 4.4 shows clearly that the polarization angles in the full-resolution SMICA map have fluctuations of approximately $\pm 2\%$ from a uniform $1/\pi$ distribution. The overall non-uniform part is a roughly even superposition of 2ψ and 4ψ modes (the two dashed curves in figure 4.4 have almost the same amplitude). It need not necessarily be that the means and variances have similar statistical departures from the null assumptions. Smoothing or downgrading the map, which keeps the means fixed but reduces the variances, tends to diminish the 4ψ mode and produce polarization angle distributions dominated by the 2ψ

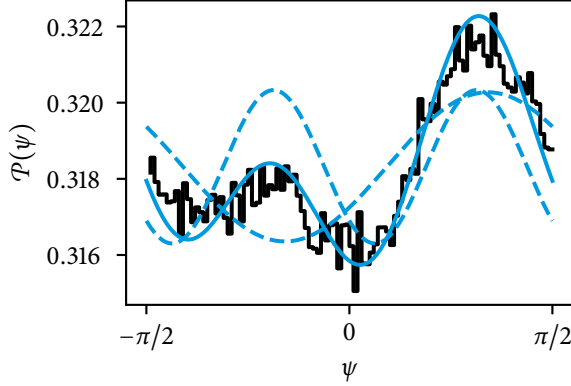


Figure 4.4: Empirical distribution function of the polarization angle from SMICA (black) compared to the theoretical Gaussian model (blue). The 2ψ and 4ψ modes are shown separately as dashed curves.

mode.

As a final remark, we consider the validation of the leading order models in (4.9) and equation (4.15). The total leading order model is constructed by adding the non-uniform parts of each asymptotic model to $1/\pi$:

$$\mathcal{P}_{\mu\sigma} = \frac{1}{\pi} + \left(\mathcal{P}_{\mu}(\psi) - \frac{1}{\pi} \right) + \left(\mathcal{P}_{\sigma}(\psi) - \frac{1}{\pi} \right) \quad (4.24a)$$

$$= \frac{1}{\pi} + \frac{\mu_Q \cos(2\psi) + \mu_U \sin(2\psi)}{\sqrt{2\pi\sigma_{QQ}}} + \frac{(1-R) \cos(4\psi) + \kappa \sin(4\psi)}{\pi(1+R)}. \quad (4.24b)$$

The same asymptotic model can be derived by a series expansion of equation (4.12), but there are cumbersome singularities. For the values of μ_Q , μ_U , and Σ_{QU} estimated from full-resolution SMICA, equation (4.24b) is the same as equation (4.12) to within an absolute error of around 10^{-5} , indicating that we are well within the leading order regime.

The polarization angle theory naturally invites an investigation of the sample statistics themselves, especially in light of equations (4.22a) and (4.22b), which show how these are related to the cosmologically interesting E and B power spectra.

4.2 STATISTICS OF GAUSSIANTY PARAMETERS

A natural companion to the investigation of the polarization angles in the *Planck* maps is a study of the Gaussianity parameters themselves: the means of Q and U , and the asymmetry parameters R and κ .

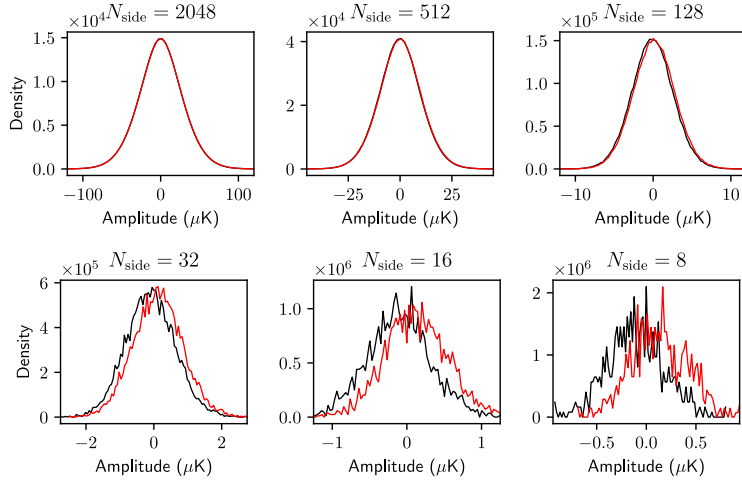


Figure 4.5: Distribution functions of SMICA Q (black) and U (red) for $N_{\text{side}} = 2048, 512, 128$ (top row) and $N_{\text{side}} = 64, 32, 16$ (bottom row). With decreasing resolution, the standard deviations shrink and the different Q, U means become increasingly visible.

Dependence on resolution

When a map is smoothed by a Gaussian filter or downgraded by averaging of merged subpixels, the mean stays the same, but the variance is reduced. Therefore the study of the Gaussianity parameters is resolution-dependent.

In figure 4.5, the empirical distribution functions of Q and U for the 2018 SMICA map are shown at different angular resolutions. The distributions are visibly Gaussian at high resolutions, with increasing random fluctuations at lower resolutions. As expected, the width of the distribution functions is seen to decrease with decreasing resolution. The means remain constant, and therefore the relative difference of the Q and U distribution functions from each other due to the offset shift induced by different Q and U means, which is almost negligible at full resolution, becomes very visible at lower resolution.

The trend is increasing sensitivity to nonzero means at lower resolutions, which is entirely expected. This is pronounced in the polarization angle distribution function, for which the amplitudes of the 2ψ modes are enhanced by diminishing variances (see table 4.1). The amplitudes of the 4ψ modes, which are ratios of variances, tend to stay the same. This behavior is illustrated for SMICA in figure 4.6. At low smoothing, all four modes have approximately the same amplitude around the 0.01 level (cf. figure 4.4), but at 1° smoothing, the 2ψ modes have more than quadrupled in amplitude.

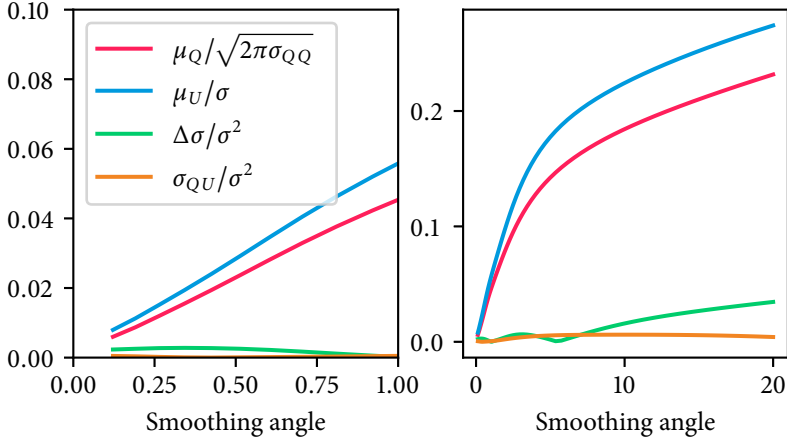


Figure 4.6: Amplitudes of the 4ψ and 2ψ modes as a function of the smoothing angle. These curves are based on 2018 SMICA, but the general behaviour is typical.

At very large smoothing angles, the trend breaks down when there can be significant random fluctuations in the variances.

Variance parameters

The variance-related asymmetry parameters of SMICA, NILC, Commander, and SEVEM at $N_{\text{side}} = 2048$, are shown in table 4.2. For all the CMB maps, we see $|R - 1|$ and $|\kappa|$ are of approximately similar size, meaning that both unequal variances and nonzero covariance are present in the data to a similar extent, and the polarization angle distributions have $\sin(4\psi)$ and $\cos(4\psi)$ modes with comparable amplitudes.

The variances of the SMICA and Commander maps are nearly equal to each other, while the variances in NILC and SEVEM are smaller. This is likely a reflection of the different high- ℓ cutoffs of the different component separation methods. In particular, SEVEM is limited by the resolution of the lowest-resolution input, which results in a final map with a lower resolution. The situation for the covariances is similar. Masking has a minor effect on the variances and a slightly more significant effect on the covariances, indicating that the Galactic plane region is a source of significant $Q-U$ covariance.

Q, U means

The means μ_Q and μ_U estimated from the SMICA, NILC, Commander, and SEVEM maps at $N_{\text{side}} = 2048$ are shown in table 4.3. Figure 4.7 shows the actual measured Q and U

Map	$\sigma_{QQ} (\mu\text{K}^2)$	$\sigma_{QU} (\mu\text{K}^2)$	R	κ
SMICA	813.552	-3.683	1.0089	-0.0045
Commander	802.189	-2.628	1.0089	-0.0033
NILC	646.368	-1.933	1.0072	-0.0029
SEVEM	436.429	-1.201	1.0076	-0.0028

Table 4.2: Q variance, Q–U covariance, and the R and κ parameters characterizing unequal variances and relative nonzero covariance at full resolution $N_{\text{side}} = 2048$.

Map	$\mu_Q (\mu\text{K})$	$\mu_U (\mu\text{K})$	$p_{\bar{Q}}$	$p_{\bar{U}}$
SMICA	-0.107	0.116	0.024	0.0
Commander	-0.093	0.116	0.049	0.0
NILC	-0.146	0.097	0.002	0.0
SEVEM	-0.118	0.143	0.012	0.0

Table 4.3: Q and U means and the two-sided p values with respect to the distributions implied by the power spectra.

means in each map, compared to the Gaussian distributions predicted by equation (4.22a) and (4.22b) evaluated using the E and B power spectra corresponding to the best-fit Λ CDM model.¹ For Q, the means are generally negative at around the $-0.1 \mu\text{K}$ level, which is departed from the expected value with a p value of less than $p = 0.05$. For U, on the other hand, the means are around the $+0.1 \mu\text{K}$ level, which is inconsistent with the Gaussian theory at almost unfathomably high significance.

In the 2015 *Planck* component separation products [98], the polarization maps were high-pass filtered, removing multipoles $\ell < 20$. These maps have effectively zero Q and U means, and they yield p values of nearly 0.5 when analyzed in the same way. As discussed in [98], the polarization maps were still heavily corrupted by systematics on scales above 10° , which is why these scales were simply filtered out of the maps. Following continued improvement in reducing systematics (discussed in [151–154]), the 2018 *Planck* component separation products [99] are not treated in this way. However, [99] warns that:

“We observe broad large-scale structures in both Stokes Q and U that are aligned with the Planck scanning strategy. These structures are effectively due to gain-modelling uncertainties coupled to monopole and dipole leakage, and corresponding features are present in the associated simulations. . . . In practice, however, we note that these modes are associated with significant additional systematic uncertainties, and we therefore caution against over-interpretation of the very largest scales in these maps.”

Bearing this in mind, the tension between the Q and U monopoles and the E and B

¹Specifically, the baseline *Planck* TT,TE,EE+lowE+lensing file is used.

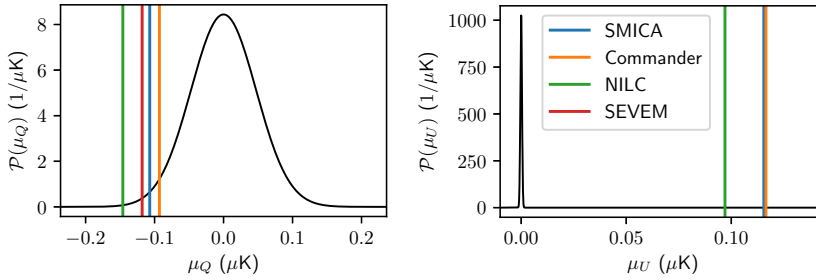


Figure 4.7: Actual extracted Q and U monopoles from the four *Planck* 2018 CMB maps, compared to the background distributions allowed assuming Gaussianity of Q and U and the best-fit E and B power spectra published by *Planck*. These two results are moderately incompatible for Q (i.e. the E mode) and extremely different for U (i.e. the B mode).

power spectra found here is almost certainly a manifestation of the large-scale systematics affecting the polarization maps. The distribution function of the polarization angle is sensitive to these systematic errors, and subtraction of the monopoles of Q and U , which may seem like a simple operation, can significantly alter the statistics of the polarization angle.

5 NON-POLARIZED POINTS AND THEIR STATISTICS

As discussed in chapter 1, in standard theories of inflationary cosmology, the CMB temperature anisotropy is expected to be a realization of a Gaussian random field, which is normally characterized by its power spectrum after harmonic transformation. The statistical description of Gaussian random fields in the map domain is somewhat more complicated, and there have been varied attempts to characterize the Gaussianity of the CMB in the map domain. Early works focused on peak statistics and “hot spots” in the maps [155–157]. Gaussianity puts statistical constraints on the frequency and shape of those regions exceeding some threshold intensity. More recently, saddle points have been exploited in a similar way [158].

Among other geometrical and topological estimators investigated for their sensitivity to Gaussianity (reviewed in [159]), the Minkowski functionals are the most popular [160–164]. Minkowski functionals depend on a threshold T_t , with respect to which are measured (1) the “hot” area of the sky where $T(\hat{n}) > T_t$, (2) the length of the boundary between the hot and cold regions, and (3) the Euler characteristic, which is calculated as the number of isolated regions above the threshold minus the number of regions below the threshold. Under Gaussianity, there exist analytic expressions for the expected values of the Minkowski functionals. Complementary to the peak statistics and the Minkowski functionals are the zero points, where $T(\hat{n}) = 0$, which should occur with a regular density in a Gaussian random field.

One of the major advantages of map domain analysis is that it is simple to constrain to certain parts of the sky. In this way, map domain estimators can be used to test not only Gaussianity but also isotropy. In [165], for example, Minkowski functionals and related estimators are applied to the northern and southern hemispheres separately, and the discrepancy between them is linked to the power asymmetry anomaly. Map domain estimators are also especially suitable for local analysis of small regions of the sky and upcoming ground-based datasets.

The possibilities for map-domain analysis are richer in polarization. The Minkowski functionals can also be adapted for use on polarization data [166]. The general existence of zero points in the polarization field, or non-polarized points, where the polarization intensity is identically zero, is feasible from the intermediate value theorem, although less

obvious. The Stokes parameters Q and U comprise a continuous, spin-2 function defined on the sphere. Continuity implies that there should exist well-defined contours where $Q = 0$, and similarly contours where $U = 0$ (so-called the “contours of percolation” [167]). The intersections of these contours are exactly the non-polarized points. Physically, at these points, the polarization signal is entirely canceled along the line of sight.

The zero points in polarization can be classified into three kinds according to the geometry of the local polarization field. The basic theory was largely presented in [166] and [168]. Here the theory is reviewed and extended, exploiting the Stokes-space decomposition of E and B, which allows the analysis to also be applied to the E and B modes. It is also shown that gravitational lensing has a specific signature in the non-polarized point density.

Additionally, concrete tests of Gaussianity using the theory of the non-polarized points are constructed. This complicates the analysis because it is not simply necessary to have a mean expectation, but also a variance. In practice, simulated data are used. Two test methodologies are described, based on the Kullback–Leibler divergence and the Kolmogorov–Smirnov estimator, intended to compare the properties of the non-polarized points in the actual data with simulations. The tests are localizable.

Further practical considerations for the detection of non-polarized points in pixelized sky maps are discussed and an overall algorithm is presented, followed by an application to the *Planck* 2018 maps. This work is published in [21].

5.1 GAUSSIAN THEORY

The correlated Gaussian model for Q and U , specified in equations (4.3) through (4.6), continues. Q and U are assumed to be random Gaussian variables with joint distribution

$$\mathcal{P}(Q, U) = \frac{1}{2\pi\sqrt{|\Sigma_{QU}|}} \exp\left(-\frac{1}{2}(\vec{P} - \vec{\mu})^T \Sigma_{QU}^{-1}(\vec{P} - \vec{\mu})\right). \quad (5.1)$$

In [166, 168], Q and U are assumed to be uncorrelated have the same variance, denoted σ_0^2 , and the means of Q and U are also assumed to be zero in this study, which is the primordial expectation. Under these assumptions, the distribution function is

$$\mathcal{P}(Q, U) = \frac{1}{2\pi\sigma_0^2} \exp\left(-\frac{1}{2} \frac{Q^2 + U^2}{\sigma_0^2}\right). \quad (5.2)$$

It is also necessary to describe the statistics of the field derivatives. The Jacobian is

$$J = \begin{pmatrix} \frac{\partial Q}{\partial \theta} & \frac{\partial Q}{\partial \phi} \\ \frac{\partial U}{\partial \theta} & \frac{\partial U}{\partial \phi} \end{pmatrix}. \quad (5.3)$$

The components of the Jacobian are, like Q and U , assumed to be zero-mean Gaussian random variables with a common variance, denoted $\sigma_1^2/2$, uncorrelated with each other

or Q and U . In this case, an overall joint distribution of Q , U , and their derivatives can be constructed as a simple product of Gaussians:

$$\mathcal{P}\left(Q, U, \frac{\partial Q}{\partial \theta}, \frac{\partial Q}{\partial \phi}, \frac{\partial U}{\partial \theta}, \frac{\partial U}{\partial \phi}\right) = \frac{4}{(2\pi)^3 \sigma_0^2 \sigma_1^4} \exp\left(-\frac{1}{2}\left(\frac{Q^2 + U^2}{\sigma_0^2} + 2\frac{\frac{\partial Q^2}{\partial \theta} + \frac{\partial Q^2}{\partial \phi} + \frac{\partial U^2}{\partial \theta} + \frac{\partial U^2}{\partial \phi}}{\sigma_1^2}\right)\right). \quad (5.4)$$

The factor of $1/2$ in the definition of the variance of the derivatives means that the gradients of Q and U ,

$$\nabla Q = \begin{pmatrix} \frac{\partial Q}{\partial \theta} \\ \frac{\partial Q}{\partial \phi} \end{pmatrix}; \quad \nabla U = \begin{pmatrix} \frac{\partial U}{\partial \theta} \\ \frac{\partial U}{\partial \phi} \end{pmatrix}, \quad (5.5)$$

have magnitudes with variance σ_1^2 . The ratio of σ_0 and σ_1 is then the correlation length of the map,

$$r_c = \frac{\sigma_0}{\sigma_1}. \quad (5.6)$$

Number density of non-polarized points

The probability density of non-polarized points is

$$\int \mathcal{P}(Q = 0, U = 0, J) dJ = \frac{4}{(2\pi)^3 \sigma_0^2 \sigma_1^4} \int \exp\left(-\frac{1}{\sigma_1^2}\left(\frac{\partial Q^2}{\partial \theta} + \frac{\partial Q^2}{\partial \phi} + \frac{\partial U^2}{\partial \theta} + \frac{\partial U^2}{\partial \phi}\right)\right) dQ_\theta dQ_\phi dU_\theta dU_\phi. \quad (5.7)$$

The Taylor expansion to first order around a non-polarized point at (θ_0, ϕ_0) ,

$$P(\theta_0 + d\theta, \phi_0 + d\phi) = P(\theta_0, \phi_0) + J(\theta_0, \phi_0) \begin{pmatrix} d\theta \\ d\phi \end{pmatrix}. \quad (5.8)$$

The constant term vanishes by definition, leaving the linear term

$$J(\theta_0, \phi_0) \begin{pmatrix} d\theta \\ d\phi \end{pmatrix} = \begin{pmatrix} \frac{\partial Q}{\partial \theta} & \frac{\partial Q}{\partial \phi} \\ \frac{\partial U}{\partial \theta} & \frac{\partial U}{\partial \phi} \end{pmatrix} \begin{pmatrix} d\theta \\ d\phi \end{pmatrix}. \quad (5.9)$$

The linear regime in the immediate vicinity of a non-polarized point has Q and U in bijection with θ and ϕ . By a change of coordinates, the number density can therefore be written using the probability density, but it acquires a factor of $|\det(J)|$:

$$N_{\text{np}} = \frac{4}{(2\pi)^3 \sigma_0^2 \sigma_1^4} \int \exp\left(-\frac{1}{\sigma_1^2}\left(\frac{\partial Q^2}{\partial \theta} + \frac{\partial Q^2}{\partial \phi} + \frac{\partial U^2}{\partial \theta} + \frac{\partial U^2}{\partial \phi}\right)\right) |\det(J)| dQ_\theta dQ_\phi dU_\theta dU_\phi. \quad (5.10)$$

Field trajectories near non-polarized points

Near a non-polarized point, the eigenvalues of the Jacobian J determine the local dynamics of the polarization field. We work in local coordinates, and assume that the derivatives are constant. The linearization is based on the derivatives evaluated exactly at the non-polarized point itself. The differential equation governing the field trajectories, which are parametrized as $(\theta(t), \phi(t))$, is

$$\begin{pmatrix} \dot{\theta} \\ \dot{\phi} \end{pmatrix} = J \begin{pmatrix} \theta \\ \phi \end{pmatrix} = \begin{pmatrix} Q_\theta & Q_\phi \\ U_\theta & U_\phi \end{pmatrix} \begin{pmatrix} \theta \\ \phi \end{pmatrix}. \quad (5.11)$$

The general solution can be given in terms of the eigenvalues of the Jacobian, which are the solutions to the characteristic equation

$$\lambda^2 - \text{Tr}(J) + \det(J) = 0, \quad (5.12)$$

i.e.,

$$\lambda_{\pm} = \frac{1}{2} \left(\text{Tr}(J) \pm \sqrt{\text{Tr}(J)^2 - 4\det(J)} \right). \quad (5.13)$$

Then the solution to equation (5.11) is

$$\theta(t) = C_1 \frac{Q_\phi}{\lambda_+ - Q_\theta} e^{\lambda_+ t} + C_2 \frac{\lambda_- - U_\phi}{U_\theta} e^{\lambda_- t}; \quad (5.14a)$$

$$\phi(t) = C_1 e^{\lambda_+ t} + C_2 e^{\lambda_- t}. \quad (5.14b)$$

C_1 and C_2 are constants of integration, which are fixed by an initial condition $(\theta(0), \phi(0))$. It has been assumed that the Q and U derivatives in the Jacobian are constant.

Classification of non-polarized points

The non-polarized point itself, $(\theta, \phi) = (0, 0)$, is a equilibrium point of the dynamical system. There are three qualitative behaviors of the trajectories, depending on the signs of the eigenvalues:

1. If both eigenvalues are real and have the same sign, then the point is a *node*. If $\lambda_+ > \lambda_- > 0$, then the node is called unstable, and all trajectories diverge to infinity; if $\lambda_+ < \lambda_- < 0$, then the node is called stable, and all trajectories approach the node.
2. If the eigenvalues are real and have opposite signs, the point is a *saddle*. All trajectories converge to the axis of the positive eigenvector.
3. If the eigenvalues are a pair of complex conjugates, then the point is a *focus*. The trajectories are spirals that approach the point if the real part is negative and diverge if the real part is positive.

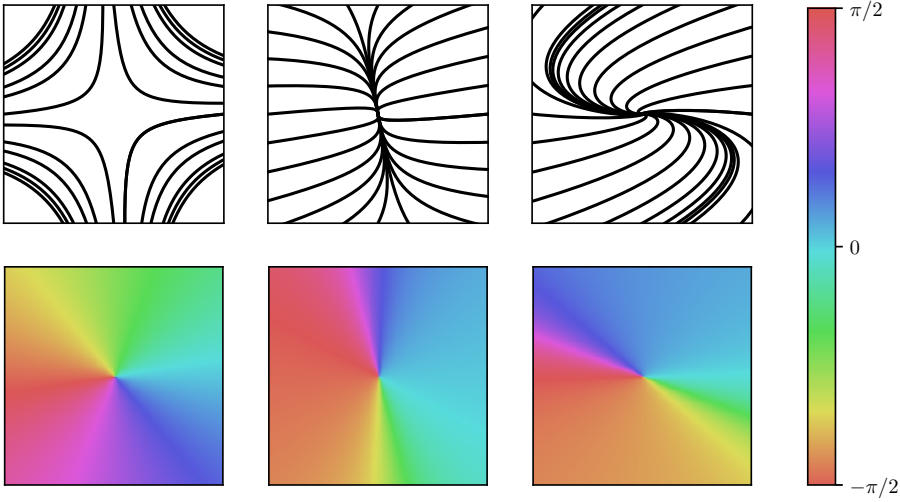


Figure 5.1: Different types of non-polarized points, from left to right, a saddle, a knot, and a focus. The first row shows the polarization field lines. The second row shows the polarization angle pattern local to the singular point, based on the derivatives of Q and U at the point.

The conditions on the eigenvalues can be stated equivalently in terms of the determinant and trace:

$$\begin{aligned} \det(J) > \left(\frac{1}{2}\text{Tr}(J)\right)^2 > 0 &: \quad \text{focus;} \\ \left(\frac{1}{2}\text{Tr}(J)\right)^2 > \det(J) > 0 &: \quad \text{node;} \\ \det(J) < 0 &: \quad \text{saddle.} \end{aligned}$$

In figure 5.1, sample trajectories are shown for the three types of points.

Number densities of nodes, saddles, and focuses

So far, this classification based on the qualitative behavior of the field line trajectories is entirely generic to any two-dimensional dynamical system. Now we return to the original premise, in which the dynamical systems in question arise at the zeros of the polarization intensity field. Within the Gaussian model, the Jacobian has specific statistical properties, which implies a distribution for the eigenvalues and therefore for the densities of the nodes, saddles, and focuses. The goal is to calculate the expected number density for each type.

What follows is the integration of the probability density over suitable regions of the phase space corresponding to each type of non-polarized point. The most important reference is the appendix of [166], where a sketch of the derivation is given.

The calculation begins with a change of variables as follows:

$$\frac{Q_\theta}{\sigma_1} = \frac{x}{2} + \frac{R}{2} \cos(\alpha); \quad (5.15a)$$

$$\frac{Q_\phi}{\sigma_1} = \frac{R}{2} \sin(\alpha) - \frac{w}{2}; \quad (5.15b)$$

$$\frac{U_\theta}{\sigma_1} = \frac{R}{2} \sin(\alpha) + \frac{w}{2}; \quad (5.15c)$$

$$\frac{U_\phi}{\sigma_1} = \frac{x}{2} - \frac{R}{2} \cos(\alpha). \quad (5.15d)$$

The corresponding Jacobian, J_{QU} (to be distinguished from the Jacobian above), is

$$|\det(J_{QU})| = \frac{R}{4\sigma_1^4}. \quad (5.16)$$

Therefore,

$$dQ_\theta dQ_\phi dU_\theta dU_\phi = \frac{R}{4\sigma_1^4} dR dx dw d\alpha \quad (5.17)$$

Applying the change of variables within the integral in equation (5.10),

$$N_{\text{np}} = \frac{\sigma_1^2}{4(2\pi)^3 \sigma_0^2} \int \exp\left(-\frac{x^2 + w^2 + R^2}{2}\right) |x^2 + w^2 - R^2| dR dx dw d\alpha. \quad (5.18)$$

Integration over α is a factor of 2π , so

$$N_{\text{np}} = \frac{\sigma_1^2}{4(2\pi)^2 \sigma_0^2} \int \exp\left(-\frac{x^2 + w^2 + R^2}{2}\right) |x^2 + w^2 - R^2| dR dx dw. \quad (5.19)$$

The integral can be almost separated by a further change of variables, defining $b = R^2 - w^2$,

$$N_{\text{np}} = \frac{\sigma_1^2}{8(2\pi)^2 \sigma_0^2} \int_{-\infty}^{\infty} e^{-x^2/2} dx \int_{-\infty}^{\infty} e^{-w^2} dw \int_{-w^2}^{\infty} |x^2 - b| e^{-b/2} db. \quad (5.20)$$

b has a finite lower bound by construction. The number density of non-polarized points has been recast into integration over the three-dimensional x, w, b space. In terms of these coordinates, the trace and determinant of the original Jacobian J are

$$\text{Tr}(J) = x \quad (5.21)$$

and

$$\det(J) = \frac{1}{4}(x^2 + w^2 - R^2) = \frac{1}{4}(x^2 - b). \quad (5.22)$$

The eigenvalues, expressed before in terms of the trace and determinant in equation (5.13), thus take the simple form

$$\lambda_{\pm} = \frac{1}{2}(x \pm \sqrt{b}). \quad (5.23)$$

Also, the classifications of non-polarized points can be specified as:

$$\begin{aligned} -w^2 < b < 0 &: \quad \text{focus;} \\ 0 < b < x^2 &: \quad \text{node;} \\ x^2 < b < \infty &: \quad \text{saddle.} \end{aligned}$$

Therefore, the number density of each type can be computed by restricting the bounds of the innermost integral in equation (5.20). When the bounds are specified, all the integrations are elementary. The results are

$$N_f = \frac{\sqrt{2}}{16\pi r_c^2}, \quad N_k = \frac{2 - \sqrt{2}}{16\pi r_c^2}, \quad N_s = \frac{1}{8\pi r_c^2}, \quad (5.24)$$

which are all multiples of $1/r_c^2 = \sigma_1^2/\sigma_0^2$. These sum to the total density of non-polarized points,

$$N_{\text{total}} = N_f + N_k + N_s = \frac{1}{4\pi r_c^2}, \quad (5.25)$$

from which it is clear that the number of non-polarized points on the full sky is given by the simple expression $1/r_c^2$.

The correlation radius r_c depends on the power spectrum, which dependence is inherited by the densities N_f , N_k , and N_s . However, the ratios of the densities are independent of r_c :

$$\frac{N_f}{N_k} = \sqrt{2} + 1, \quad \frac{N_f}{N_s} = \frac{\sqrt{2}}{2}. \quad (5.26)$$

These ratios are true constants depending only on the Gaussian character of Q and U . This is the basis for the Gaussianity tests that follow.

F-statistics of the correlation length

At this point, it should be restated that, thus far, we have dealt with expectation values. A sky map, or any subset thereof, is a finite sample in which the empirical numbers of non-polarized points and their ratios are allowed to vary. It is not possible to predict the variance directly from equation (5.26). Instead, we should return to the individual

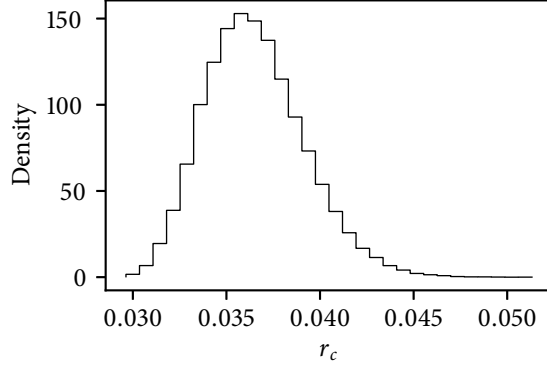


Figure 5.2: F -distribution fit to simulations of r_c in a Gaussian model. The shape parameters of the F -distribution will depend on the specific power spectrum of the CMB sky; given these parameters, the allowed variation in r_c , and therefore the number density N_{np} , is specified by the F -distribution.

expressions found for the number densities in equation (5.24). r_c is a ratio of chi-squared variables, which follows a beta distribution of the second kind:

$$\mathcal{P}(r_c) = \frac{r_c^{\alpha-1}(1+r_c)^{-\alpha-\beta}}{\int_0^1 t^{\alpha-1}(1-t)^{\beta-1} dt}. \quad (5.27)$$

With suitable rescalings of Q and U , which can be subsumed into a change of units, the beta distribution can be reduced into an F -distribution:

$$\mathcal{P}(r_c) = \frac{(\alpha/\beta)^\alpha}{\int_0^1 t^{\alpha-1}(1-t)^{\beta-1} dt} r_c^{\alpha-1} \left(1 + \frac{\alpha}{\beta} r_c\right)^{-\alpha-\beta}. \quad (5.28)$$

If Q and U are allowed to have nonzero means, the noncentral F -distribution applies, which is not fundamentally different except for having a more complicated formula. The parameters α and β depend on the number of degrees of freedom of the chi-squared distributions—which in practice depend on the power spectrum and the smoothing angle. Rather than attempting to work out the details of this dependence, it is simpler to consider α and β as power-spectrum-dependent parameters which can be empirically fitted if necessary. From the distribution of r_c , the distribution of the number densities follows immediately.

Polarization angles near non-polarized points

A final aspect of the Gaussian theory of non-polarized points is the local behavior of the polarization angle. Adopting polar coordinates in the tangent space,

$$d\theta = dr \cos(\bar{\omega}), \quad d\phi = dr \sin(\bar{\omega}), \quad (5.29)$$

the polarization angle ψ obeys

$$\frac{d}{d\bar{\omega}} \tan(2\psi) = \frac{\det(J)}{Q^2}. \quad (5.30)$$

Therefore the sign of the determinant determines whether the polarization angle increases in a clockwise or anticlockwise direction around the point. In a clockwise trajectory, ψ decreases if the point is a saddle and increases if it is a knot or focus. This is illustrated in figure 5.1.

5.2 LENSING AND THE E/B MODES

The E and B modes, decomposed in the space of the Stokes parameters as explained in chapter 2, are subject to the same Gaussian theory when the $Q_{E/B}$ and $U_{E/B}$ maps are Gaussian. However, in general the correlation length can vary between the unseparated and the E/B modes. This variation is constrained by equation (2.4). The Q/U variance, σ_0^2 , obeys

$$\sigma_0^2 = \langle (Q_E + Q_B)^2 \rangle = \langle (U_E^2 + U_B^2) \rangle. \quad (5.31)$$

Therefore,

$$2\sigma_0^2 = \langle (Q_E + Q_B)^2 + (U_E + U_B)^2 \rangle \quad (5.32a)$$

$$= \langle Q_E^2 + Q_B^2 + U_E^2 + U_B^2 \rangle \quad (5.32b)$$

$$= \Delta_E^2 + \Delta_B^2, \quad (5.32c)$$

where $\Delta_E^2 = \langle Q_E^2 \rangle + \langle U_E^2 \rangle$ and $\Delta_B^2 = \langle Q_B^2 \rangle + \langle U_B^2 \rangle$. These equations assume zero E–B correlation. There is no expectation that $\Delta_E = \Delta_B$. However, within the same equal-variance model assumed in section 5.1, we can assume that $\langle Q_E^2 \rangle = \langle U_E^2 \rangle = \Delta_E^2/2$, and similarly for the B mode. For the derivatives,

$$\sigma_1^2 = 2\text{var}(Q'_E + Q'_B) = 2\text{var}(U'_E + U'_B) \quad (5.33a)$$

$$= \text{var}(Q'_E + Q'_B) + \text{var}(U'_E + U'_B) \quad (5.33b)$$

$$= \text{var}(Q'_E) + \text{var}(U'_E) + \text{var}(Q'_B) + \text{var}(U'_B) \quad (5.33c)$$

$$= \frac{\gamma_E^2 + \gamma_B^2}{2}, \quad (5.33d)$$

where $\gamma_E^2 = 4\text{var}(Q'_E) = 4\text{var}(U'_E)$ and $\gamma_B^2 = 4\text{var}(Q'_B) = 4\text{var}(U'_B)$. The same equal-variance and zero-covariance assumptions are in use, and, in general, γ_E and γ_B are different from each other.

The correlation lengths of the E and B modes are

$$N_{\text{np}}^{E/B} = \frac{1}{(r_c^{E/B})^2} = \frac{\gamma_{E/B}^2/2}{\Delta_{E/B}^2/2} = \frac{\gamma_{E/B}^2}{\Delta_{E/B}^2}. \quad (5.34)$$

The total number of non-polarized points can be decomposed as

$$N_{\text{np}} = \frac{1}{r_c^2} = \frac{\sigma_1^2}{\sigma_0^2} = \frac{\gamma_E^2 + \gamma_B^2}{\Delta_E^2 + \Delta_B^2} \quad (5.35a)$$

$$\approx N_{\text{np}}^E \left(1 + \frac{\gamma_B^2}{\gamma_E^2} - \frac{\Delta_B^2}{\Delta_E^2} \right) \quad (5.35b)$$

$$= N_{\text{np}}^E \left(1 - \frac{\Delta_B^2}{\Delta_E^2} \left(1 - \frac{N_{\text{np}}^B}{N_{\text{np}}^E} \right) \right). \quad (5.35c)$$

Thus, if $N_{\text{np}}^B < N_{\text{np}}^E$, then the E mode has more non-polarized points than the total unseparated map. This is observed in practice (figure 5.3). The excess grows with increasing B mode, i.e., with increasing Δ_B^2 .

For the primordial B mode signal, both γ_B^2 and Δ_B^2 are proportional to the tensor-to-scalar ratio r . Therefore the total number of non-polarized points in the primordial B mode does not depend on r . However, this proportionality is broken in the presence of weak lensing of the E mode, which induces a B mode signal unrelated to r . This raises the possibility of lensing detection based on simple total density estimators.

The dependence of N_{np}^B on r , including the effect of gravitational lensing, is nontrivial. Assuming that the smoothing scale of the map is greater than the correlation radius of the cosmological signal, then the variances can be represented as

$$\Delta_B^2 \approx \Delta_{B,\text{cmb}}^2(r) + \Delta_{B,\text{lens}}^2 \quad (5.36)$$

and

$$\gamma_B^2 \approx \gamma_{B,\text{cmb}}^2(r) + \gamma_{B,\text{lens}}^2. \quad (5.37)$$

The first terms are the variances from the primordial CMB, which are functions of the tensor-to-scalar ratio r . The second terms are due to lensing, which are independent of r .

The dependence of the primordial variances on r is linear. Therefore they can be written

$$\Delta_B^2(r) = \frac{r}{r_*} \Delta_B^2(r_*) \quad (5.38)$$

and

$$\gamma_B^2(r) = \frac{r}{r_*} \gamma_B^2(r_*), \quad (5.39)$$

where r_* is an arbitrary normalization value. Then the total number of non-polarized points is

$$N_{\text{np}}^B(r) = \frac{\frac{r}{r_*} \gamma_B^2(r_*) + \gamma_{B,\text{lens}}^2}{\frac{r}{r_*} \Delta_B^2(r_*) + \Delta_{B,\text{lens}}^2}. \quad (5.40)$$

The asymptotics are easy to calculate. The small- r limit (lensing dominates) is

$$\lim_{r \rightarrow 0} N_{\text{np}}^B(r) = \frac{\gamma_{B,\text{lens}}^2}{\Delta_{B,\text{lens}}^2}, \quad (5.41)$$

and the large- r limit is

$$\lim_{r \rightarrow \infty} N_{\text{np}}^B(r) = \frac{\gamma_{B,\text{lens}}^2(r_*)}{\Delta_{B,\text{lens}}^2(r_*)}, \quad (5.42)$$

which is equal to $N_{\text{np,cmb}}^B$ for any r_* .

In the large- r limit, $N_{\text{np}}^B(r)$ can be extended to linear order:

$$\frac{N_{\text{np}}^B(r)}{N_{\text{np,cmb}}^B} \approx 1 - \frac{\Delta_{B,\text{lens}}^2}{\Delta_B^2(r_*)} \left(\frac{r_*}{r} \right) \left(1 - \frac{N_{\text{np,lens}}^B}{N_{\text{np,cmb}}^B} \right). \quad (5.43)$$

In the other limit

$$\frac{N_{\text{np}}^B(r)}{N_{\text{np,cmb}}^B} \approx 1 - \frac{\Delta_B^2(r_*)}{\Delta_{B,\text{lens}}^2} \left(\frac{r}{r_*} \right) \left(1 - \frac{N_{\text{np,cmb}}^B}{N_{\text{np,lens}}^B} \right). \quad (5.44)$$

These results are investigated in simulated CMB maps generated using CAMB, in which the tensor-to-scalar ratio and the lensing potential can be adjusted. The derived effects will only be visible when the maps are at a resolution comparable to the lensing scale. Figure 5.3 shows results at a smoothing scale of 0.5° , where the sensitivity to lensing in the B mode is very strongly visible.

5.3 NON-POLARIZED POINT ANALYSIS IN THE 2018 PLANCK MAPS

The goal is to use the non-polarized points, and in particular the ratios N_f/N_s and N_k/N_s , as statistical estimators. As we have seen above, these ratios have specific expectation values when the data are Gaussian. Departures from Gaussianity are expected to perturb the ratios.

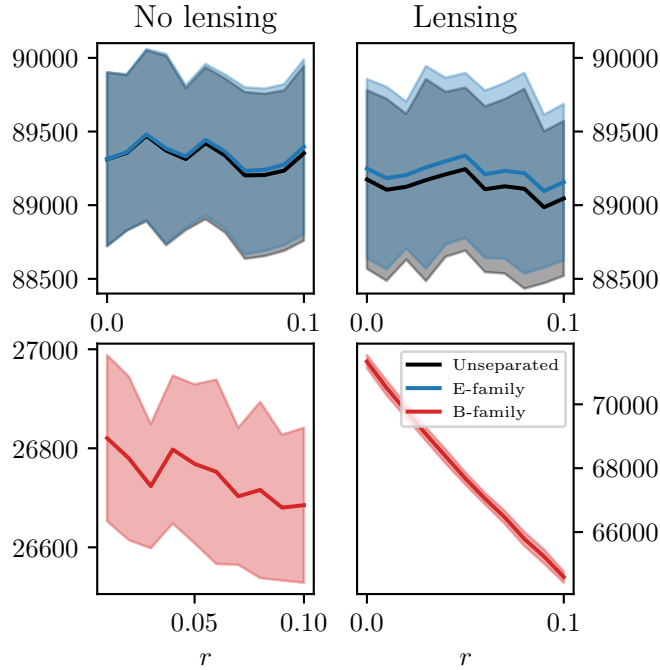


Figure 5.3: Total numbers of non-polarized points, for the E and B modes separately and the total unseparated signal, under conditions of lensing and no lensing. The shaded region shows the 68% confidence region over the simulations, which were generated using CAMB [169]. The simulations validate the results found in the preceding theoretical section. Except when $r = 0$ in the no lensing simulations, there are slightly more E non-polarized points than the total unseparated signal. The stronger the B mode is, the bigger the E excess will be.

Detection of non-polarized points

In the abstract theory, where Q and U are continuous real-valued functions on the sphere, the existence of points where simultaneously $Q = 0$ and $U = 0$ is a trivial matter, which is easily handled by the intermediate value theorem. This is essentially the argument at the beginning of this chapter. But the simplicity of this argument disguises some genuine difficulties of locating non-polarized points in the practical reality, where Q and U are pixelized sky maps. Immediately, we face the challenge that there is not expected to be any pixel in which either $Q = 0$ or $U = 0$ because the pixel values are samples.

The main computational strategies are based on simultaneous root-finding in the Q and

U maps, or minimization of the polarization intensity map ($P = \sqrt{Q^2 + U^2}$). Combining these strategies, the following necessary and sufficient conditions are proposed for root-finding in the CMB polarization.

A particular pixel \hat{n}_0 is a non-polarized point if:

1. The Stokes parameters at \hat{n}_0 satisfy $|Q(\hat{n}_0)| < \epsilon$ and $|U(\hat{n}_0)| < \epsilon$ for some small threshold intensity ϵ .¹
2. \hat{n}_0 is a local minimum of the polarization intensity with respect to all neighbouring pixels, i.e. $P(\hat{n}_0) < P(\hat{n}_i)$ for all \hat{n}_i adjacent to \hat{n}_0 .
3. Within the connected sub- ϵ region containing \hat{n}_0 , there are pixels taking both positive and negative values of Q and U .
4. There are no other pixels that meet conditions 1–3 with a smaller polarization intensity within an angular distance α_{\max} of \hat{n}_0 .

The parameters ϵ and α_{\max} are not necessarily fixed by the criteria. In practice, some heuristic definitions of these parameters enable a search. In [21], these parameters are determined as follows. It was observed above that the total number of non-polarized points expected on the full sky is $1/r_c^2 \cdot \epsilon$ and α_{\max} can be adjusted until the total number of points detected is equal to $1/r_c^2$, rescaled suitably for the partial sky. Acting in this way removes information about the total number of non-polarized points while retaining information about their ratios only: in essence, it is assumed that the total number is exactly the Gaussian expectation, and then the corresponding ratios are found. The meaning has a slight fuzziness, but in practice, provided that the data resolution enables a large number of non-polarized points to be extracted, the ratios are rarely strongly sensitive to the parameters ϵ and α_{\max} .

Analysis in subareas

The ratios N_f/N_s and N_k/N_s can be computed within any given region of the sky. Assuming isotropy, their expectation value is the same in any subarea, although smaller subareas will have fewer total counts of non-polarized points and corresponding greater expected variances of the empirical ratios.

Statistical analysis on subareas has two possible advantages. First, it is sensitive to local anomalies in the non-polarized points which may be outweighed in the full-sky analysis. Second, it permits the data to be studied with different variances, depending on the size of the subareas.

A simple scheme for subarea analysis is based on the nested nature of HEALPix. Low resolution “mother pixels”, corresponding to the HEALPix pixels from a small N_{side} , are

¹Alternatively, the polarization intensity at \hat{n}_0 satisfies $P(\hat{n}_0) < \epsilon$ for some small threshold intensity ϵ , which is statistically equivalent, but in practice will result in a slightly a different sample of points.

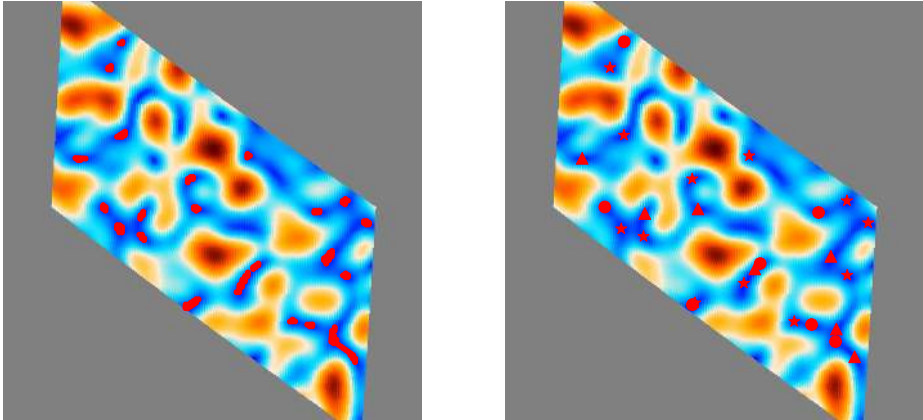


Figure 5.4: Illustration of detection of non-polarized points in a single $N_{\text{side}} = 16$ subpixel. The left panel shows the red dots resulting from the initial descent algorithm. The right panel shows the final NPPs that remained after filtering for α_{max} . The nearly adjacent streams of NPPs, which are not distinguished in the pixel domain, must be removed in this way. Focuses are drawn marked by circles, knots by triangles, and saddles by stars.

used as the subareas for analysis. These subareas automatically cover the entire sky, and each subarea has the same size. The analysis in this chapter, based on [21], uses $N_{\text{side}} = 8$ for the mother pixel resolution. The full sky is therefore divided into 768 subareas.

Corrupted sky regions are easily excluded from the subarea analysis by masking at the mother pixel resolution. A simple approach, used here, is downgrading the *Planck* polarization confidence masks, which are provided at the data resolution of $N_{\text{side}} = 2048$, using an area-preserving method. Area-preserving mask downgrading does not retain the original statistical definition of the mask confidence, but it is a compromise on a continuum of more conservative and less conservative choices.

Comparing ratio distributions

At last, we can look at the ratios in the 2018 *Planck* maps. All maps are smoothed with a Gaussian filter having a full width at half maximum of 0.5° , and divided into subareas corresponding to $N_{\text{side}} = 8$ as described above and illustrated in figure 5.6. From the ratios evaluated in each subpixel, a distribution function can be calculated. This is shown in figure 5.7.

The histograms are calculated with a relatively small number of bins. In order to reduce noise, the conservative Sturge's formula is used, giving $\log_2(N) + 1$ bins, which is 9 for the

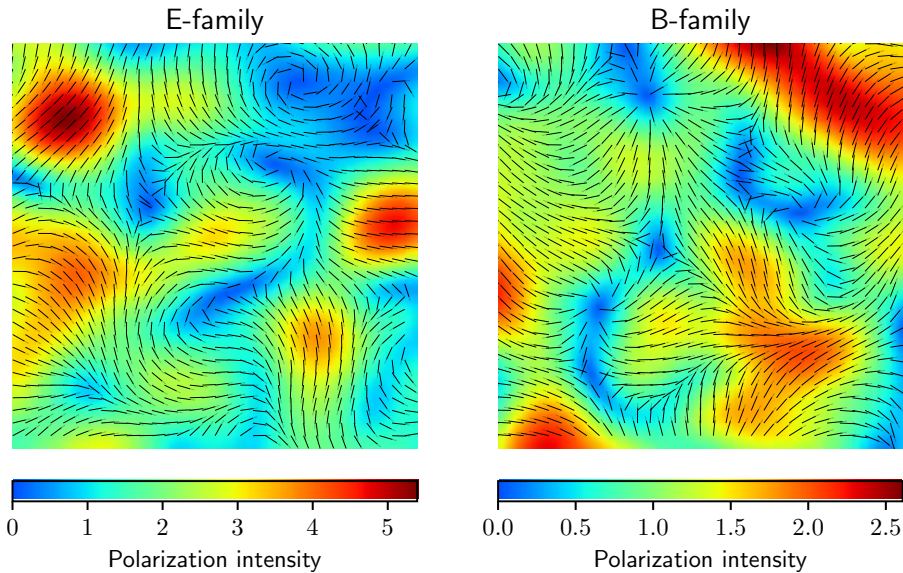


Figure 5.5: Polarization intensities and polarization angles (shown as black dashes) in the E and B families in a small zone of the sky. Several non-polarized points are visible.

dataset.¹

To compare the distribution functions from the *Planck* maps with a background Gaussian expectation, the Kullback–Leibler entropy is used. The definition of the Kullback–Leibler entropy between a sample distribution P and a background distribution Q is

$$\Theta_{KL}(P|Q) = \sum_i P_i \log\left(\frac{P_i}{Q_i}\right), \quad (5.45)$$

where the sum is taken over all bins i , and P_i and Q_i are the densities in each bin. Smaller values of Θ_{KL} correspond to better consensus between the two distribution functions.

Any bin for which $Q_i = 0$ contributes an infinity to the Kullback–Leibler entropy. There are several fixes for this problem, including doping bins by adding an extra data point, minimally smoothing the distributions, or excluding bins with zero points from the analysis. All methods gave similar results, and generally, this is not expected to be a problem because there are very few bins that have zeros. In the results below, zero bins are excluded.

To produce a p value from the Kullback–Leibler entropy, the KL-statistics between

¹ $\log_2(768) + 1 \approx 10.5$, but some subpixels are masked in this analysis. See figure 5.6.

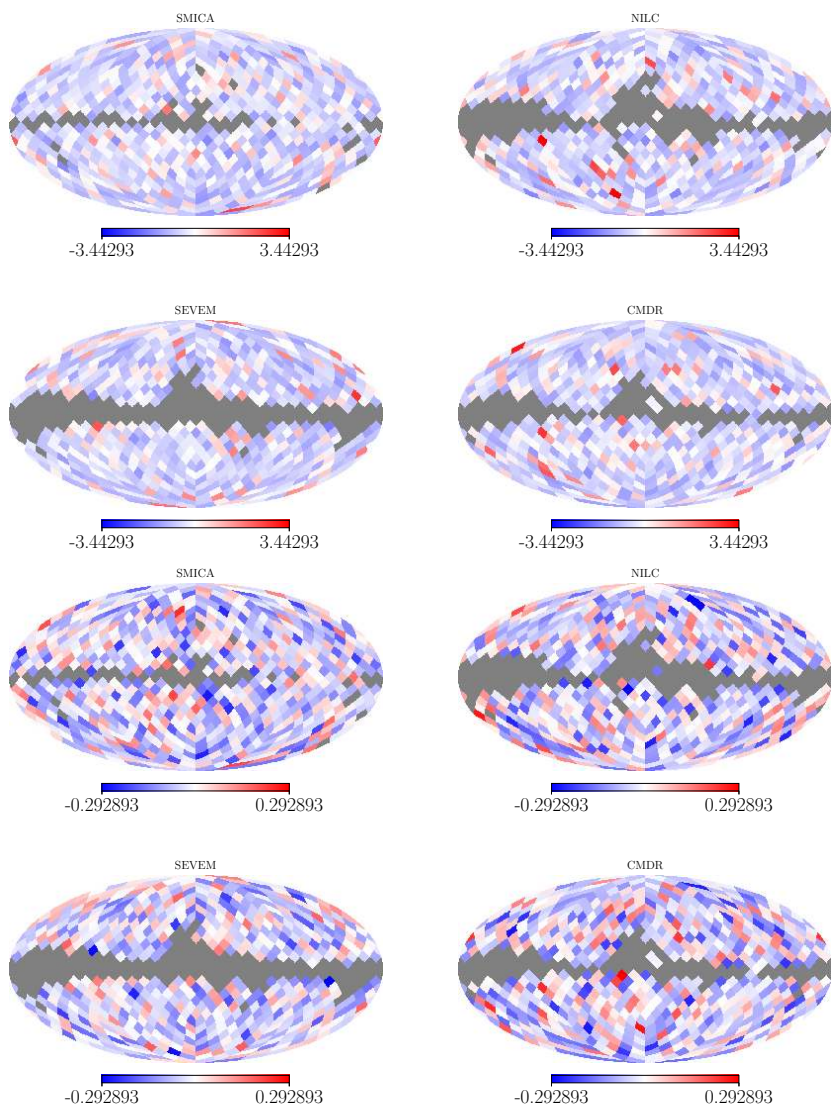


Figure 5.6: Absolute ratio differences in the $N_{\text{side}} = 8$ subareas. The upper four panels show N_f/N_k and the lower four panels show N_f/N_s . The differences are calculated by subtraction of the theoretical ratios $N_f/N_k = \sqrt{2} + 1$ and $N_f/N_s = \sqrt{2}/2$. Downgraded confidence masks are used to exclude some highly corrupted subareas from the analysis.

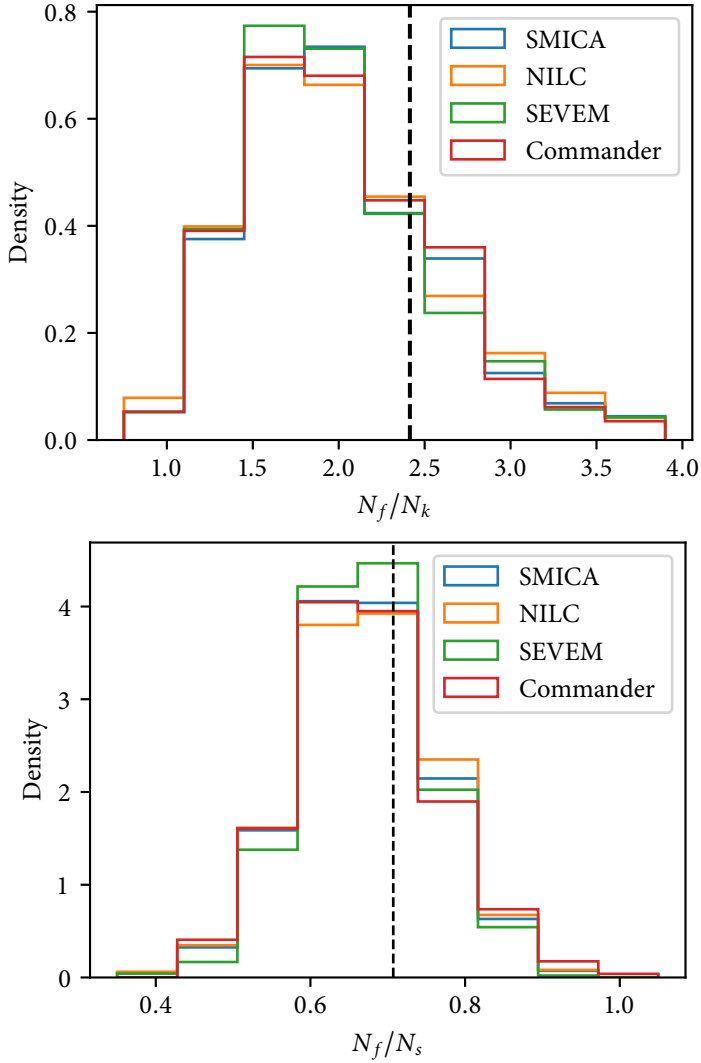


Figure 5.7: The upper panel shows the distribution function of N_f/N_k over the $N_{\text{side}} = 8$ subregions of the four *Planck* CMB maps. The lower panel shows the same of N_f/N_s .

the *Planck* maps and background Gaussian simulations are compared to an ensemble of KL-statistics generated by comparing different Gaussian simulations to each other. A total of 46 unique Gaussian simulations are used, yielding 1035 unique pairs in the background

distribution. This is not enough to overcome entirely the issues of sampling uncertainty, however, it is enough to give reasonably stable results and to illustrate the performance of the method.

An alternative estimator is the Kolmogorov–Smirnov test. The Kolmogorov–Smirnov estimator is the maximum distance between the cumulative distribution functions of two samples, which, under relatively weak assumptions, is distributed according to the Kolmogorov distribution depend on the number of samples (but not the shape of the underlying distribution functions). The Kolmogorov–Smirnov test therefore provides a low-assumption p value, and, unlike the Kullback–Leibler entropy, it does not depend on the binning. A possible source of trouble, however, is that the ratios are not, strictly speaking, continuous, which violates one of the assumptions underlying the validity of the Kolmogorov distribution. It is hoped that the ratios are close enough to continuous that this is a small source of error.

Results and p values

Tables 5.1 and 5.2 summarize the statistics of the ratio distributions, the estimators, and p values calculated according to the methodology detailed above. According to the Kullback–Leibler estimator, the strongest discrepancies are seen in Commander and NILC, with p values of 0.07 and 0.15 respectively. The Kolmogorov–Smirnov test points to more peculiarities, especially in SEVEM, in which Gaussian behavior of the ratios is rejected with $p < 0.01$. The two estimators are complementary, with the KS test being more sensitive to local deviations and deviations in the tails compared to the KL entropy.

None of the p values are highly significant, although the modest significance of some of the ratios (especially in SEVEM) could merit future investigation. The p values, being calculated as percentiles in empirical histograms, are themselves uncertain and could be unstable when too few simulations are in use. This does not seem to be the case here, although some of the variations in the p values are remarkable.

A final comment is made about the interpretation of the results. The theoretical number densities of the different types of non-polarized points implied by Gaussianity have not been tested. Instead, we have tested two things: the total number density of non-polarized points and the ratios. Recall that the procedure for identification of the non-polarized points is effectively imposing r_c through the α_{\max} and ϵ parameters. Therefore it is only the two ratios themselves, not the underlying three number densities, which are probed. Because it is impossible to detect exact zeros in pixelized data, this limitation is inevitable in this kind of analysis; however, tests show that the choices made here result in a non-polarized point search algorithm that is reasonably stable and well-motivated.

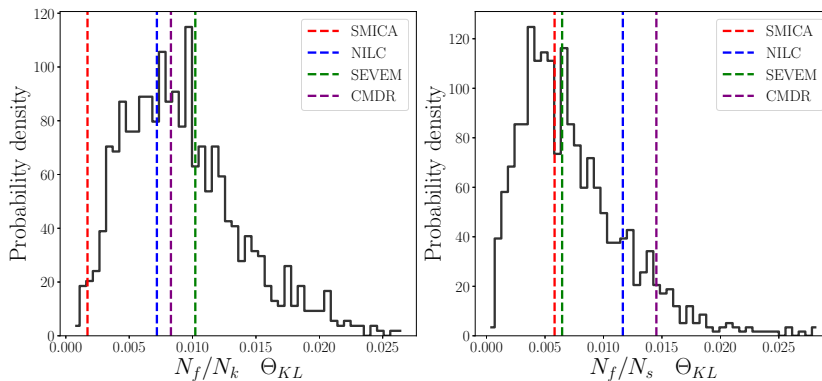


Figure 5.8: Distribution functions of the Kullback–Leibler divergence, Θ_{KL} , calculated from between the ratio distributions of Gaussian simulations, compared to the specific Θ_{KL} values between the *Planck* 2018 CMB maps and the averaged background Gaussian. From these plots, the p values in table 5.2 are calculated.

Map name	$\text{ex}(f/k)$	$\text{stdev}(f/k)$	$\text{ex}(f/s)$	$\text{stdev}(f/s)$
Gaussian	2.0349	0.3240	0.6763	0.0071
SMICA	2.0149	0.3357	0.6716	0.0076
NILC	2.0143	0.3756	0.6719	0.0084
SEVEM	1.9934	0.3377	0.6702	0.0067
CMDR	2.0073	0.3190	0.6712	0.0087

Table 5.1: The statistics of the ratio distributions for the CMB and Gaussian simulations. For the two ratios, N_f/N_k and N_f/N_s , calculated in subareas as discussed in the text, the observed means (ex) and standard deviations (stdev) are shown.

KL	f/k KL-entropy	f/k p value	f/s KL-entropy	f/s p value
SMICA	0.0017	0.9884	0.0058	0.5044
NILC	0.0072	0.6135	0.0117	0.1560
CMDR	0.0083	0.5130	0.0145	0.0713
SEVEM	0.0102	0.3324	0.0065	0.4661
KS	f/k KS-score	f/k p value	f/s KS-score	f/s p value
SMICA	0.0400	0.2076	0.0459	0.1017
NILC	0.0380	0.3248	0.0466	0.1317
CMDR	0.0424	0.1859	0.0506	0.0686
SEVEM	0.0662	0.0095	0.0518	0.0747

Table 5.2: Kullback–Leibler and Kolmogorov–Smirnov test results for all the maps. The p values are the probability of finding a statistic at least that large.

6 LARGE SCALE ANOMALIES IN TEMPERATURE AND POLARIZATION

Despite the excellent overall agreement of the recent observations of the CMB with standard cosmological theory, tests of isotropy and Gaussianity at large angular scales have uncovered several deviations with noticeable, but not undeniable, significance. These features are termed *anomalies*. They include:

- The parity asymmetry, the excess of odd-multipole power and/or deficit of even-multipole power. This was detected in the power spectrum of the WMAP and *Planck* data [170–173]. Perhaps a special case of the parity asymmetry is the unusually low amplitude of the quadrupole ($\ell = 2$), although this might also deserve treatment as a separate anomaly.
- The power asymmetry, the excess of power in the southern hemisphere compared to the northern, or a generic dipole asymmetry directed approximately orthogonal to the ecliptic. This effect was first detected in the first-year WMAP data [174] and has been investigated in the subsequent WMAP and *Planck* releases [175–177]. In [178], a simple model of dipole modulation, accompanied by a proposed physical explanation, is suggested:

$$T(\hat{n})_{\text{modulated}} = (1 + \vec{w} \cdot \hat{n})T(\hat{n})_{\text{unmodulated}}. \quad (6.1)$$

The direction and norm of the vector \vec{w} parametrize the dipole modulation model. In normal processing of microwave data, the entire dipole ($\ell = 1$) is attributed to the redshift of the CMB caused by the motion of the observatory in the CMB rest frame.

- The quadrupole–octupole alignment, which entails several peculiar aspects of the orientation of the $\ell = 2$ and $\ell = 3$ multipoles. The planarity of the octupole ($\ell = 3$) is greater than expected, and its direction is aligned with the direction of the quadrupole, which is planar by nature. The mutual alignment of the quadrupole and octupole is also similar to the direction of the kinematic dipole and the ecliptic plane. These features were observed in the WMAP data [179, 180] and persist in the *Planck* data [181, 182].

Other important anomalies include the lack of power on large angular scales [183, 184] and the cold spot [185, 186].

The possible origins can be classified into four kinds: random coincidence, systematic errors, foreground contamination, and cosmological. The last of these has attracted the most attention and spawned theory papers that attempt to modify the cosmological theory to explain the anomalies [178, 187, 188]. However, the other explanations cannot be overlooked. Systematic errors and the residuals of foreground cleaning are well-known to pervade the data, although the overall general agreement between the WMAP and *Planck* analyses of the anomalies disfavors an obvious systematic explanation. It has been demonstrated that not only Galactic foregrounds, but also Solar System foregrounds and Kuiper Belt objects, could influence the power and parity asymmetries [189]. The significance of these anomalies has been questioned, especially in consideration of cosmic variance, and it has been argued that it is unimpressive. The position of the *Planck* collaboration on the anomalies is summarized in [66]:

“The existence of these features is uncontested, but, given the modest significances at which they deviate from the standard Λ CDM cosmological model, and the a posteriori nature of their detection, the extent to which they provide evidence for a violation of isotropy in the CMB remains unclear. It is plausible that they are indeed simply statistical fluctuations. Nevertheless, if any one of them has a physical origin, it would be extremely important, and hence further investigation is certainly worthwhile.”

The large-scale anomalies have been widely studied using different estimators in the literature, especially in the WMAP and *Planck* data (some reviews include [190, 191]). It has been shown that the significance of the anomalies has considerable dependence on the mask [192], and the joint estimation of their significance, and the correlation and independence of the anomalies with each other, as well as the possibilities and difficulties of a common explanation, have also been widely investigated [193–199]. The possibility of using the polarization data together with the temperature data for joint analysis of the anomalies in both datasets has also been considered [200–202].

The purpose of this chapter is some new analysis of the anomalies in the latest *Planck* data, especially the parity asymmetry, with the continued spirit of attempting to use map-domain methods and estimators. The asymmetry between the even and odd modes can be localized by separating them, returning to the map domain, and comparing their local power. In this way, it is shown that the parity asymmetry is not distributed evenly across the sky, but is particularly clustered in several small regions. From here the interaction of the parity asymmetry with masking, and with the other anomalies, especially the octupole–quadrupole alignment, can be investigated.

In map-domain analysis of the anomalies, the multipole range is controlled by the smoothing angle of the map. Most of the results in this chapter are based on maps smoothed at 5° , corresponding to approximately all multipoles $\ell \lesssim 20$; in several places the smoothing

angle is reduced to 2.5° , corresponding to approximately $\ell \lesssim 40$. This correspondence is only approximate. Furthermore, the *Planck* SMICA map is chosen for most of the illustrations, although the results are not strongly dependent on the choice of component separation method. The work is contained in recent publications [22, 23].

6.1 POINT PARITY ASYMMETRY

The investigation of the parity asymmetry naturally begins in the power spectrum. Several power spectrum estimators have been proposed. In [171, 172] is introduced the estimator

$$g(\ell_{\max}) = \frac{\sum_{\ell=2}^{\ell_{\max}} \ell(\ell+1)C_\ell^+}{\sum_{\ell=2}^{\ell_{\max}} \ell(\ell+1)C_\ell^-}, \quad (6.2)$$

where C_ℓ^\pm is the power spectrum of even/odd modes only, i.e.

$$C_\ell^+ = C_\ell \cos^2(\pi\ell); \quad (6.3a)$$

$$C_\ell^- = C_\ell \sin^2(\pi\ell). \quad (6.3b)$$

This estimator is slightly amended in the *Planck Isotropy & Statistics* papers [66, 203] to explicitly correct for the unequal number of multipoles in each sum for odd ℓ_{\max} :

$$R(\ell_{\max}) = \frac{\frac{1}{\ell_{\text{tot}}^+} \sum_{\ell=2}^{\ell_{\max}} \ell(\ell+1)C_\ell^+}{\frac{1}{\ell_{\text{tot}}^-} \sum_{\ell=2}^{\ell_{\max}} \ell(\ell+1)C_\ell^-}, \quad (6.4)$$

The *Planck* result for $R(\ell_{\max})$ from [66] is plotted in figure 6.1. Apart from showing a preference for odd multipoles ($g(\ell_{\max}) < 1$ and $R(\ell_{\max}) < 1$ consistently), the estimator is not informative without examination of the variance. The strongest departure is found around $\ell_{\max} \approx 25$ at around the 1% level.¹ This is broadly consistent with the results from the 2015 maps [204], as well as similar analyses in the *Planck* studies [203].

It is clear from figure 6.1 that the expectation value of $R(\ell_{\max})$ is not 1, although it does seem to converge to 1 in the $\ell_{\max} \rightarrow \infty$ limit. This may be surprising, but consider that the leading-order quadrupole term ($\ell = 2$) in an approximately quadratic power spectrum ($C_\ell \approx 1/\ell(\ell+1)$) will give a strong overall even-parity preference. This leading-order preference is related to the decay of the power spectrum and not compensated by the ℓ_{tot}^\pm

¹But the “look-elsewhere” effect applies to estimators of this kind. Nevertheless, near-1% significance is observed in a fairly wide range of ℓ_{\max} .

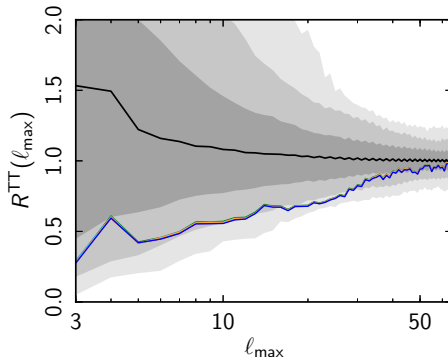


Figure 6.1: $R(\ell_{\max})$ for the *Planck* component separation maps up to $\ell_{\max} \approx 50$. A persistent odd-parity preference is visible. Commander, NILC, SEVEM, and SMICA are plotted in red, orange, green, and blue respectively; the differences between the maps are minor. The grey background shows the 1, 2, and 3σ ranges of the estimator for isotropic simulations. Figure taken from [66].

factors in $R(\ell_{\max})$, but it is diluted when enough multipoles are counted. There is therefore some subtlety in assigning even/odd-parity preference: comparison of the estimators with 1 is biased by the inherent even-parity preference of zero-mean, zero-dipole sky data. Also noteworthy in the low- ℓ_{\max} region is the very large variance of the estimators.

Pixel-domain estimation of parity asymmetry

The study of the parity asymmetry in the power spectrum domain using the $g(\ell_{\max})$ and $R(\ell_{\max})$ estimators above indicates an odd-parity preference in the first ≈ 40 multipoles. From this analysis, it is unclear if this asymmetry is localized or distributed in the map domain, because the estimators involve sky averaging, implicitly through the power spectrum. To investigate this question, a map domain estimator is proposed, which is the product of antipodal temperatures, as follows.

We define the symmetric and asymmetric combinations of the CMB temperature $T(\hat{n})$ and its antipode, $T(-\hat{n})$:

$$S(\hat{n}) = \frac{T(\hat{n}) + T(-\hat{n})}{2}; \quad (6.5a)$$

$$A(\hat{n}) = \frac{T(\hat{n}) - T(-\hat{n})}{2}. \quad (6.5b)$$

The two parts sum to the original input: $T(\hat{n}) = S(\hat{n}) + A(\hat{n})$. The desirable property of

$S(\hat{n})$ and $A(\hat{n})$ is that they decompose into only the even and odd multipoles respectively:

$$S(\hat{n}) = \sum_{\ell=2}^{\ell_{\max}} \sum_{m=-\ell}^{\ell} a_{\ell m} Y_{\ell m}(\hat{n}) \cos^2(\pi\ell/2); \quad (6.6a)$$

$$S(\hat{n}) = \sum_{\ell=2}^{\ell_{\max}} \sum_{m=-\ell}^{\ell} a_{\ell m} Y_{\ell m}(\hat{n}) \sin^2(\pi\ell/2). \quad (6.6b)$$

We can characterize the asymmetry between the even and odd multipoles by the difference in their power, which is

$$Z(\hat{n}) = S^2(\hat{n}) - A^2(\hat{n}) = T(\hat{n})T(-\hat{n}). \quad (6.7)$$

When $Z(\hat{n}) > 0$, then the \hat{n} is correlated with $-\hat{n}$, and the symmetric (even ℓ) modes exceed the asymmetric (odd ℓ) modes at that point. When $Z(\hat{n}) < 0$, the situation is reversed, and \hat{n} is anti-correlated with $-\hat{n}$, and the asymmetric part is greater than the symmetric part.

The expectation value of the full-sky mean of $Z(\hat{n})$ is computed as follows:

$$\langle Z(\hat{n}) \rangle = \int Z(\hat{n}) d\hat{n} = \int T(\hat{n})T(-\hat{n}) d\hat{n} \quad (6.8a)$$

$$= \sum_{\ell, m} \sum_{\ell', m'} a_{\ell m} a_{\ell' m'}^* \int Y_{\ell m}(\hat{n}) Y_{\ell' m'}(-\hat{n})^* d\hat{n} \quad (6.8b)$$

$$= \sum_{\ell, m} \sum_{\ell', m'} a_{\ell m} a_{\ell' m'}^* (-1)^{\ell'} \int Y_{\ell m}(\hat{n}) Y_{\ell' m'}(\hat{n})^* d\hat{n} \quad (6.8c)$$

$$= \sum_{\ell, m} \sum_{\ell', m'} a_{\ell m} a_{\ell' m'}^* (-1)^{\ell'} \delta_{\ell\ell'} \delta_{mm'} \quad (6.8d)$$

$$= \sum_{\ell, m} |a_{\ell m}|^2 (-1)^{\ell}, \quad (6.8e)$$

whose expectation value is $\sum_{\ell} (2\ell + 1) (-1)^{\ell} C_{\ell}$. From this expression, something can be said about the expected sign of $\langle Z(\hat{n}) \rangle$. C_{ℓ} is positive for all ℓ , so even- ℓ modes contribute positively and odd- ℓ modes contribute negatively. Assuming that the power spectrum for $\ell \geq 2$ is approximately proportional to $D_{\ell}/\ell(\ell + 1)$, the contribution of each D_{ℓ} to $\langle Z(\hat{n}) \rangle$ will fall off asymptotically as $1/\ell$:

$$\langle Z(\hat{n}) \rangle \approx \sum_{\ell} (-1)^{\ell} \frac{D_{\ell}}{\ell}.$$

Visualization of $Z(\hat{n})$

The map of $Z(\hat{n})$ is plotted in figure 6.2, calculated from the *Planck* 2018 SMICA map. This map is symmetric by construction, because $Z(\hat{n}) = Z(-\hat{n})$. Visible in figure 6.2 are

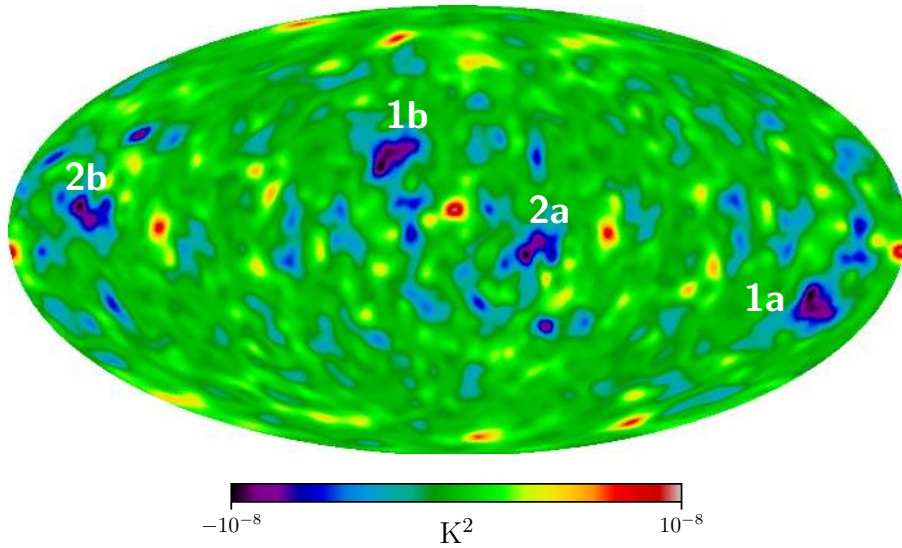


Figure 6.2: Map of $Z(\hat{n})$ from *Planck* 2018 SMICA with 5° smoothing. The map is symmetric by construction.

two pairs of strong negative peaks, labeled 1a/1b and 2a/2b, and several peaks with smaller amplitudes. The coordinates of the peaks 1a/1b and 2a/2b are:

$$\begin{aligned} 1a : (212^\circ, -21^\circ), & \quad 1b : (32^\circ, 21^\circ); \\ 2a : (332^\circ, -8^\circ), & \quad 2b : (152^\circ, 8^\circ). \end{aligned}$$

Something noticeable, and perhaps curious, about the direction of 1a/b is that it is very similar to the direction of the power asymmetry anomaly, for which [205] reports $(l, b) \approx (224^\circ, -22^\circ) \pm 24^\circ$, and [66] adopts $(l, b) = (221^\circ, -20^\circ)$ in a dipole modulation model.

If the peaks 1a/1b and 2a/2b are masked, even by relatively small disk masks that exclude only the peaks themselves, then the odd-parity preference is reduced to a large extent, and the power spectrum estimators, such as shown in figure 6.1, lose significance. Moderate Galactic masks can exclude 2a/b, and the most conservative Galactic masks will exclude 1a/1b. It was known that conservative masking can reduce the significance of the parity asymmetry. But now it is seen it is not the masking of the Galaxy *per se* that is responsible for this, but the masking of these particular anomalous regions.

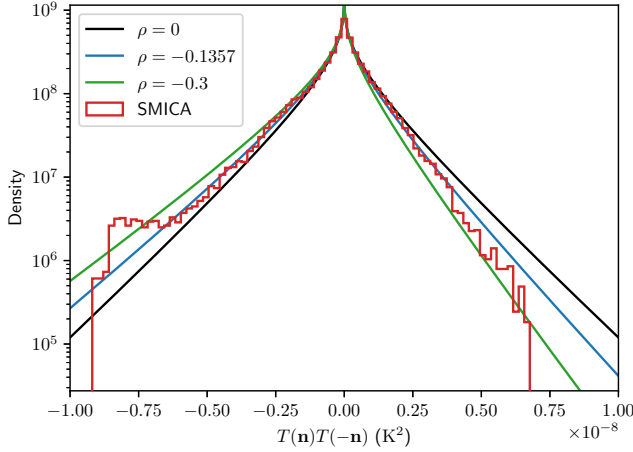


Figure 6.3: The distribution function expected of $Z(\hat{n})$ in the theoretical Gaussian model, for $\rho = 0$ (black), $\rho = -0.1357$ (blue), and $\rho = -0.3$ (green). The actual distribution from SMICA is shown in red.

Statistical properties of $Z(\hat{n})$

If $T(\hat{n})$ as a realization of an isotropic Gaussian random field, then so is $T(-\hat{n})$, but $T(\hat{n})$ and $T(-\hat{n})$ are not independent. Map-domain correlations between $T(\hat{n})$ and $T(-\hat{n})$ are expected. These are reflected in the two-point correlation function of the field. A simpler, but still useful, statistic is the cross-correlation between $T(\hat{n})$ and $T(-\hat{n})$, taken over the sky. Since there is no mean, $\int T(\hat{n}) d\hat{n} = 0$, the Pearson cross-correlation coefficient can be written as

$$\rho = \text{Corr}(T(\hat{n}), T(-\hat{n})) = \frac{\int T(\hat{n})T(-\hat{n}) d\hat{n}}{\int T(\hat{n})^2 d\hat{n}} = \frac{\sum_{\ell} (-1)^{\ell} \sum_m |a_{\ell m}|^2}{\sum_{\ell, m} |a_{\ell m}|^2}. \quad (6.9)$$

If the true value of ρ is known, then the point distribution function of $Z(\hat{n})$ is [206, 207]

$$\mathcal{P}(Z') = \frac{1}{\pi\sqrt{1-\rho^2}} \exp\left(\frac{\rho Z'}{1-\rho^2}\right) K_0\left(\frac{|Z'|}{1-\rho^2}\right), \quad (6.10)$$

where K_0 is the 0th order modified Bessel function of the second kind. The cross-correlation coefficient ρ therefore characterizes the shape of the distribution function of $Z(\hat{n})$. If $\rho = 0$, then the distribution function is symmetric; otherwise, it skews left (excess odd- ℓ power) or right (excess even- ℓ power) when $\rho < 0$ or $\rho > 0$ respectively.

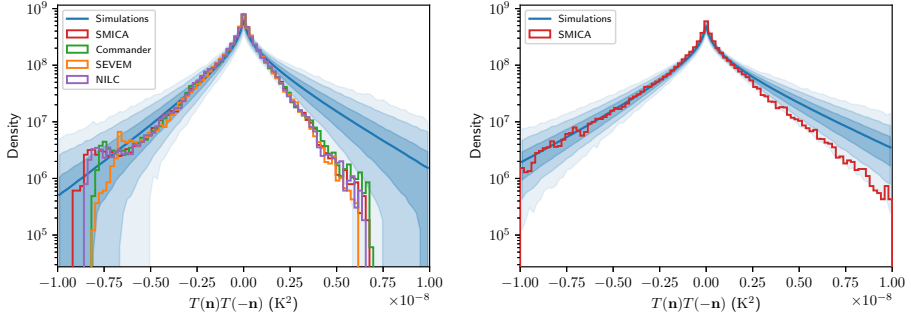


Figure 6.4: The left panel shows the distribution of $Z(\hat{n})$ from simulations (blue) and actual distribution of $Z(\hat{n})$ from SMICA (red) together with the other *Planck* maps. The smoothing angle is $\Theta = 5^\circ$. The shaded blue regions show the 68%, 95%, and 99.7% uncertainty regions. The departure in the right tail is at or slightly above the 3σ level. The right panel shows the same for SMICA at $\Theta = 2.5^\circ$.

The value of ρ estimated from SMICA is -0.1357 , suggesting an overall asymmetric excess. The empirical distribution function is shown in figure 6.3, together with the model of equation (6.10) for several values of ρ .

The fluctuations of the distribution function visible in figure 6.3 are more interesting. It is seen that on the left, there is a bump near $Z \approx -7 \times 10^{-8} \text{ K}^2$, which corresponds to the four negative peaks $1a/1b$ and $2a/2b$.

Comparison to simulations

To capture the full details of the map-domain morphology, and to estimate the significance of the departure, it is necessary to use simulations. Figure 6.4 shows the mean and uncertainty in the distribution functions determined from Gaussian simulations using the *Planck* best-fit cosmological parameters [4, 60]. The actual distribution functions agree well with the pointwise model of equation (6.10). The simulations have a slight positive preference for ρ which is reflected in the mean distribution function having a slight tilt to the right. The actual distribution function from SMICA, plotted again in figure 6.4, tilts left, departing from the uncertainty range of the simulations at about the 3σ level.

The left or right tilt of the distribution function is directly analogous to the $g(\ell_{\max})$ or $R(\ell_{\max})$ power spectrum estimators being less than 1 or greater than 1. The two approaches (figure 6.1 and figure 6.4), although very different in principle, yield a similar presentation of the anomaly with a similar significance. In figure 6.1, the anomaly can be localized in the multipole domain, with the maximum departure from the simulations occurring around $\ell \approx 25$. In figure 6.4, which is already associated with a certain multipole range via

the smoothing in use, the anomaly can further be localized in the map domain.

Note that the histograms are constrained by normalization. Although it is difficult to see in the figures due to the logarithmic vertical scale, it should be remarked that the CMB maps show a slight excess near the peak (low $|Z(\hat{n})|$) region. Such an excess is complementary to the deficits in the tails.

Hemispherical power asymmetry

There are two conceptions of the hemispherical power asymmetry: either it is exactly oriented and associated to the ecliptic plane, or it has an unknown generic orientation that is oriented approximately to the ecliptic plane, and may or may not be associated with it. In Galactic coordinates, the north and south ecliptic poles are

$$\begin{aligned} \text{North ecliptic pole} &: (l, b) = (96^\circ, 30^\circ); \\ \text{South ecliptic pole} &: (l, b) = (276^\circ, -30^\circ). \end{aligned}$$

The direction of the dipole modulation adopted by *Planck* [66] is $(221^\circ, -20^\circ)$, while a joint Bayesian analysis of the anomalies in [198] reports $(248^\circ, -20^\circ)$. The difference reflects the approximate level of uncertainty in the direction posteriors. It can be said that the direction recovered by general fitting of the model of equation (6.1) is not inconsistent with the South ecliptic pole.

It is possible to investigate the hemispherical power asymmetry in the map domain in a very simple way. The idea is to define an estimator which compares power at antipodal points, following the same principle as above where total even and odd ℓ power was compared at each point by $Z(\hat{n})$. The following estimator is defined:

$$G(\hat{n}) = T(\hat{n})^2 - T(-\hat{n})^2 = 4S(\hat{n})A(\hat{n}). \quad (6.11)$$

Assuming the dipolar model $T(\hat{n}) = (1 + \hat{m} \cdot \hat{n}D)T_{\text{iso}}(\hat{n})$, where \hat{m} is the direction of the dipole modulation (now a unit vector) and D is a constant reflecting its amplitude, the estimator $G(\hat{n})$ can be written

$$G(\hat{n}) = (-R(\hat{n}) + 2D \cos(\xi)(2 + R(\hat{n})) - R(\hat{n})D^2 \cos^2(\xi))T_{\text{iso}}(\hat{n})^2. \quad (6.12)$$

ξ is the angle between \hat{m} and \hat{n} , and

$$R(\hat{n}) + 1 = \frac{T_{\text{iso}}(-\hat{n})^2}{T_{\text{iso}}(\hat{n})^2}. \quad (6.13)$$

$R(\hat{n})$ is an asymmetry parameter. When $R(\hat{n}) \ll D$,

$$G(\hat{n}) \propto S(\hat{n})A(\hat{n}) \approx D \cos(\xi)T_{\text{iso}}(\hat{n})^2. \quad (6.14)$$

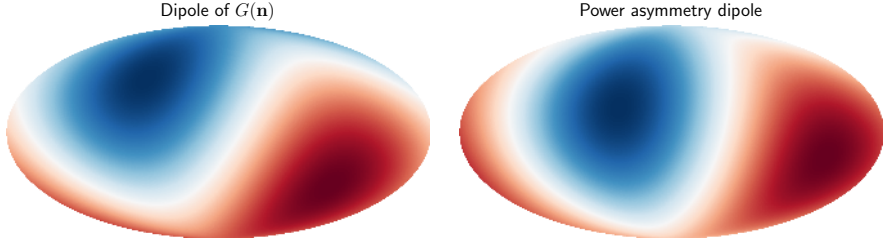


Figure 6.5: Dipole modulations recovered from $S(\hat{n})A(\hat{n})$ (left) and adopted in [66] (right).

Therefore, in this limit, the absolute difference between the antipodal amplitudes, i.e. $T(\hat{n})^2 - T(-\hat{n})^2$, which is $G(\hat{n})$, is proportional to $\cos(\xi)$. Because $T_{\text{iso}}(\hat{n})$ is isotropic by assumption, this is a map of the dipole modulation. This is plotted in figure 6.5, compared to the dipole modulation adopted in [66].

6.2 QUADRUPOLE–OCTUPOLE ALIGNMENT

An anomalous alignment of the quadrupole and octupole was reported for the WMAP data in [180]. Some sort of alignment is obvious from a comparison of the maps (see figure 6.6); however, in general, multipoles with $\ell \geq 3$ do not immediately have an obvious unique directionality, and this notion must be defined formally. In [180], the functional

$$D_1(\hat{n}) = \sum_{m=-\ell}^{\ell} m^2 |a_{\ell m}(\hat{n})|^2 \quad (6.15)$$

is maximized over directions \hat{n} , where $a_{\ell m}(\hat{n})$ is the harmonic transform taken in a coordinate system whose z -axis is oriented in the \hat{n} direction.¹ No efficient algorithm was known for this maximization; the authors of [180] propose a brute force sampling method.

In addition to angular momentum methods, more elaborate direction schemes have been proposed. The most notable is the Maxwell multipole vectors [208].

Once a definition of direction is established, numerous estimators for alignment are in use. An overview of the main results which constitute the low-multipole alignment is the following:

1. The planarity of the octupole (dominance of $m = \pm\ell$) is peculiar at the 5% level.
2. The quadrupole and octupole are aligned with a significance of 0.2% to 2%.

¹This is equivalent to maximizing the angular momentum dispersion in quantum mechanics, where the CMB serves as a “wavefunction”.

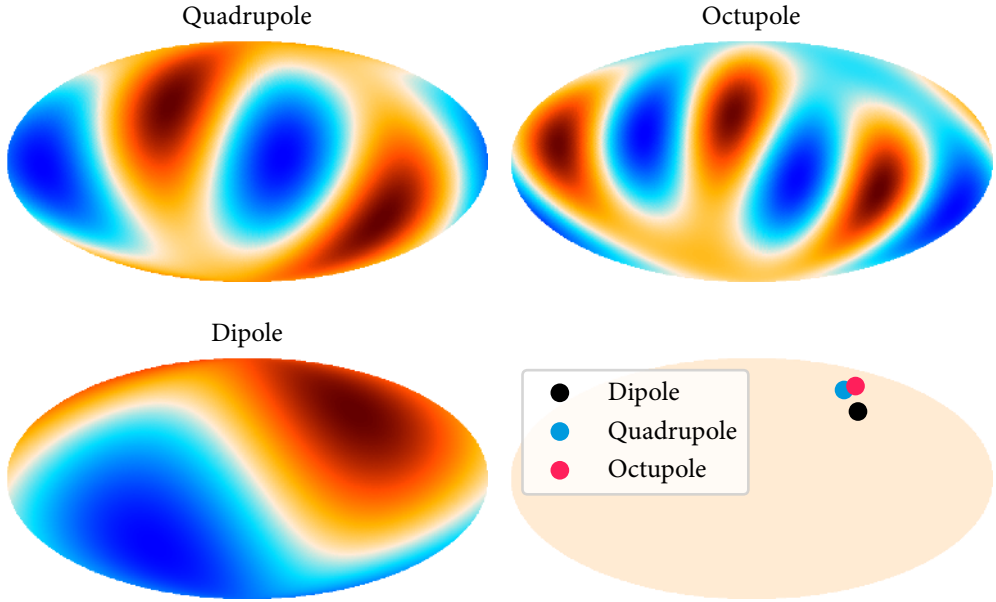


Figure 6.6: The first 3 multipoles and their directions. The planarity of the octupole is also visible in the nearly ring-like arrangement of its six strongest peaks.

3. The common quadrupole–octupole axis coincides with the dipole axis ($p < 0.5\%$).
4. The dipole–quadrupole–octupole axis is perpendicular to the ecliptic ($p = 2\%$).

If simply multiplied together, these results yield a fearsome p value, but one which is unlikely to have any rigorous meaning: not merely because such an estimator would be highly posterior, but also because these alignments, despite their first appearance, may not be statistically independent.

Kinematic dipole and the ring of attraction

The peaks 1a/1b and 2a/2b, which were responsible for the odd parity preference, are noticeably also featured in these alignments, although, like the ecliptic, they are orthogonal to the dipole axis. The dipole direction is measured to high accuracy: $(l, b) = (264.00^\circ \pm 0.03^\circ, 48.24^\circ \pm 0.02^\circ)$ [209]. If this direction is denoted \hat{q} , then a general description of orthogonality to the dipole axis is the ring of all directions \hat{g} such that

$$\hat{q} \cdot \hat{g} = 0. \quad (6.16)$$

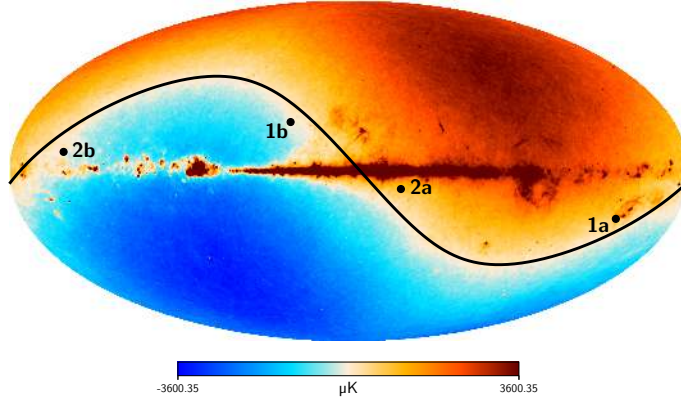


Figure 6.7: The 30 GHz frequency map from [74], before subtraction of the kinematic dipole, showing the ring of attraction and the peaks of the parity asymmetry.

Figure 6.7 and shows the position of this ring, which is called the “ring of attraction” in [23] by virtue of apparent attraction of the parity asymmetry peaks and also the low multipole peaks, discussed below.

Concentration of parity asymmetry peaks

It is noticeable in figure 6.7 that the peaks of the parity asymmetry, 1a/1b and 2a/2b, are aligned to the ring. To quantify this apparent correlation and estimate its significance, an estimator

$$d = \max_{|Z(\hat{n})| \geq \nu} (\hat{q} \cdot \hat{n}) \quad (6.17)$$

is defined for some peak threshold ν . The maximization is over all points exceeding the peak threshold. d gives the distance from the ring of attraction to the peaks. Figure 6.8 shows the values of this estimator for 4000 isotropic Gaussian simulations based on the *Planck* best-fit cosmological parameters, with the peak threshold $\nu = 7.5 \times 10^9 \text{ K}^2$. Because maps with fewer peak pixels are allowed a broader range in d , it is also necessary to consider how many pixels exceed the peak. These two quantities are not independent. The actual CMB map generally has fewer peak pixels than simulations, especially positive peaks (see figure 6.4). Nevertheless it is still found at the edge of the region encompassed by the simulations.

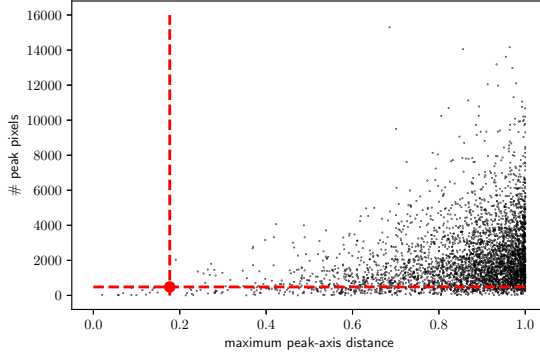


Figure 6.8: Each black dot shows the value of $\max_{|Z(\hat{n})| \geq \nu} (\hat{q} \cdot \hat{n})$ and the total number of peak pixels for 4000 simulations. The same values for SMICA are shown in red.

Concentration of low multipole peaks

The map of the ℓ th multipole can have up to 2^ℓ peaks. In an isotropic Gaussian random field, all directions are equally probable. Examination of the low multipole maps themselves seems to suggest that there is, in the CMB, some concentration of these peaks to the ring of attraction. Figure 6.9 shows the first 6 multipoles of SMICA. The maps of $\ell = 2$ and $\ell = 3$ have very clear planar peak structure aligned as discussed above: this is the well-known quadrupole–octupole alignment with the dipole. For $\ell \geq 4$, there are more peaks, and the peak structure is more complicated; nevertheless, there appear to be chains of peaks aligned with the ring of attraction. These are not necessarily the strongest peaks, but subsidiary chains of peaks. The alignment is especially visible in $\ell = 5$ and $\ell = 7$.

6.3 POLARIZATION

Lastly, we briefly comment on the possibility of applying map-domain analysis of the anomalies in polarization. Many of the estimators applied in this chapter can equally be applied to the polarization. Analysis of the anomalies in the polarization domain has important potential as an independent data set for verification of significance. Counterparts to the temperature anomalies, including the lack of correlations on large scales, have been searched for in the polarization data, and the link between the hemispherical power asymmetry and the B mode has been investigated [187, 200, 201, 210]. In figure 6.10, the Z asymmetry maps for the Stokes parameters Q and U are shown, computed as

$$Z_Q(\hat{n}) = Q(\hat{n})Q(-\hat{n}); \quad (6.18)$$

$$Z_U(\hat{n}) = U(\hat{n})U(-\hat{n}). \quad (6.19)$$

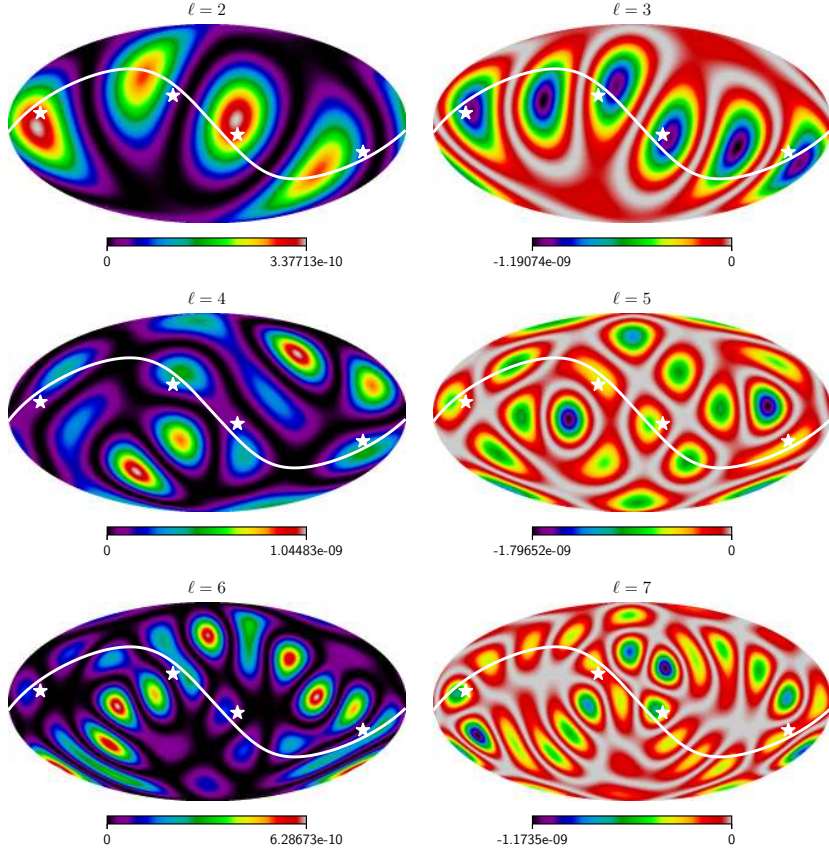


Figure 6.9: Maps of $Z_\ell(\hat{n})$ for even and odd multipoles. $Z_\ell(\hat{n})$ is equal to $(-1)^\ell T_\ell(\hat{n})^2$, where T_ℓ is the map of the ℓ th multipole.

In the Z_U map, there is a pair of positive Z peaks aligned with the ring of attraction. These peaks are also aligned to the pair of temperature peaks 1a/1b (see figure 6.2). Further study of this part of the sky, which is also near to the dipole modulation direction, is an important direction for future research.

Discussion of results

Beginning with the parity asymmetry, we have investigated the CMB anomalies in the pixel domain. The novel part of this analysis is that we can see what parts of the sky are

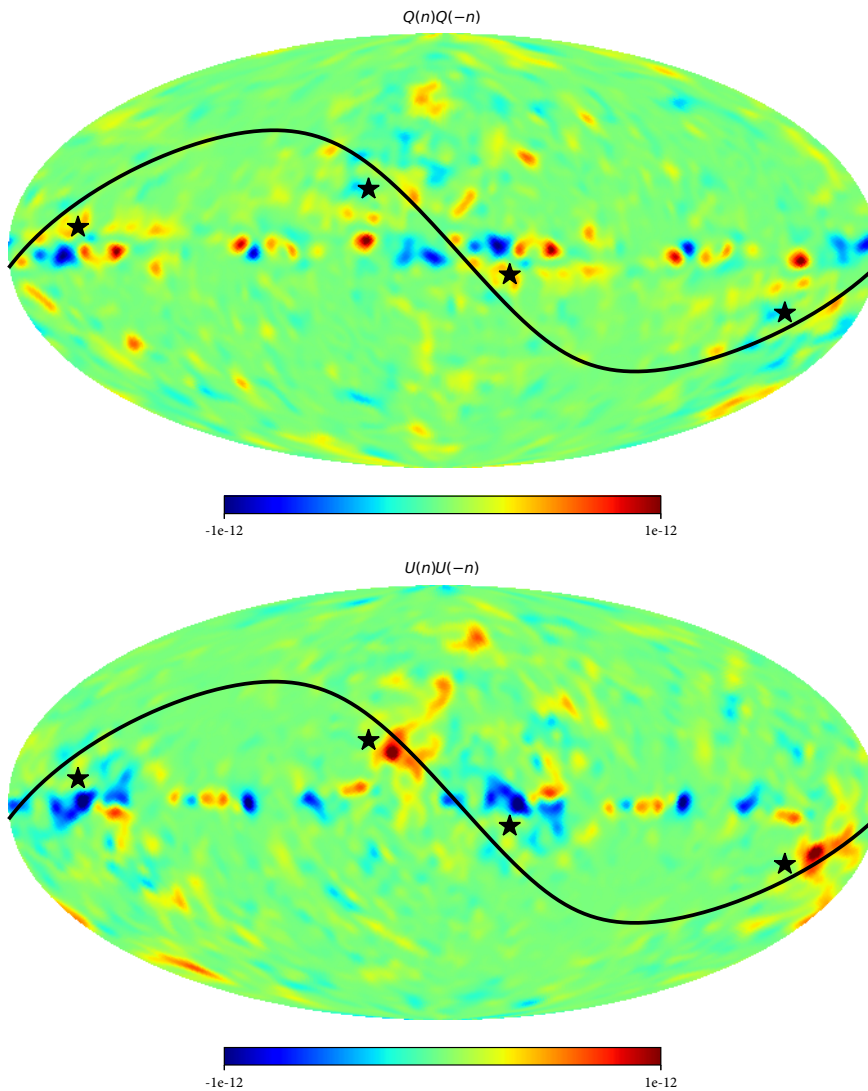


Figure 6.10: $Z_Q(\hat{n})$ and $Z_U(\hat{n})$ of SMICA at 5° smoothing. In much of the sky the maps are quite featureless, but $Z_U(\hat{n})$ map includes a pair of strong positive-parity excess regions near to the ring of attraction, shown in black.

contributing to the parity asymmetry, which was previously observed primarily in the domain of the power spectrum. The analysis shows that the parity asymmetry can be localized into two pairs of antipodal peaks. Despite comprising a very small area of the sky, these peaks are the origin of the 3σ parity asymmetry, and if they are masked by small point masks, the significance of the parity asymmetry can be greatly reduced.

The parity asymmetry is aligned with the dipole modulation asymmetry, and these anomalies share in the well-known quadrupole–octupole alignment and its counterpart, the ring of attraction containing directions perpendicular to the kinematic dipole. The alignment appears to be manifested in the subsidiary peaks of the low odd multipoles.

CONCLUSION AND OUTLOOK

In this thesis, new approaches to data analysis of the cosmic microwave background were proposed and applied to the observations made by *Planck*. The objective of this work is the development of methods that are sensitive to the statistical properties of the CMB, together with improvement in the understanding of the B mode of the CMB polarization. It is hoped that these tools can benefit the high-precision CMB observations expected in the next decade.

A new method for calculating families of the Stokes parameters associated with the E and B modes was presented. Unlike the standard E–B decomposition which is performed by a harmonic transformation, the new approach has a natural formulation in the map domain as a linear convolution. The convolution kernels, which were explicitly computed, show exactly the non-locality of the E and B modes.


The description of polarization data in terms of a polarization intensity and an orientation has been exploited in many contexts. By remaining in the space of the Stokes parameters, it is now possible to define intensities and angles corresponding to each of the E and B modes. These estimators have widespread applications in data analysis, some of which were illustrated in the study of the morphology of the *Planck* 217 GHz and 353 GHz frequency maps, which are dominated by thermal dust foreground emission.

The problem of E–B leakage was addressed and a new method for its correction was presented. The method is simple in principle and easy to implement, and, under realistic simulated parameters corresponding roughly to the upcoming GreenPol experiment, it was able to improve the accuracy of the recovered B mode considerably. Ground-based observations will inevitably face E–B leakage, and the method was able to reduce the error down to a level that does not interfere with the detection of very small tensor-to-scalar ratios at the $r \approx 10^5$ level. The performance of the method is likely to depend on the shape of the mask. Further characterization of the method under different circumstances is a direction for future research. In particular, the performance for irregular Galactic masks or point source masks should be examined.

Assuming underlying Gaussian polarization data, the distribution function of the polarization angle was considered. The statistical dependence of the polarization angle on the properties of the Stokes parameters was established in the context of the E and B modes, which were found to leave a specific signature in the polarization angle distribution func-

tion, related to the Q and U means. The histogram of the polarization angle seems to be an attractive estimator not only for tests of systematic errors, which was applied herein to the 2018 *Planck* CMB maps and best-fit power spectra, but also to other corruptions like E–B leakage. E–B leakage may leave an imprint in the polarization angles, which could be informative in the construction and validation of leakage correction methods, although this has not yet been studied in detail.

It had been known that non-polarized points of the CMB polarization field can be classified into saddles, knots, and focuses that occur with fixed ratios under Gaussian statistics. This fact was used to construct a new local test of Gaussianity that works in the map domain, which was applied to the *Planck* CMB maps. Several other theoretical results were worked out, including the dependence of the total number density of non-polarized points on gravitational lensing and the tensor-to-scalar ratio. The non-polarized points theory can now be applied to E and B separately in terms of the E and B families, which are polarization fields with the same mathematical capabilities as the total unseparated signal. Applied to the *Planck* 2018 CMB maps, the non-polarized points appear to be generally consistent with Gaussianity, despite a marginal ($p \approx 1\%$) signal in the SEVEM map. There is potential for the construction of many further tests of Gaussianity and isotropy based on the non-polarized points, and, like the polarization angle, they too could be sensitive to systematics. Software written in Python for the detection and analysis of non-polarized points, developed for the project in this thesis, is now released in the public domain.

Lastly, the large-scale anomalies of the CMB were investigated using map-domain methods. While the anomalies persist, with marginal significance, in all applicable datasets, their continued study is an important research question. Working with a simple map-domain estimator to compare the even-parity and odd-parity power, it was shown that the odd-parity excess can be localized to a relatively small part of the sky. Furthermore, the parity asymmetry participates with the low multipoles in a suspicious alignment related to the kinematic dipole direction. In particular, subsidiary peaks of the low multipoles, especially $\ell = 5$ and $\ell = 7$, appear to be attracted to directions that are perpendicular to the kinematic dipole, forming rings that resemble the well-known quadrupole and octupole anomalies. These features in the low multipole maps justify continued effort in the map-domain study of the anomalies, especially the estimation of the significance of the subsidiary peak alignments. It is considered likely that the anomalies reflect a systematic error, rather than an error in the prevailing theories of cosmology. In view of the findings here, the subtraction of the kinematic dipole seems to deserve further attention. 

REFERENCES

- [1] V. F. Mukhanov and G. V. Chibisov, “Quantum Fluctuations and a Nonsingular Universe”, *JETP Lett.* **33**, 532–535 (1981).
- [2] V. F. Mukhanov, H. A. Feldman, and R. H. Brandenberger, “Theory of cosmological perturbations. Part 1. Classical perturbations. Part 2. Quantum theory of perturbations. Part 3. Extensions”, *Phys. Rept.* **215**, 203–333 (1992).
- [3] N. Aghanim et al. (Planck), “Planck 2018 results. I. Overview and the cosmological legacy of Planck”, *Astron. Astrophys.* **641**, A1 (2020), [arXiv:1807.06205 \[astro-ph.CO\]](#).
- [4] N. Aghanim et al. (Planck), “Planck 2018 results. VI. Cosmological parameters”, *Astron. Astrophys.* **641**, A6 (2020), [arXiv:1807.06209 \[astro-ph.CO\]](#).
- [5] P. A. R. Ade et al. (BICEP2, Planck), “Joint Analysis of BICEP2/*KeckArray* and *Planck* Data”, *Phys. Rev. Lett.* **114**, 101301 (2015), [arXiv:1502.00612 \[astro-ph.CO\]](#).
- [6] Y. Akrami et al. (Planck), “Planck 2018 results. X. Constraints on inflation”, *Astron. Astrophys.* **641**, A10 (2020), [arXiv:1807.06211 \[astro-ph.CO\]](#).
- [7] M. Hazumi et al., “LiteBIRD: a small satellite for the study of B-mode polarization and inflation from cosmic background radiation detection”, *Proc. SPIE Int. Soc. Opt. Eng.* **8442**, 844219 (2012).
- [8] T. Matsumura et al., “Mission design of LiteBIRD”, *J. Low Temp. Phys.* **176**, 733 (2014), [arXiv:1311.2847 \[astro-ph.IM\]](#).
- [9] M. Hazumi et al., “LiteBIRD: A Satellite for the Studies of B-Mode Polarization and Inflation from Cosmic Background Radiation Detection”, *J. Low Temp. Phys.* **194**, 443–452 (2019).
- [10] K. N. Abazajian et al. (CMB-S4), “CMB-S4 Science Book, First Edition”, (2016), [arXiv:1610.02743 \[astro-ph.CO\]](#).
- [11] P. Ade et al. (Simons Observatory), “The Simons Observatory: Science goals and forecasts”, *JCAP* **02**, 056 (2019), [arXiv:1808.07445 \[astro-ph.CO\]](#).
- [12] H. Li et al., “Probing Primordial Gravitational Waves: Ali CMB Polarization Telescope”, *Natl. Sci. Rev.* **6**, 145–154 (2019), [arXiv:1710.03047 \[astro-ph.CO\]](#).

- [13] U. Seljak and M. Zaldarriaga, “Signature of gravity waves in polarization of the microwave background”, *Phys. Rev. Lett.* **78**, 2054–2057 (1997), [arXiv:astro-ph/9609169](#).
- [14] M. Kamionkowski, A. Kosowsky, and A. Stebbins, “A Probe of primordial gravity waves and vorticity”, *Phys. Rev. Lett.* **78**, 2058–2061 (1997), [arXiv:astro-ph/9609132](#).
- [15] M. Kamionkowski, “Cosmic microwave background tests of inflation”, *Nucl. Phys. B Proc. Suppl.* **70**, edited by A. Bottino, A. Di Credico, and P. Monacelli, 529–536 (1999), [arXiv:astro-ph/9712215](#).
- [16] H. Liu, J. Creswell, and P. Naselsky, “E and B families of the Stokes parameters in the polarized synchrotron and thermal dust foregrounds”, *JCAP* **05**, 059 (2018), [arXiv:1804.10382 \[astro-ph.CO\]](#).
- [17] H. Liu, J. Creswell, S. von Hausegger, and P. Naselsky, “Methods for pixel domain correction of EB leakage”, *Phys. Rev. D* **100**, 023538 (2019), [arXiv:1811.04691 \[astro-ph.CO\]](#).
- [18] H. Liu, J. Creswell, S. von Hausegger, and P. Naselsky, “From top-hat masking to smooth transitions: P-filter and its application to polarized microwave sky maps”, *JCAP* **05**, 003 (2019), [arXiv:1904.04124 \[astro-ph.CO\]](#).
- [19] H. Liu, J. Creswell, and K. Dachlythra, “Blind correction of the EB-leakage in the pixel domain”, *JCAP* **04**, 046 (2019), [arXiv:1904.00451 \[astro-ph.CO\]](#).
- [20] J. Creswell, N. Dachlythra, H. Liu, P. Naselsky, and P. R. Christensen, “Statistics of CMB polarization angles”, *JCAP* **02**, 001 (2020), [arXiv:2001.01757 \[astro-ph.CO\]](#).
- [21] J. Kasak, J. Creswell, P. Naselsky, and H. Liu, “Statistics of nonpolarized points in the CMB polarization maps”, *Phys. Rev. D* **104**, 023502 (2021), [arXiv:2012.15811 \[astro-ph.CO\]](#).
- [22] J. Creswell and P. Naselsky, “Asymmetry of the CMB map: local and global anomalies”, *JCAP* **03**, 103 (2021), [arXiv:2102.13442 \[astro-ph.CO\]](#).
- [23] J. Creswell and P. Naselsky, “Ring of attraction: overlapping directions of the dipole modulation of the CMB, the parity asymmetry, and kinematic dipole percolation zone”, (2021), [arXiv:2105.08658 \[astro-ph.CO\]](#).
- [24] A. H. Guth, “The Inflationary Universe: A Possible Solution to the Horizon and Flatness Problems”, *Phys. Rev. D* **23**, edited by L.-Z. Fang and R. Ruffini, 347–356 (1981).
- [25] A. D. Linde, “A New Inflationary Universe Scenario: A Possible Solution of the Horizon, Flatness, Homogeneity, Isotropy and Primordial Monopole Problems”, *Phys. Lett. B* **108**, edited by L.-Z. Fang and R. Ruffini, 389–393 (1982).

- [26] A. A. Starobinsky, “Spectrum of relict gravitational radiation and the early state of the universe”, *JETP Lett.* **30**, edited by I. M. Khalatnikov and V. P. Mineev, 682–685 (1979).
- [27] P. A. R. Ade et al. (Planck), “Planck 2015 results. XX. Constraints on inflation”, *Astron. Astrophys.* **594**, A20 (2016), [arXiv:1502.02114 \[astro-ph.CO\]](#).
- [28] M. Tristram et al., “Planck constraints on the tensor-to-scalar ratio”, *Astron. Astrophys.* **647**, A128 (2021), [arXiv:2010.01139 \[astro-ph.CO\]](#).
- [29] A. A. Penzias and R. W. Wilson, “A Measurement of Excess Antenna Temperature at 4080 Mc/s.”, *apj* **142**, 419–421 (1965).
- [30] R. H. Dicke, P. J. E. Peebles, P. G. Roll, and D. T. Wilkinson, “Cosmic Black-Body Radiation.”, *apj* **142**, 414–419 (1965).
- [31] G. Gamow, “The Evolution of the Universe”, *Nature* **162**, 680–682 (1948).
- [32] R. A. Alpher and R. C. Herman, “On the Relative Abundance of the Elements”, *Phys. Rev.* **74**, 1737–1742 (1948).
- [33] R. A. Alpher and R. C. Herman, “Theory of the Origin and Relative Abundance Distribution of the Elements”, *Rev. Mod. Phys.* **22**, 153–212 (1950).
- [34] R. A. Alpher and R. C. Herman, “The origin and abundance distribution of the elements”, *Ann. Rev. Nucl. Part. Sci.* **2**, 1–40 (1953).
- [35] A. G. Doroshkevich and I. D. Novikov, “Mean Density of Radiation in the Metagalaxy and Certain Problems in Relativistic Cosmology”, *Soviet Physics Doklady* **9**, 111 (1964).
- [36] I. A. Strukov, A. A. Brukhanov, D. P. Skulachev, and M. V. Sazhin, “Anisotropy of the microwave background radiation”, *Soviet Astronomy Letters* **18**, 153 (1992).
- [37] A. A. Klypin, I. A. Strukov, and D. P. Skulachev, “The Relikt missions: results and prospects for detection of the microwave background anisotropy”, *Monthly Notices of the Royal Astronomical Society* **258**, 71–81 (1992).
- [38] G. F. Smoot et al. (COBE), “Structure in the COBE differential microwave radiometer first year maps”, *Astrophys. J. Lett.* **396**, L1–L5 (1992).
- [39] N. W. Boggess et al., “The COBE mission - Its design and performance two years after launch”, *Astrophys. J.* **397**, 420–429 (1992).
- [40] C. L. Bennett, A. Banday, K. M. Gorski, G. Hinshaw, P. Jackson, P. Keegstra, A. Kogut, G. F. Smoot, D. T. Wilkinson, and E. L. Wright, “Four year COBE DMR cosmic microwave background observations: Maps and basic results”, *Astrophys. J. Lett.* **464**, L1–L4 (1996), [arXiv:astro-ph/9601067](#).
- [41] G. F. Smoot, “COBE observations and results”, *AIP Conf. Proc.* **476**, edited by L. Maiani, F. Melchiorri, and N. Vittorio, 1–10 (1999), [arXiv:astro-ph/9902027](#).

- [42] C. L. Bennett et al. (WMAP), “The Microwave Anisotropy Probe (MAP) mission”, *Astrophys. J.* **583**, 1–23 (2003), [arXiv:astro-ph/0301158](#).
- [43] G. Hinshaw et al. (WMAP), “Five-Year Wilkinson Microwave Anisotropy Probe (WMAP) Observations: Data Processing, Sky Maps, and Basic Results”, *Astrophys. J. Suppl.* **180**, 225–245 (2009), [arXiv:0803.0732 \[astro-ph\]](#).
- [44] C. L. Bennett et al. (WMAP), “Nine-Year Wilkinson Microwave Anisotropy Probe (WMAP) Observations: Final Maps and Results”, *Astrophys. J. Suppl.* **208**, 20 (2013), [arXiv:1212.5225 \[astro-ph.CO\]](#).
- [45] D. N. Spergel et al. (WMAP), “First year Wilkinson Microwave Anisotropy Probe (WMAP) observations: Determination of cosmological parameters”, *Astrophys. J. Suppl.* **148**, 175–194 (2003), [arXiv:astro-ph/0302209](#).
- [46] G. Hinshaw et al. (WMAP), “Nine-Year Wilkinson Microwave Anisotropy Probe (WMAP) Observations: Cosmological Parameter Results”, *Astrophys. J. Suppl.* **208**, 19 (2013), [arXiv:1212.5226 \[astro-ph.CO\]](#).
- [47] “The Scientific programme of Planck”, edited by J. Tauber et al. (2006), [arXiv:astro-ph/0604069](#).
- [48] R. Gualtieri et al. (SPIDER), “SPIDER: CMB Polarimetry from the Edge of Space”, *J. Low Temp. Phys.* **193**, 1112–1121 (2018), [arXiv:1711.10596 \[astro-ph.CO\]](#).
- [49] P. A. R. Ade et al. (SPIDER), “A Constraint on Primordial B -Modes from the First Flight of the SPIDER Balloon-Borne Telescope”, (2021), [arXiv:2103.13334 \[astro-ph.CO\]](#).
- [50] S. Aiola et al. (LSPE), “The Large-Scale Polarization Explorer (LSPE)”, *Proc. SPIE Int. Soc. Opt. Eng.* **8446**, edited by I. S. McLean, S. K. Ramsay, and H. Takami, 84467A (2012), [arXiv:1208.0281 \[astro-ph.IM\]](#).
- [51] P. de Bernardis, S. Masi, and OLIMPO and LSPE Teams, “Precision CMB measurements with long-duration stratospheric balloons: activities in the Arctic”, in *Astrophysics from antarctica*, Vol. 288, edited by M. G. Burton, X. Cui, and N. F. H. Tothill (Jan. 2013), pp. 208–213.
- [52] F. Piacentini, A. Coppolecchia, P. de Bernardis, G. Di Stefano, A. Iarocci, L. Lamagna, S. Masi, S. Peterzen, and R. Giovanni, “Winter long duration stratospheric balloons from Polar regions”, arXiv e-prints, [arXiv:1810.05565](#), [arXiv:1810.05565](#) (2018), [arXiv:1810.05565 \[astro-ph.IM\]](#).
- [53] H. Hui et al., “BICEP Array: a multi-frequency degree-scale CMB polarimeter”, *Proc. SPIE Int. Soc. Opt. Eng.* **10708**, edited by G. Z. Angeli and P. Dierickx, 1070807 (2018), [arXiv:1808.00568 \[astro-ph.IM\]](#).
- [54] S. Naess et al. (ACTPol), “The Atacama Cosmology Telescope: CMB Polarization at $200 < \ell < 9000$ ”, *JCAP* **10**, 007 (2014), [arXiv:1405.5524 \[astro-ph.CO\]](#).

- [55] A. Suzuki et al. (POLARBEAR), “The POLARBEAR-2 and the Simons Array Experiment”, *J. Low Temp. Phys.* **184**, edited by P. Camus, A. Juillard, and A. Monfardini, 805–810 (2016), [arXiv:1512.07299 \[astro-ph.IM\]](#).
- [56] R. Genova-Santos et al. (QUIJOTE), “The QUIJOTE experiment: project overview and first results”, in 11th Scientific Meeting of the Spanish Astronomical Society (Apr. 2015), [arXiv:1504.03514 \[astro-ph.CO\]](#).
- [57] B. A. Benson et al. (SPT-3G), “SPT-3G: A Next-Generation Cosmic Microwave Background Polarization Experiment on the South Pole Telescope”, *Proc. SPIE Int. Soc. Opt. Eng.* **9153**, 91531P (2014), [arXiv:1407.2973 \[astro-ph.IM\]](#).
- [58] D. J. Fixsen, E. S. Cheng, J. M. Gales, J. C. Mather, R. A. Shafer, and E. L. Wright, “The Cosmic Microwave Background spectrum from the full COBE FIRAS data set”, *Astrophys. J.* **473**, 576 (1996), [arXiv:astro-ph/9605054](#).
- [59] D. J. Fixsen and J. C. Mather, “The Spectral Results of the Far-Infrared Absolute Spectrophotometer Instrument on COBE”, *The Astrophysical Journal* **581**, 817–822 (2002).
- [60] N. Aghanim et al. (Planck), “Planck 2018 results. V. CMB power spectra and likelihoods”, *Astron. Astrophys.* **641**, A5 (2020), [arXiv:1907.12875 \[astro-ph.CO\]](#).
- [61] G. G. Stokes, “On the Composition and Resolution of Streams of Polarized Light from different Sources”, *Transactions of the Cambridge Philosophical Society* **9**, 399 (1851).
- [62] M. Kamionkowski, A. Kosowsky, and A. Stebbins, “Statistics of cosmic microwave background polarization”, *Phys. Rev. D* **55**, 7368–7388 (1997), [arXiv:astro-ph/9611125](#).
- [63] K. M. Gorski, B. D. Wandelt, F. K. Hansen, E. Hivon, and A. J. Banday, “The healpix primer”, (1999), [arXiv:astro-ph/9905275](#).
- [64] S. Plaszczynski, L. Montier, F. Levrier, and M. Tristram, “A novel estimator of the polarization amplitude from normally distributed Stokes parameters”, *Mon. Not. Roy. Astron. Soc.* **439**, 4048–4056 (2014), [arXiv:1312.0437 \[astro-ph.CO\]](#).
- [65] J. N. Goldberg, A. J. Macfarlane, E. T. Newman, F. Rohrlich, and E. C. G. Sudarshan, “Spin-s spherical harmonics and δ ”, *Journal of Mathematical Physics* **8**, 2155–2161 (1967), eprint: <https://doi.org/10.1063/1.1705135>.
- [66] Y. Akrami et al. (Planck), “Planck 2018 results. VII. Isotropy and Statistics of the CMB”, *Astron. Astrophys.* **641**, A7 (2020), [arXiv:1906.02552 \[astro-ph.CO\]](#).
- [67] M. Bucher, “Physics of the cosmic microwave background anisotropy”, *Int. J. Mod. Phys. D* **24**, 1530004 (2015), [arXiv:1501.04288 \[astro-ph.CO\]](#).
- [68] M. Zaldarriaga and U. Seljak, “An all sky analysis of polarization in the microwave background”, *Phys. Rev. D* **55**, 1830–1840 (1997), [arXiv:astro-ph/9609170](#).

- [69] A. Rotti and K. Huffenberger, “Real-space computation of E/B-mode maps. Part I. Formalism, compact kernels, and polarized filaments”, *JCAP* **01**, 045 (2019), [arXiv:1807.11940 \[astro-ph.CO\]](#).
- [70] M. Kamionkowski and E. D. Kovetz, “The Quest for B Modes from Inflationary Gravitational Waves”, *Ann. Rev. Astron. Astrophys.* **54**, 227–269 (2016), [arXiv:1510.06042 \[astro-ph.CO\]](#).
- [71] A. Lewis, “Harmonic E/B decomposition for CMB polarization maps”, *Phys. Rev. D* **68**, 083509 (2003), [arXiv:astro-ph/0305545](#).
- [72] E. F. Bunn, M. Zaldarriaga, M. Tegmark, and A. de Oliveira-Costa, “E/B decomposition of finite pixelized CMB maps”, *Phys. Rev. D* **67**, 023501 (2003), [arXiv:astro-ph/0207338](#).
- [73] E. F. Bunn, “Separating E from B”, *New Astron. Rev.* **47**, 987 (2003), [arXiv:astro-ph/0306003](#).
- [74] K. J. Andersen et al. (BeyondPlanck), “BeyondPlanck I. Global Bayesian analysis of the Planck Low Frequency Instrument data”, in BeyondPlanck Release Conference (Nov. 2020), [arXiv:2011.05609 \[astro-ph.CO\]](#).
- [75] R. Adam et al. (Planck), “Planck 2015 results. X. Diffuse component separation: Foreground maps”, *Astron. Astrophys.* **594**, A10 (2016), [arXiv:1502.01588 \[astro-ph.CO\]](#).
- [76] H. Liu, S. von Hausegger, and P. Naselsky, “Towards understanding the Planck thermal dust models”, *Phys. Rev. D* **95**, 103517 (2017), [arXiv:1705.05530 \[astro-ph.CO\]](#).
- [77] P. A. R. Ade et al. (Planck), “Planck intermediate results. XIX. An overview of the polarized thermal emission from Galactic dust”, *Astron. Astrophys.* **576**, A104 (2015), [arXiv:1405.0871 \[astro-ph.GA\]](#).
- [78] Y. Akrami et al. (Planck), “Planck 2018 results. XI. Polarized dust foregrounds”, *Astron. Astrophys.* **641**, A11 (2020), [arXiv:1801.04945 \[astro-ph.GA\]](#).
- [79] C. Dickinson, “CMB foregrounds - A brief review”, in 51st Rencontres de Moriond on Cosmology (June 2016), [arXiv:1606.03606 \[astro-ph.CO\]](#).
- [80] B. T. Draine and A. A. Fraisse, “Polarized Far-Infrared and Submillimeter Emission from Interstellar Dust”, *Astrophys. J.* **696**, [Erratum: *Astrophys. J.* 757, 106 (2012)], 1–11 (2009), [arXiv:0809.2094 \[astro-ph\]](#).
- [81] D. P. Finkbeiner, D. J. Schlegel, C. Frank, and C. Heiles, “Tentative detection of electric dipole emission from rapidly rotating dust grains”, *Astrophys. J.* **566**, 898 (2002), [arXiv:astro-ph/0109534](#).
- [82] D. P. Finkbeiner, “Microwave ISM emission observed by WMAP”, *Astrophys. J.* **614**, 186–193 (2004), [arXiv:astro-ph/0311547](#).

- [83] A. de Oliveira-Costa, M. Tegmark, R. D. Davies, C. M. Gutierrez, A. N. Lasenby, R. Rebolo, and R. A. Watson, “The Quest for microwave Foreground X”, *Astrophys. J. Lett.* **606**, L89–L92 (2004), [arXiv:astro-ph/0312039](#).
- [84] G. Dobler and D. P. Finkbeiner, “Extended Anomalous Foreground Emission in the WMAP 3-Year Data”, *Astrophys. J.* **680**, 1222–1234 (2008), [arXiv:0712.1038 \[astro-ph\]](#).
- [85] R. Adam et al. (Planck), “Planck intermediate results. XXX. The angular power spectrum of polarized dust emission at intermediate and high Galactic latitudes”, *Astron. Astrophys.* **586**, A133 (2016), [arXiv:1409.5738 \[astro-ph.CO\]](#).
- [86] P. A. R. Ade et al. (Planck), “Planck intermediate results. XXII. Frequency dependence of thermal emission from Galactic dust in intensity and polarization”, *Astron. Astrophys.* **576**, A107 (2015), [arXiv:1405.0874 \[astro-ph.GA\]](#).
- [87] P. A. R. Ade et al. (Planck), “Planck intermediate results. XXXVIII. E- and B-modes of dust polarization from the magnetized filamentary structure of the interstellar medium”, *Astron. Astrophys.* **586**, A141 (2016), [arXiv:1505.02779 \[astro-ph.GA\]](#).
- [88] N. Aghanim et al. (Planck), “Planck intermediate results - L. Evidence of spatial variation of the polarized thermal dust spectral energy distribution and implications for CMB B-mode analysis”, *Astron. Astrophys.* **599**, A51 (2017), [arXiv:1606.07335 \[astro-ph.CO\]](#).
- [89] R. Cepeda-Arroita et al., “Detection of spectral variations of Anomalous Microwave Emission with QUIJOTE and C-BASS”, *Mon. Not. Roy. Astron. Soc.* **503**, 2927–2943 (2021), [arXiv:2001.07159 \[astro-ph.GA\]](#).
- [90] A. G. Kritsuk, R. Flauger, and S. D. Ustyugov, “Dust-polarization maps for local interstellar turbulence”, *Phys. Rev. Lett.* **121**, 021104 (2018), [arXiv:1711.11108 \[astro-ph.GA\]](#).
- [91] D. Kandel, A. Lazarian, and D. Pogosyan, “Statistical properties of galactic CMB foregrounds: dust and synchrotron”, *Mon. Not. Roy. Astron. Soc.* **478**, 530–540 (2018), [arXiv:1711.03161 \[astro-ph.GA\]](#).
- [92] A. Bracco, T. Ghosh, F. Boulanger, and J. Aumont, “Link between E–B polarization modes and gas column density from interstellar dust emission”, *Astron. Astrophys.* **632**, A17 (2019), [arXiv:1905.10471 \[astro-ph.GA\]](#).
- [93] C. Hervias-Caimapo, A. Bonaldi, and M. L. Brown, “Impact of modelling foreground uncertainties on future CMB polarization satellite experiments”, *Mon. Not. Roy. Astron. Soc.* **468**, 4408–4418 (2017), [arXiv:1701.02277 \[astro-ph.CO\]](#).
- [94] C. Hervias-Caimapo, A. Bonaldi, M. L. Brown, and K. M. Huffenberger, “Galactic foreground constraints on primordial B-mode detection for ground-based experiments”, (2021), [arXiv:2105.06311 \[astro-ph.CO\]](#).

- [95] M. Kamionkowski and E. D. Kovetz, “Statistical diagnostics to identify Galactic foregrounds in B-mode maps”, *Phys. Rev. Lett.* **113**, 191303 (2014), [arXiv:1408.4125 \[astro-ph.CO\]](#).
- [96] A. Rotti and K. Huffenberger, “Isotropy-Violation Diagnostics for *B*-mode Polarization Foregrounds to the Cosmic Microwave Background”, *JCAP* **09**, 034 (2016), [arXiv:1604.08946 \[astro-ph.CO\]](#).
- [97] O. H. E. Philcox, B. D. Sherwin, and A. van Engelen, “Detection and Removal of B-mode Dust Foregrounds with Signatures of Statistical Anisotropy”, *Mon. Not. Roy. Astron. Soc.* **479**, 5577–5595 (2018), [arXiv:1805.09177 \[astro-ph.CO\]](#).
- [98] R. Adam et al. (Planck), “Planck 2015 results. IX. Diffuse component separation: CMB maps”, *Astron. Astrophys.* **594**, A9 (2016), [arXiv:1502.05956 \[astro-ph.CO\]](#).
- [99] Y. Akrami et al. (Planck), “Planck 2018 results. IV. Diffuse component separation”, *Astron. Astrophys.* **641**, A4 (2020), [arXiv:1807.06208 \[astro-ph.CO\]](#).
- [100] H. K. Eriksen, I. J. O’Dwyer, J. B. Jewell, B. D. Wandelt, D. L. Larson, K. M. Gorski, S. Levin, A. J. Banday, and P. B. Lilje, “Power spectrum estimation from high-resolution maps by Gibbs sampling”, *Astrophys. J. Suppl.* **155**, 227–241 (2004), [arXiv:astro-ph/0407028](#).
- [101] H. K. Eriksen, J. B. Jewell, C. Dickinson, A. J. Banday, K. M. Gorski, and C. R. Lawrence, “Joint Bayesian component separation and CMB power spectrum estimation”, *Astrophys. J.* **676**, 10–32 (2008), [arXiv:0709.1058 \[astro-ph\]](#).
- [102] D. S. Seljebotn, T. Bærland, H. K. Eriksen, K. A. Mardal, and I. K. Wehus, “Multi-resolution Bayesian CMB component separation through Wiener-filtering with a pseudo-inverse preconditioner”, *Astron. Astrophys.* **627**, A98 (2019), [arXiv:1710.00621 \[astro-ph.IM\]](#).
- [103] S. Basak and J. Delabrouille, “A needlet ILC analysis of WMAP 7-year data: estimation of CMB temperature map and power spectrum”, *Mon. Not. Roy. Astron. Soc.* **419**, 1163 (2012), [arXiv:1106.5383 \[astro-ph.CO\]](#).
- [104] S. Basak and J. Delabrouille, “A needlet ILC analysis of WMAP 7-year polarisation data: CMB polarisation power spectra”, *Mon. Not. Roy. Astron. Soc.* **435**, 18 (2013), [arXiv:1204.0292 \[astro-ph.CO\]](#).
- [105] S. M. Leach et al., “Component separation methods for the Planck mission”, *Astron. Astrophys.* **491**, 597–615 (2008), [arXiv:0805.0269 \[astro-ph\]](#).
- [106] J. Delabrouille, J.-F. Cardoso, and G. Patanchon, “Multi-detector multi-component spectral matching and applications for CMB data analysis”, *Mon. Not. Roy. Astron. Soc.* **346**, 1089 (2003), [arXiv:astro-ph/0211504](#).

- [107] J.-F. Cardoso, M. Le Jeune, J. Delabrouille, M. Betoule, and G. Patanchon, “Component Separation With Flexible Models—Application to Multichannel Astrophysical Observations”, *IEEE Journal of Selected Topics in Signal Processing* **2**, 735–746 (2008).
- [108] M. Zaldarriaga and U. Seljak, “Gravitational lensing effect on cosmic microwave background polarization”, *Phys. Rev. D* **58**, 023003 (1998), [arXiv:astro-ph/9803150](#).
- [109] J. Guzik, U. Seljak, and M. Zaldarriaga, “Lensing effect on polarization in the microwave background: Extracting the convergence power spectrum”, *Phys. Rev. D* **62**, 043517 (2000), [arXiv:astro-ph/9912505](#).
- [110] A. Lewis and A. Challinor, “Weak gravitational lensing of the CMB”, *Phys. Rept.* **429**, 1–65 (2006), [arXiv:astro-ph/0601594](#).
- [111] P. A. R. Ade et al. (Planck), “Planck intermediate results. XLI. A map of lensing-induced B-modes”, *Astron. Astrophys.* **596**, A102 (2016), [arXiv:1512.02882 \[astro-ph.CO\]](#).
- [112] B. D. Sherwin and M. Schmittfull, “Delensing the CMB with the Cosmic Infrared Background”, *Phys. Rev. D* **92**, 043005 (2015), [arXiv:1502.05356 \[astro-ph.CO\]](#).
- [113] L. Marian and G. M. Bernstein, “Detectability of CMB tensor B modes via delensing with weak lensing galaxy surveys”, *Phys. Rev. D* **76**, 123009 (2007), [arXiv:0710.2538 \[astro-ph\]](#).
- [114] T. Namikawa, D. Yamauchi, B. Sherwin, and R. Nagata, “Delensing Cosmic Microwave Background B-modes with the Square Kilometre Array Radio Continuum Survey”, *Phys. Rev. D* **93**, 043527 (2016), [arXiv:1511.04653 \[astro-ph.CO\]](#).
- [115] K. M. Gorski, E. Hivon, A. J. Banday, B. D. Wandelt, F. K. Hansen, M. Reinecke, and M. Bartelman, “HEALPix - A Framework for high resolution discretization, and fast analysis of data distributed on the sphere”, *Astrophys. J.* **622**, 759–771 (2005), [arXiv:astro-ph/0409513](#).
- [116] K. M. Gorski, E. Hivon, and B. D. Wandelt, “Analysis issues for large CMB data sets”, in *MPA/ESO Cosmology Conference: Evolution of Large Scale Structure: From Recombination to Garching* (Dec. 1998), [arXiv:astro-ph/9812350](#).
- [117] A. Zonca, L. Singer, D. Lenz, M. Reinecke, C. Rosset, E. Hivon, and K. Gorski, “healpy: equal area pixelization and spherical harmonics transforms for data on the sphere in Python”, *Journal of Open Source Software* **4**, 1298 (2019).
- [118] M. Zaldarriaga, “Nature of the E B decomposition of CMB polarization”, *Phys. Rev. D* **64**, 103001 (2001), [arXiv:astro-ph/0106174](#).
- [119] E. F. Bunn, “Efficient decomposition of cosmic microwave background polarization maps into pure E, pure B, and ambiguous components”, *Phys. Rev. D* **83**, 083003 (2011), [arXiv:1008.0827 \[astro-ph.CO\]](#).

- [120] J. D. McEwen and Y. Wiaux, “A Novel Sampling Theorem on the Sphere”, *IEEE Transactions on Signal Processing* **59**, 5876–5887 (2011), [arXiv:1110.6298 \[cs.IT\]](#).
- [121] A. Abergel et al. (Planck), “Planck 2013 results. XI. All-sky model of thermal dust emission”, *Astron. Astrophys.* **571**, A11 (2014), [arXiv:1312.1300 \[astro-ph.GA\]](#).
- [122] R. Adam et al. (Planck), “Planck 2015 results. X. Diffuse component separation: Foreground maps”, *Astron. Astrophys.* **594**, A10 (2016), [arXiv:1502.01588 \[astro-ph.CO\]](#).
- [123] S. Prunet and A. Lazarian, “Thermal Dust Emission as a Polarized Foreground”, in *Microwave foregrounds*, Vol. 181, edited by A. de Oliveira-Costa and M. Tegmark, *Astronomical Society of the Pacific Conference Series* (Jan. 1999), p. 113.
- [124] M. O. Irfan, J. Bobin, M.-A. Miville-Deschenes, and I. Grenier, “Determining thermal dust emission from Planck HFI data using a sparse, parametric technique”, *Astron. Astrophys.* **623**, A21 (2019), [arXiv:1901.01713 \[astro-ph.CO\]](#).
- [125] M. Vidal, C. Dickinson, R. D. Davies, and J. P. Leahy, “Polarized radio filaments outside the Galactic plane”, *Mon. Not. Roy. Astron. Soc.* **452**, 656–675 (2015), [arXiv:1410.4438 \[astro-ph.GA\]](#).
- [126] P. A. R. Ade et al. (Planck), “Planck 2015 results. XXV. Diffuse low-frequency Galactic foregrounds”, *Astron. Astrophys.* **594**, A25 (2016), [arXiv:1506.06660 \[astro-ph.GA\]](#).
- [127] K. W. Yoon et al., “The Robinson Gravitational Wave Background Telescope (BICEP): A bolometric large angular scale CMB polarimeter”, *Proc. SPIE Int. Soc. Opt. Eng.* **6275**, edited by J. C. Mather, H. A. MacEwen, and M. W. M. de Graauw, 62751K (2006), [arXiv:astro-ph/0606278](#).
- [128] B. Racine et al. (BICEP, Keck), “Measurements of Degree-Scale B-mode Polarization with the BICEP/Keck Experiments at South Pole”, in *53rd Rencontres de Moriond on Cosmology* (July 2018), [arXiv:1807.02199 \[astro-ph.CO\]](#).
- [129] M. Tegmark and A. de Oliveira-Costa, “How to measure CMB polarization power spectra without losing information”, *Phys. Rev. D* **64**, 063001 (2001), [arXiv:astro-ph/0012120](#).
- [130] A. Lewis, A. Challinor, and N. Turok, “Analysis of CMB polarization on an incomplete sky”, *Phys. Rev. D* **65**, 023505 (2002), [arXiv:astro-ph/0106536](#).
- [131] K. M. Gorski, “On Determining the spectrum of primordial inhomogeneity from the Cobe DMR sky maps. 1. Method”, *Astrophys. J. Lett.* **430**, L85 (1994), [arXiv:astro-ph/9403066](#).
- [132] D. J. Mortlock, A. D. Challinor, and M. P. Hobson, “Analysis of cosmic microwave background data on an incomplete sky”, *Mon. Not. Roy. Astron. Soc.* **330**, 405 (2002), [arXiv:astro-ph/0008083](#).

- [133] W. Zhao and D. Baskaran, “Separating E and B types of polarization on an incomplete sky”, *Phys. Rev. D* **82**, 023001 (2010), [arXiv:1005.1201 \[astro-ph.CO\]](#).
- [134] K. M. Smith, “Pseudo- C_ℓ estimators which do not mix E and B modes”, *Phys. Rev. D* **74**, 083002 (2006), [arXiv:astro-ph/0511629](#).
- [135] K. M. Smith and M. Zaldarriaga, “A general solution to the E-B mixing problem”, *Phys. Rev. D* **76**, 043001 (2007), [arXiv:astro-ph/0610059](#).
- [136] K. M. Smith, “Pure pseudo- C_ℓ estimators for CMB B-modes”, *New Astron. Rev.* **50**, 1025–1029 (2006), [arXiv:astro-ph/0608662](#).
- [137] H. Liu, “General solutions of the leakage in integral transforms and applications to the EB-leakage and detection of the cosmological gravitational wave background”, *JCAP* **10**, 001 (2019), [arXiv:1906.10381 \[astro-ph.CO\]](#).
- [138] S. von Hausegger, “In the foreground - Steps towards a clear view on the Cosmic Microwave Background”, PhD thesis (University of Copenhagen, 2019).
- [139] J. Kim and P. Naselsky, “CMB E/B decomposition of incomplete sky: a pixel space approach”, *Astron. Astrophys.* **519**, A104 (2010), [arXiv:1003.2911 \[astro-ph.CO\]](#).
- [140] P. A. R. Ade et al. (Planck), “Planck 2015 results. XII. Full Focal Plane simulations”, *Astron. Astrophys.* **594**, A12 (2016), [arXiv:1509.06348 \[astro-ph.CO\]](#).
- [141] M. Tegmark, “How to measure CMB power spectra without losing information”, *Phys. Rev. D* **55**, 5895–5907 (1997), [arXiv:astro-ph/9611174](#).
- [142] E. Hivon, K. M. Gorski, C. B. Netterfield, B. P. Crill, S. Prunet, and F. Hansen, “Master of the cosmic microwave background anisotropy power spectrum: a fast method for statistical analysis of large and complex cosmic microwave background data sets”, *Astrophys. J.* **567**, 2 (2002), [arXiv:astro-ph/0105302](#).
- [143] G. Polenta, D. Marinucci, A. Balbi, P. de Bernardis, E. Hivon, S. Masi, P. Natoli, and N. Vittorio, “Unbiased estimation of angular power spectrum”, *JCAP* **11**, 001 (2005), [arXiv:astro-ph/0402428](#).
- [144] D. Molinari, A. Gruppuso, G. Polenta, C. Burigana, A. De Rosa, P. Natoli, F. Finelli, and F. Paci, “A comparison of CMB Angular Power Spectrum Estimators at Large Scales: the TT case”, *Mon. Not. Roy. Astron. Soc.* **440**, 957–964 (2014), [arXiv:1403.1089 \[astro-ph.CO\]](#).
- [145] D. Alonso, J. Sanchez, and A. Slosar (LSST Dark Energy Science), “A unified pseudo- C_ℓ framework”, *Mon. Not. Roy. Astron. Soc.* **484**, 4127–4151 (2019), [arXiv:1809.09603 \[astro-ph.CO\]](#).
- [146] J. Grain, M. Tristram, and R. Stompor, “Polarized CMB spectrum estimation using the pure pseudo cross-spectrum approach”, *Phys. Rev. D* **79**, 123515 (2009), [arXiv:0903.2350 \[astro-ph.CO\]](#).

- [147] M. Preece and R. A. Battye, “Testing cosmic microwave background polarization data using position angles”, *Mon. Not. Roy. Astron. Soc.* **444**, 162–171 (2014), [arXiv:1407.6772 \[astro-ph.CO\]](#).
- [148] M. Vidal, J. P. Leahy, and C. Dickinson, “A new polarization amplitude bias reduction method”, *Mon. Not. Roy. Astron. Soc.* **461**, 698–709 (2016), [arXiv:1410.4436 \[astro-ph.IM\]](#).
- [149] K. Mardia, *Statistics of Directional Data*, Probability and Mathematical Statistics: A Series of Monographs and Textbooks (Academic Press, 1972).
- [150] F. Wang and A. E. Gelfand, “Directional data analysis under the general projected normal distribution”, *Statistical Methodology* **10**, 113–127 (2013).
- [151] P. A. R. Ade et al. (Planck), “Planck 2015 results. VI. LFI mapmaking”, *Astron. Astrophys.* **594**, A6 (2016), [arXiv:1502.01585 \[astro-ph.CO\]](#).
- [152] R. Adam et al. (Planck), “Planck 2015 results. VIII. High Frequency Instrument data processing: Calibration and maps”, *Astron. Astrophys.* **594**, A8 (2016), [arXiv:1502.01587 \[astro-ph.CO\]](#).
- [153] Y. Akrami et al. (Planck), “Planck 2018 results. II. Low Frequency Instrument data processing”, *Astron. Astrophys.* **641**, A2 (2020), [arXiv:1807.06206 \[astro-ph.CO\]](#).
- [154] N. Aghanim et al. (Planck), “Planck 2018 results. III. High Frequency Instrument data processing and frequency maps”, *Astron. Astrophys.* **641**, A3 (2020), [arXiv:1807.06207 \[astro-ph.CO\]](#).
- [155] J. M. Bardeen, J. R. Bond, N. Kaiser, and A. S. Szalay, “The Statistics of Peaks of Gaussian Random Fields”, *Astrophys. J.* **304**, 15–61 (1986).
- [156] J. R. Bond and G. Efstathiou, “The statistics of cosmic background radiation fluctuations”, *Mon. Not. Roy. Astron. Soc.* **226**, 655–687 (1987).
- [157] N. Vittorio and R. Juszkiewicz, “Hot Spots in the Microwave Sky”, *apjl* **314**, L29 (1987).
- [158] D. L. Jow, D. Contreras, D. Scott, and E. F. Bunn, “Taller in the saddle: constraining CMB physics using saddle points”, *JCAP* **03**, 031 (2019), [arXiv:1811.05629 \[astro-ph.CO\]](#).
- [159] D. Marinucci, “Testing for Non-Gaussianity on Cosmic Microwave Background Radiation: A Review”, *Statist. Sci.* **19**, 294 (2004).
- [160] K. R. Mecke, T. Buchert, and H. Wagner, “Robust morphological measures for large scale structure in the universe”, *Astron. Astrophys.* **288**, 697–704 (1994), [arXiv:astro-ph/9312028](#).
- [161] S. Winitzki and A. Kosowsky, “Minkowski functional description of microwave background Gaussianity”, *New Astron.* **3**, 75 (1998), [arXiv:astro-ph/9710164](#).

- [162] J. Schmalzing and K. M. Gorski, “Minkowski functionals used in the morphological analysis of cosmic microwave background anisotropy maps”, *Mon. Not. Roy. Astron. Soc.* **297**, 355 (1998), [arXiv:astro-ph/9710185](#).
- [163] D. Novikov, H. A. Feldman, and S. F. Shandarin, “Minkowski functionals and cluster analysis for CMB maps”, *Int. J. Mod. Phys. D* **8**, 291–306 (1999), [arXiv:astro-ph/9809238](#).
- [164] D. Novikov, J. Schmalzing, and V. F. Mukhanov, “On non-Gaussianity in the cosmic microwave background”, *Astron. Astrophys.* **364**, 17–25 (2000), [arXiv:astro-ph/0006097](#).
- [165] H. K. Eriksen, D. I. Novikov, P. B. Lilje, A. J. Banday, and K. M. Gorski, “Testing for non-Gaussianity in the WMAP data: Minkowski functionals and the length of the skeleton”, *Astrophys. J.* **612**, 64–80 (2004), [arXiv:astro-ph/0401276](#).
- [166] P. D. Naselsky and D. I. Novikov, “General statistical properties of the CMB polarization field”, *Astrophys. J.* **507**, 31 (1998), [arXiv:astro-ph/9801285](#).
- [167] P. D. Naselsky and D. I. Novikov, “Percolation and Cluster Analysis for Delta T/T Maps”, *Astrophys. J. Lett.* **444**, L1 (1995).
- [168] A. D. Dolgov, A. G. Doroshkevich, D. I. Novikov, and I. D. Novikov, “Classification of singular points in polarization field of cmb and eigenvectors of stokes matrix”, *JETP Lett.* **69**, 427 (1999), [arXiv:astro-ph/9806104](#).
- [169] A. Lewis, A. Challinor, and A. Lasenby, “Efficient computation of CMB anisotropies in closed FRW models”, *Astrophys. J.* **538**, 473–476 (2000), [arXiv:astro-ph/9911177](#).
- [170] K. Land and J. Magueijo, “Is the Universe odd?”, *Phys. Rev. D* **72**, 101302 (2005), [arXiv:astro-ph/0507289](#).
- [171] J. Kim and P. Naselsky, “Anomalous parity asymmetry of the Wilkinson Microwave Anisotropy Probe power spectrum data at low multipoles”, *Astrophys. J. Lett.* **714**, L265–L267 (2010), [arXiv:1001.4613 \[astro-ph.CO\]](#).
- [172] J. Kim and P. Naselsky, “Anomalous parity asymmetry of WMAP power spectrum data at low multipoles: is it cosmological or systematics?”, *Phys. Rev. D* **82**, 063002 (2010), [arXiv:1002.0148 \[astro-ph.CO\]](#).
- [173] A. Gruppuso, F. Finelli, P. Natoli, F. Paci, P. Cabella, A. De Rosa, and N. Mandolesi, “New constraints on Parity Symmetry from a re-analysis of the WMAP-7 low resolution power spectra”, *Mon. Not. Roy. Astron. Soc.* **411**, 1445–1452 (2011), [arXiv:1006.1979 \[astro-ph.CO\]](#).
- [174] H. K. Eriksen, F. K. Hansen, A. J. Banday, K. M. Gorski, and P. B. Lilje, “Asymmetries in the Cosmic Microwave Background anisotropy field”, *Astrophys. J.* **605**, [Erratum: *Astrophys. J.* 609, 1198 (2004)], 14–20 (2004), [arXiv:astro-ph/0307507](#).

- [175] F. K. Hansen, A. J. Banday, and K. M. Gorski, “Testing the cosmological principle of isotropy: Local power spectrum estimates of the WMAP data”, *Mon. Not. Roy. Astron. Soc.* **354**, 641–665 (2004), [arXiv:astro-ph/0404206](#).
- [176] F. K. Hansen, A. J. Banday, K. M. Gorski, H. K. Eriksen, and P. B. Lilje, “Power Asymmetry in Cosmic Microwave Background Fluctuations from Full Sky to Sub-degree Scales: Is the Universe Isotropic?”, *Astrophys. J.* **704**, 1448–1458 (2009), [arXiv:0812.3795 \[astro-ph\]](#).
- [177] J. Hoftuft, H. K. Eriksen, A. J. Banday, K. M. Gorski, F. K. Hansen, and P. B. Lilje, “Increasing evidence for hemispherical power asymmetry in the five-year WMAP data”, *Astrophys. J.* **699**, 985–989 (2009), [arXiv:0903.1229 \[astro-ph.CO\]](#).
- [178] C. Gordon, W. Hu, D. Huterer, and T. M. Crawford, “Spontaneous isotropy breaking: a mechanism for cmb multipole alignments”, *Phys. Rev. D* **72**, 103002 (2005), [arXiv:astro-ph/0509301](#).
- [179] M. Tegmark, A. de Oliveira-Costa, and A. Hamilton, “A high resolution foreground cleaned CMB map from WMAP”, *Phys. Rev. D* **68**, 123523 (2003), [arXiv:astro-ph/0302496](#).
- [180] A. de Oliveira-Costa, M. Tegmark, M. Zaldarriaga, and A. Hamilton, “The Significance of the largest scale CMB fluctuations in WMAP”, *Phys. Rev. D* **69**, 063516 (2004), [arXiv:astro-ph/0307282](#).
- [181] C. J. Copi, D. Huterer, D. J. Schwarz, and G. D. Starkman, “Large-scale alignments from WMAP and Planck”, *Mon. Not. Roy. Astron. Soc.* **449**, 3458–3470 (2015), [arXiv:1311.4562 \[astro-ph.CO\]](#).
- [182] P. A. R. Ade et al. (Planck), “Planck 2013 results. XXIII. Isotropy and statistics of the CMB”, *Astron. Astrophys.* **571**, A23 (2014), [arXiv:1303.5083 \[astro-ph.CO\]](#).
- [183] C. J. Copi, D. Huterer, D. J. Schwarz, and G. D. Starkman, “No large-angle correlations on the non-Galactic microwave sky”, *Mon. Not. Roy. Astron. Soc.* **399**, 295–303 (2009), [arXiv:0808.3767 \[astro-ph\]](#).
- [184] C. J. Copi, D. Huterer, D. J. Schwarz, and G. D. Starkman, “Lack of large-angle TT correlations persists in WMAP and Planck”, *Mon. Not. Roy. Astron. Soc.* **451**, 2978–2985 (2015), [arXiv:1310.3831 \[astro-ph.CO\]](#).
- [185] M. Cruz, E. Martinez-Gonzalez, P. Vielva, and L. Cayon, “Detection of a non-Gaussian spot in WMAP”, *Mon. Not. Roy. Astron. Soc.* **356**, 29–40 (2005), [arXiv:astro-ph/0405341](#).
- [186] M. Cruz, M. Tucci, E. Martinez-Gonzalez, and P. Vielva, “The non-Gaussian Cold Spot in WMAP: significance, morphology and foreground contribution”, *Mon. Not. Roy. Astron. Soc.* **369**, 57–67 (2006), [arXiv:astro-ph/0601427](#).

- [187] S. Mukherjee, “Hemispherical asymmetry from an isotropy violating stochastic gravitational wave background”, *Phys. Rev. D* **91**, 062002 (2015), [arXiv:1412.2491 \[astro-ph.CO\]](#).
- [188] I. Agullo, D. Kranas, and V. Sreenath, “Large scale anomalies in the CMB and non-Gaussianity in bouncing cosmologies”, *Class. Quant. Grav.* **38**, 065010 (2021), [arXiv:2006.09605 \[astro-ph.CO\]](#).
- [189] M. Hansen, J. Kim, A. M. Frejsel, S. Ramazanov, P. Naselsky, W. Zhao, and C. Burigana, “Can residuals of the Solar system foreground explain low multipole anomalies of the CMB?”, *JCAP* **10**, 059 (2012), [arXiv:1206.6981 \[astro-ph.CO\]](#).
- [190] C. J. Copi, D. Huterer, D. J. Schwarz, and G. D. Starkman, “Large angle anomalies in the CMB”, *Adv. Astron.* **2010**, 847541 (2010), [arXiv:1004.5602 \[astro-ph.CO\]](#).
- [191] D. J. Schwarz, C. J. Copi, D. Huterer, and G. D. Starkman, “CMB Anomalies after Planck”, *Class. Quant. Grav.* **33**, 184001 (2016), [arXiv:1510.07929 \[astro-ph.CO\]](#).
- [192] A. Rassat, J.-L. Starck, P. Paykari, F. Sureau, and J. Bobin, “Planck CMB Anomalies: Astrophysical and Cosmological Secondary Effects and the Curse of Masking”, *JCAP* **08**, 006 (2014), [arXiv:1405.1844 \[astro-ph.CO\]](#).
- [193] A. Rakic and D. J. Schwarz, “Correlating anomalies of the microwave sky: The Good, the Evil and the Axis”, *Phys. Rev. D* **75**, 103002 (2007), [arXiv:astro-ph/0703266](#).
- [194] L. Polastri, A. Gruppuso, and P. Natoli, “CMB low multipole alignments in the Λ CDM and Dipolar models”, *JCAP* **04**, 018 (2015), [arXiv:1503.01611 \[astro-ph.CO\]](#).
- [195] A. Gruppuso, N. Kitazawa, M. Lattanzi, N. Mandolesi, P. Natoli, and A. Sagnotti, “The Evens and Odds of CMB Anomalies”, *Phys. Dark Univ.* **20**, 49–64 (2018), [arXiv:1712.03288 \[astro-ph.CO\]](#).
- [196] J. Muir, S. Adhikari, and D. Huterer, “Covariance of CMB anomalies”, *Phys. Rev. D* **98**, 023521 (2018), [arXiv:1806.02354 \[astro-ph.CO\]](#).
- [197] U. Natale, A. Gruppuso, D. Molinari, and P. Natoli, “Is the lack of power anomaly in the CMB correlated with the orientation of the Galactic plane?”, *JCAP* **12**, 052 (2019), [arXiv:1908.10637 \[astro-ph.CO\]](#).
- [198] S. Shaikh, S. Mukherjee, S. Das, B. D. Wandelt, and T. Souradeep, “Joint Bayesian Analysis of Large Angular Scale CMB Temperature Anomalies”, *JCAP* **08**, 007 (2019), [arXiv:1902.10155 \[astro-ph.CO\]](#).
- [199] A. Marcos-Caballero and E. Martinez-Gonzalez, “Scale-dependent dipolar modulation and the quadrupole-octopole alignment in the CMB temperature”, *JCAP* **10**, 053 (2019), [arXiv:1909.06093 \[astro-ph.CO\]](#).
- [200] S. Mukherjee and T. Souradeep, “Litmus Test for Cosmic Hemispherical Asymmetry in the Cosmic Microwave Background B-mode polarization”, *Phys. Rev. Lett.* **116**, 221301 (2016), [arXiv:1509.06736 \[astro-ph.CO\]](#).

- [201] M. Billi, A. Gruppuso, N. Mandolesi, L. Moscardini, and P. Natoli, “Polarisation as a tracer of CMB anomalies: Planck results and future forecasts”, *Phys. Dark Univ.* **26**, 100327 (2019), [arXiv:1901.04762 \[astro-ph.CO\]](#).
- [202] D. Contreras, J. P. Zibin, D. Scott, A. J. Banday, and K. M. Górski, “Testing physical models for dipolar asymmetry with CMB polarization”, *Phys. Rev. D* **96**, 123522 (2017), [arXiv:1704.03143 \[astro-ph.CO\]](#).
- [203] P. A. R. Ade et al. (Planck), “Planck 2015 results. XVI. Isotropy and statistics of the CMB”, *Astron. Astrophys.* **594**, A16 (2016), [arXiv:1506.07135 \[astro-ph.CO\]](#).
- [204] A. M. Frejsel, “Large Scale Anomalies of the Cosmic Microwave Background with Planck”, PhD thesis (University of Copenhagen, 2015).
- [205] J. Hoftuft, H. K. Eriksen, A. J. Banday, K. M. Gorski, F. K. Hansen, and P. B. Lilje, “Increasing evidence for hemispherical power asymmetry in the five-year WMAP data”, *Astrophys. J.* **699**, 985–989 (2009), [arXiv:0903.1229 \[astro-ph.CO\]](#).
- [206] S. Nadarajah and T. K. Pogany, “On the distribution of the product of correlated normal random variables”, *Comptes Rendus Mathematique* **354**, 201–204 (2016).
- [207] R. E. Gaunt, “A note on the distribution of the product of zero-mean correlated normal random variables”, *Statistica Neerlandica* **73**, 176–179 (2019), eprint: [1807.03981](#).
- [208] C. J. Copi, D. Huterer, and G. D. Starkman, “Multipole vectors - A New representation of the CMB sky and evidence for statistical anisotropy or non-Gaussianity at $2 \leq l \leq 8$ ”, *Phys. Rev. D* **70**, 043515 (2004), [arXiv:astro-ph/0310511](#).
- [209] R. Adam et al. (Planck), “Planck 2015 results. I. Overview of products and scientific results”, *Astron. Astrophys.* **594**, A1 (2016), [arXiv:1502.01582 \[astro-ph.CO\]](#).
- [210] C. Chiocchetta, A. Gruppuso, M. Lattanzi, P. Natoli, and L. Pagano, “Lack-of-correlation anomaly in CMB large scale polarisation maps”, (2020), [arXiv:2012.00024 \[astro-ph.CO\]](#).

ACKNOWLEDGMENTS

This work was funded in part by Villum Fonden through the Deep Space project. Some of the results in this thesis have been derived using the healpy and HEALPix packages [115, 117]. Many of the results are based on observations obtained with *Planck* (<http://www.esa.int/Planck>), an ESA science mission with instruments and contributions directly funded by ESA Member States, NASA, and Canada.